Behavior of Triplex Silicon Carbide Fuel Cladding Designs Tested Under Simulated PWR Conditions

by

John D. Stempien

B.S. Chemistry
University of Vermont, 2008

ARCHIVES
MASSACHUSETTS INSTITUTE OF TECHNOLOGY
JUL 25 2012
LIBRARIES

SUBMITTED TO THE DEPARTMENT OF NUCLEAR SCIENCE AND ENGINEERING IN PARTIAL FULFILLMENT OF THE REQUIREMENTS FOR THE DEGREE OF

MASTER OF SCIENCE IN NUCLEAR SCIENCE AND ENGINEERING
AT THE
MASSACHUSETTS INSTITUTE OF TECHNOLOGY

June 2011

© Massachusetts Institute of Technology, 2011. All rights reserved.

Signature of Author: _____
Department of Nuclear Science and Engineering
May 6, 2011

Certified by: _____
Mujid S. Kazimi, Ph.D.
TEPCO Professor of Nuclear Engineering
Thesis Supervisor

Certified by: _____
Gordon Kohse, Ph.D.
Principal Research Engineer
Thesis Reader

Accepted by: _____
Mujid S. Kazimi, Ph.D.
TEPCO Professor of Nuclear Engineering
Chair, Department Committee on Graduate Students

THIS PAGE LEFT INTENTIONALLY BLANK.

Behavior of Triplex Silicon Carbide Fuel Cladding Designs Tested Under Simulated PWR Conditions

by

John D. Stempien

Submitted to the Department of Nuclear Science and Engineering
on May 6, 2011 in Partial Fulfillment of the
Requirements for the Degree of Master of Science

A silicon carbide (SiC) fuel cladding for LWRs may allow a number of advances, including: increased safety margins under transients and accident scenarios, such as loss of coolant accidents; improved resource utilization via a higher burnup beyond the present limit of 62 GWd/MTU; and improved waste management. The proposed design, referred to as Triplex, consists of three layers: an inner monolith, a central composite, and an outer environmental barrier coating (EBC). The inner monolith consists of dense SiC which provides strength and hermeticity to contain fission products. The composite layer is made of SiC fibers, woven around the monolith, and then infiltrated with a SiC matrix. The composite layer adds strength to the monolith and provides a pseudo-ductile failure mode. The EBC is a thin coating of SiC applied to the outside of the composite to protect it against corrosion. The ends of the tubes may be sealed via the bonding of SiC end caps to the SiC tube. Triplex tube samples, monolith-only samples, and SiC/SiC bonding samples (consisting of two blocks bonded together) were tested in three phases as part of an evaluation of the SiC cladding system. A number of samples were exposed to PWR coolant and neutronic conditions using an in-core loop in the MIT research reactor (MITR-II). Other samples remained in their as-fabricated states for comparison. First, mechanical testing revealed significant strength reduction in the Triplex samples due to irradiation-induced point defects, corrosive pitting of the monolith, and possible differences in the behavior of the Triplex components. Some manufacturing abnormalities were also discovered which could have compromised strength. The Triplex samples tested here were not as strong as reported in a previous study. SEM analysis was able to follow the propagation of cracks from initiation, at the monolith inner surface, to termination, upon breaching the EBC. The composite layer was found to be key in dissipating the energy driving the crack formation. Second, three SiC/SiC bonding methods (six samples total) were tested in the MITR-II to 0.2 dpa, and five of the six samples failed. SEM analysis indicates radiation induced degradation of the bond material. Dimensional and volume measurements established the anisotropic swelling of the two SiC blocks in each bond sample, which would have caused shear stresses on the bonds, contributing to their failure. Finally, thermal diffusivity measurements of the Triplex samples show substantial decreases with irradiation (saturating at about 1 dpa) due to the accumulation of phonon-scattering defects and corrosion of SiC. By 1 dpa, the thermal diffusivity/conductivity of this SiC cladding design is diminished to a value lower than that of Zircaloy. In the as-fabricated state, a large difference exists between the monolith-only and Triplex samples due to the phonon scattering centers at the interfaces of the layers. With irradiation this difference decreases, suggesting that similar corrosion and radiation damage effects exist in both the monolith and Triplex samples.

Thesis Supervisor: Mujid S. Kazimi, Ph.D.
Title: TEPCO Professor of Nuclear Engineering

THIS PAGE LEFT INTENTIONALLY BLANK.

ACKNOWLEDGMENTS

This work was supported by Ceramic Tubular Products, LLC, the Department of Energy through the Idaho National Laboratory-Advanced Test Reactor National Scientific User Facility, and Westinghouse Electric Company. This student was generously supported by the Center for Advanced Energy Systems (CANES) at MIT.

I am grateful to my advisor, Professor Mujid Kazimi, for his help in my choice of a research topic and his sound guidance throughout my research and coursework. As I made the transition from my undergraduate training in chemistry to my new-found home in nuclear engineering, Professor Kazimi's patience and support were invaluable.

Without Dr. David Carpenter, I would have quickly been lost in the sea of sample types, constructions, and irradiation histories. Not to mention the valves, sensors, and readouts of the ACI equipment or the calibration of the hoop test apparatus. Dr. Gordon Kohse, supervised my work and was instrumental in helping to define the scope and content of my work. He was usually available whenever I stopped by, and had numerous suggestions and good advice whenever I hit a snag. Yakov Ostrovsky, at the NRL, was the go-to-guy for experimental supplies and accurate CAD renditions of my hand-drawn designs. I am very grateful to Dr. Mike Short for offering his help whenever SEM micrographs of radioactive samples were required, and to Uuganbayar Otgonbaatar for his assistance and interest in this project.

I would also like to mention my fellow students and friends Bryan Herman, Eric Forrest, and Nick Horelik. All three were sources of humor, support, and sanity. Additionally, I am indebted to Bryan for his indispensable help through several of the core classes that we shared.

Finally, I must express my deepest thanks to my parents and my sisters. We are, indeed, a tight-knit bunch and I pray that we can stay that way forever.

Contents

List of Figures

List of Tables

Nomenclature

A_{plug}	**cross sectional area of polyurethane plug**
c_p	**specific heat at constant pressure**
c_v	**specific heat at contant volume**
F_{adj}	**adjusted maximum force**
F_{max}	**maximum applied force before adjustment**
F_{plug}	**force to compress plug against tube inner diameter**
k	**thermal conductivity**
L	**sample thickness**
m	**mass**
P	**internal pressure at failure**
q''	**heat flux**
r	**radius (variable)**
r_i	**tube inner radius**
r_o	**tube outer radius**
t	**time**
V	**volume**
W	**dimensionless parameter from Parker *et. al.***
α	**thermal diffusivity**
λ	**phonon mean free path**
v	**phonon group velocity**
ω	**dimensionless parameter from Parker *et. al.***
ρ	**material density**
σ_θ	**hoop stress**

Acronyms

ACI	**Advanced Cladding Irradiation**
ATR	**Advanced Test Reactor**
BWR	**boiling water reactor**
CTE	**coefficient of thermal expansion**
CTP	**Ceramic Tubular Products**
CVD	**chemical vapor deposition**
CVI	**chemical vapor infiltration**
DBA	**design basis accident**
DOE	**Department of Energy**
dpa	**displacements per atom**
EBC	**environmental barrier coating**
ECCS	**emergency core cooling system**
EDX	**energy dispersive x-ray spectroscopy**
EFPD	**effective full power days**
EFPY	**effective full power years**
FCCI	**fuel-cladding chemical interaction**
GWd	**giga-watt days**
HNTS	**Hi-Nicalon Type S**
LOCA	**loss of coolant accident**
LOFA	**loss of flow accident**
LTA	**lead test assembly**
LVDT	**linear variable differential transformer**
LWR	**light water reactor**
MCNP	**Monte Carlo N-Particle**
MITR-II	**MIT Research Reactor**
MTU	**mega-tons uranium**
MWt	**mega-watts thermal**
NRC	**Nuclear Regulatory Commission**
NRL	**Nuclear Reactor Lab**
PCMI	**pellet-cladding mechanical interaction**
PIE	**post-irradiation examination**
PIP	**polymer impregnation and pyrolysis**
PNNL	**Pacific Northwest National Laboratory**
PWR	**pressurized water reactor**
RIA	**reactivity insertion accident**
RPV	**reactor pressure vessel**
SEM	**scanning electron microscopy**
TEM	**transmission electron microscopy**
TRISO	**tri-structural isotropic**
UTS	**ultimate tensile strength**

1 Introduction

1.1 Background on Nuclear Fuel Cladding

With respect to materials degradation, the environment within a nuclear reactor is particularly aggressive. High temperature, high pressure, corrosive potentials, and neutron fluences are each, by themselves, demanding on materials. In a reactor environment, structures such as the reactor pressure vessel (RPV) and the fuel cladding are routinely subjected to all four challenges simultaneously. In a light water reactor (LWR), the integrity of the *fuel cladding* is so important that core thermal performance is limited, in large part, by the necessity to protect the fuel cladding from excessive thermal and mechanical stresses. [1] Contemporary LWRs[1] have safely operated within the limitations imposed by the materials; however, development of advanced LWR technologies for present-day reactor designs, and future Generation IV concepts, face rigorous materials development challenges. [2]

1.1.1 Nuclear Fuel Cladding: Definition and Important Properties

Nuclear fuel cladding consists of a hollow tube in which uranium oxide (UO_2) fuel pellets are stacked. (Refer to Figure 2.5 for a representation of a typical LWR fuel pin.) The cladding physically separates the fuel from the coolant and acts as a hermetic seal to prevent the release of fission products into the primary coolant system. A large pressurized water reactor (PWR), has an output of 3400 MWt and houses more than 50,000 fuel rods in its core. [3] In the Sequoyah plant in Tennessee, for example, each of the 50,000 + fuel rods is fabricated to tight tolerances: outer diameter = 9.5 mm, height = 4 m, cladding thickness = 0.57 mm. The cylindrical UO_2 fuel pellets which fill the fuel rods are also manufactured to tight tolerances of 8.2 mm in diameter and 13.5 mm in height. The pellet centerline temperature and the fuel cladding may reach temperatures in excess of 2200 °C and 350 °C respectively. [4, 5, 6] This heat must be transferred to the working fluid (water for LWRs) in order to generate power and cool the fuel rods. Thus, a high thermal conductivity is one important material property for any fuel cladding material.

As a fuel irradiation progresses, the ceramic UO_2 fuel will swell as a result of the build up of internal fission products and radiation damage. Significant thermal stresses and fission gas release cause additional anisotropic deformation of the fuel pellet. At the beginning of a cycle, the fuel cladding itself experiences creep-down *toward* the pellet as a result of the pressure differential between the inside of the pellet, which is initially pressurized with helium gas to 2 MPa, and the coolant, which is pressurized to 15.5 MPa in a PWR. [7] The consequence of fuel swelling and cladding creep-down is contact between the pellet and the cladding, a phenomenon known as pellet cladding mechanical interaction (PCMI).[2] In anticipation of this, the UO_2 pellets are deliberately undersized compared to the diameter of the fuel rod, leaving a gap (initially filled with helium at a pressure of 2 MPa[3]) between the fuel pellet and the fuel rod. Careful design has determined the optimal size of the gap between the fuel and the cladding such that PCMI is minimized and effective heat transfer is maintained. Nevertheless, PCMI remains a serious concern because

[1] Contemporary reactors include Generation II and III designs. Some Generation III+ reactors (such as the AP1000) are now under construction in China.

[2] There is also a differential in the thermal expansion of the pellet and the cladding. For the commonly used zirconium alloy (zircaloy) fuel rod (to be discussed in the next section), the UO_2 pellet experiences greater thermal expansion than the zircaloy does.

[3] The helium fill gas provides better heat transfer across the gap than leaving this space as a vacuum.

its mechanisms are not fully understood, it is a cause of fuel rod failures, and it forces a limitation on the rate of reactor power ramps. [8, 9] For these reasons, any potential cladding material must possess high strength and low proclivity for creep deformation.

In addition to good heat transfer, high strength, and a low creep rate, an effective cladding must also have resistance to radiation damage and corrosive attack. Radiation damage acts to reduce the thermal conductivity and embrittle the cladding as point defects (interstitials, vacancies, etc.), 1D defects (edge dislocations), 2D defects (dislocation loops), and 3D defects (voids etc.) are formed in the microstructure of the material. [10] The cladding should be chemically compatible with the fuel type (UO_2) and the coolant type (water) in order that the intended mechanical and thermal properties of the cladding and fuel be maintained throughout their service lives. [11]

Finally, the ideal cladding material would have a high melting point and a small neutron capture cross section. A high melting point allows the cladding to maintain its structural integrity under all operating conditions as well as postulated accident scenarios. A small capture cross section ensures that the cladding has a minimal impact on the neutron economy of the reactor and low activation at the end of service. [12]

1.1.2 A Brief History of PWR Cladding: From Stainless Steel to Zircaloy-4

Stainless steel fuel cladding was used in the experimental breeder reactor EBR-I, a sodium-potassium cooled fast reactor which began operation in 1951 and was the first nuclear reactor to produce usable electricity. [13] Austenitic stainless steels were used in early reactors due to their good mechanical properties, corrosion resistance, and cost savings compared to Zircaloys. [12] Significant drawbacks to the use of austenitic stainless steel as a cladding material, however, are the large thermal neutron capture cross sections of chromium, cobalt, and traces of other elements such as tantalum.

When EBR-I was reloaded for the second time, its "third core" utilized fuel elements clad in Zircaloy-2.[4] Zircaloy-2 consists of zirconium alloyed with tin, iron, chromium and nickel. It has good corrosion resistance[5], a low neutron capture cross section, and mechanical properties akin to carbon steel. [11] The first large-scale, nuclear power reactor was a PWR built in the United States at Shippingport, Pennsylvania which began operations in 1957 with Zircaloy-2 cladding. Shippingport was built as a collaboration between the U.S. Federal Government and the Duquesne Light Company. In 1961, Yankee-Rowe (a PWR) became the first *fully* commercial nuclear power reactor in the United States and used mostly 348 stainless steel cladding with some test pins made of Zircaloy-2 cladding.[13]

In the late 1960s and early 1970s, the occurrence of cracking in zirconium alloys prompted investigations into the underlying causes. [15] A publication from 1973 was among the first to identify that this cracking was a result of hydrogen embrittlement of the zirconium alloy. [16] It was discovered that Zircaloy-2 is susceptible to hydrogen uptake which forms brittle zirconium hydrides (ZrH_2). This may occur as a result of Zircaloy corrosion in water (see Section 1.3.1). Care must be also taken to minimize the presence of hydrogen in Zircaloy-2 during the manufacturing process, as this may cause hydride precipitation at grain boundaries. [11]

[4] Zircaloy-2 has the following composition: 1.2 - 1.7 % Sn; 0.07 - 0.20% Fe; 0.05 -0.15 % Cr; 0.03 - 0.08 % Ni; 0.08 - 0.15 % O; 0.0015 - 0.003 % C; balance Zr.[14]

[5] Although, at temperatures < 1500 K, Zircaloy may have a higher oxidation rate than stainless steel.

In boiling water reactors (BWR), which have an oxidizing environment, hydrogen embrittlement is less of a concern and Zircaloy-2 continues to be used as fuel cladding to this day. However, in PWRs where the water chemistry has a reducing potential, hydriding is a definite concern. Thus, Zircaloy-4[6] was developed to have a greater resistance to hydrogen embrittlement than Zircaloy-2. [12] Presently, Zircaloy-4 is the cladding of choice for PWRs in the United States.[7] Zircaloys as a whole have been developed to the point where failure of a Zircaloy fuel cladding has become increasingly rare. [17]

1.2 A Perspective on Nuclear Materials Development

A report issued by the U.S. Department of Energy (DOE) and the Generation IV International Forum highlights several target areas for improvement in reactor design: sustainability, economics, safety and reliability, and proliferation resistance. [18] The sustainability goals are described mainly by improved waste management and increased resource utilization. To improve waste management, the volume of nuclear wastes produced as a result of nuclear power reactor operations must be reduced and these wastes must exist in forms which have fewer long lived radioactive isotopes and lower overall levels of radioactivity. Increasing resource utilization means extracting more energy per mass of nuclear fuel. One way to increase resource utilization is to reprocess spent fuel in order to extract the remaining fissile material.

Another method for increasing resource utilization, in the absence of reprocessing or breeding programs, is to operate the nuclear fuel to higher burnup, thus extracting more energy per mass of initial fuel in the core. In the U.S., as of 2002, the average discharge burnup among PWRs was 45.7 GWd/MTU while utilizing fuels with ^{235}U enrichments of less than 4 wt %. [19] In an effort to improve fuel cycle economics and resource utilization, the current trend is towards higher discharge burnups using fuel enriched to 5 wt % ^{235}U. [20] Currently, the U.S. Nuclear Regulatory Commission (NRC) has limited allowable burnup to 62 GWd/MTU for select fuel types, and presently operating PWRs operate at this limit.[8] [21] In addition to operating at the burnup limit, existing LWRs have received permissions for power uprates and more aggressive operation, and this, too, has placed higher demands on the materials. [22] In order to increase the discharge burnup, the average fuel rod power must be increased; or, if the rod power is to remain the same, the fuel residence time must be increased. In practice, some combination of both increased rod power and increased residence time is desirable. In any case, these approaches subject the fuel cladding to greater neutron fluences which lead to increased radiation damage in the material. In addition to increased radiation damage, increased rod power means that the fuel and cladding will operate at higher temperatures and fission gas production (and the stresses associated with it) will be increased. Longer fuel residence times will require the fuel cladding to withstand environmental degradation (such as corrosion, radiation damage, and thermal fatigue) for longer periods of time. [23]

The Generation IV *economics considerations* aim to have competitive life cycle costs, competitive energy production costs, and competitive levels of financial risk associated with the construction and operation of the nuclear plant.

[6] Composition for Zircaloy-4 (wt %): 1.2 - 1.7 % Sn; 0.18 - 0.24 % Fe; 0.07 - 0.13 % Cr; 0.007 % (maximum) Ni; 0.08 - 0.15 % O; 0.0015 - 0.003 % C. [14]

[7] Although, new zirconium alloys such as Zirlo (Westinghouse) and M5 (Areva-ANP) are proving to have improved corrosion resistance.

[8] This limit applies to the core-wide *peak* power assembly. The core average discharge burnup will be lower.

Several approaches for improving the economics of energy production include increasing plant efficiency, increasing core power densities, and utilizing innovative materials, construction, and fabrication techniques. [18]

The Gen IV *safety and reliability goals* are centered on achieving low core damage frequencies and eliminating the need for off-site emergency response. [18] This may be accomplished by increasing the safety margins built into materials and structures, utilizing more passive (inherent) safety mechanisms, and improving human factors that affect nuclear power plant operations.

1.3 Limitations of Zircaloy

As was stated in the opening paragraph of this chapter, fuel performance, reactor operations, and reactor thermal performance are limited by the need to protect the fuel cladding from degradation. If the nuclear power plant were considered to be a chain, the fuel cladding would be its weakest link. It is not the weakest link because the Zircaloy cladding is a poor material, but because the operating environment that the cladding must withstand is arguably the most aggressive in the entire reactor system. If significant advances in the reactor system are desired, the fuel cladding is a prime target for improvement. The primary areas for improvement in reactor design mentioned in the Generation IV report serve as a good guide for the discussion of Zircaloy's apparent limitations. Utilities, industry, and governments are all engaged in efforts to improve the sustainability, economics, and safety/reliability of *existing* LWRs. A discussion of these goals is as relevant to existing LWR technologies as it is to Generation IV concepts.

1.3.1 Challenges to improving the fuel cycle economics and resource utilization with Zircaloy cladding

Improving fuel cycle economics and resource utilization (sustainability) generally means that the fuel must operate to higher burnup. This means increasing the fuel residence time while maintaining the same reactor power rating, or increasing the power rating while maintaining the same cycle length, or some combination of an increased cycle length and an increased power rating. In the case of a higher power rating, the fuel and cladding will operate at higher temperatures, the coolant must flow at higher velocities, and the cladding will experience higher neutron fluences. A longer cycle length exposes the cladding to a corrosive environment for increased durations. Over this duration the primary water chemistry may change in order to protect components of the primary system and/or to control reactivity as the fuel cycle proceeds. Crud may also form and introduce sites ripe for stress corrosion cracking. [24]

Zircaloy is known to form a dark-colored protective oxide layer (ZrO_2) which adheres strongly to the remaining un-oxidized Zircaloy substrate. [12] This oxidation reaction is shown below:

$$Zr + 2H_2O \rightarrow ZrO_2 + 2H_2.$$

As the cladding is exposed to high temperature water for longer periods of time, this dark, adherent film is replaced by a white, less adherent and less protecting film which results in a sharp increase in the corrosion rate. [12] This phenomenon is termed "breakaway", and there is evidence to suggest that breakaway corrosion in Zircaloy-4 may begin at burnups in the vicinity of 35 GWd/MTU. [25] Zirconium oxide (ZrO_2) occupies a volume 1.5 times that of

pure Zr, and thus, reduces the mechanical strength of the Zircaloy as the oxide thickness increases. [11] Zirconium oxide also degrades heat conduction in the Zircaloy cladding. Experimental results from Motta *et. al.* have shown that the oxide thickness may be roughly 40 μm at 35 GWd/MTU burnup, but by the time burnup has reached 45-50 GWd/MTU, the oxide thickness has increased to between 80 and 120 μm. [25] The NRC and industry have accepted a 100 μm limit on oxide thickness, with the option, under the lead test assembly (LTA) program, to allow eight fuel assemblies from a given cycle to operate at corrosion levels predicted to be higher than 100 μm. [21] Primary water corrosion of Zircaloy cladding presents a challenge at increased burnups.

Another issue at increased burnup is the formation of hydrides on the outer surface of the Zircaloy cladding. The oxidation reaction depicted above produces zirconium oxide and hydrogen gas. This reaction occurs at the surface of the fuel rod, and if there are any perforations in the rod, it may occur on the inside of the fuel cladding as well. The net effect is that hydrogen migrates along the temperature gradient, forms brittle zirconium hydride "rims" on the surface of the cladding, and embrittles the cladding. [26] The embrittlement increases as the thickness of the hydride layer increases. Hydriding in Zircaloy becomes more and more of a concern as burnup increases. Besides embrittlement due to oxide and hydride formation, Zircaloy cladding also experiences embrittlement as a result of radiation damage which becomes more severe at higher burnups (higher fluences). [14]

1.3.2 Challenges to improving safety and reliability using Zircaloy cladding

Design basis accidents (DBA) are postulated accidents that a nuclear power plant is designed to withstand without losing the necessary systems, structures, and components required to protect public health and safety. Some of the most commonly cited DBAs are loss of coolant accidents (LOCA), loss of of flow accidents (LOFA), reactivity initiated accidents (RIA), reactor trips, and turbine trips. [6, 27] Events such as the LOCA, LOFA, and RIA events are not expected to occur at any point during the life of a reactor; nevertheless, reactors are designed with independent, diverse, and redundant systems to protect the reactor in the unlikely event that such an accident occurs. It is under severe accident scenarios where materials, the fuel and cladding in particular, are at greatest risk.

As an example of perhaps the most severe type of accident, consider the double-ended guillotine break of the largest coolant inlet pipe to the reactor core. The reactor will undergo several phases during this accident. Each phase is characterized by different temperatures, pressures, and coolant flow rates. Following the course of events for a postulated large break LOCA illustrates the various points at which the Zircaloy cladding is at greatest risk for severe damage.

The first phase is the "blowdown phase" (which lasts for about 20 seconds) where the contents of the reactor and the inlet leg are blown down through the break in the pipe. The pressure initially falls sharply, a two-phase mixture forms, and portions of the emergency core cooling system (ECCS) are activated in order to attempt to replace coolant inventory lost from the reactor. During this first phase, the temperature of the cladding will jump because the surface of the cladding will experience dryout during the initial part of the blow down phase. Then, the cladding temperature will decrease as blow down continues which has a cooling effect by removing heat via steam from the reactor. [6] In the second phase, called the "bypass phase" (which lasts for ~ 10 seconds) a significant upflow of steam in the

reactor prevents the inflow of water from the ECCS. Once the bypass phase has come to an end, however, the cladding temperature will begin a steady rise. [6] The third phase is called the "refill phase" where the pressure and upward steam flow have decreased to a point where the lower plenum of the reactor core may be refilled by water from the ECCS. It may take 15 - 20 seconds to refill the lower plenum once the refill phase has started. [6] After the refill phase, the "reflood phase" begins and the fuel elements will be re-wetted by water from the ECCS as the core continues to fill. In this large break LOCA scenario, the fuel cladding temperature will rise to 1000 + °C during the reflood phase. [28, 6] The final phase is the "long-term cooling" phase where water is circulated through the core utilizing the ECCS systems (including the containment sump pump) and fuel temperature will begin to slowly decrease from its peak temperatures.

Collier and Hewitt (Reference [6]) present a summary of challenges to cladding integrity as a function of temperature. Between 800 °C and 1500 °C, the internal pressure of the fuel cladding will increase dramatically due to fission gases and the helium fill gases which are present. The fact that the core has depressurized means that the net internal pressure on the fuel cladding may cause the Zircaloy cladding to balloon outward and rupture or perforate. Chemical reactions between Zircaloy and stainless steel are also possible in this temperature range. Between 1450 °C and 1500 °C a highly exothermic oxidation reaction between Zircaloy and steam occurs. [6, 29] This reaction not only heats the Zircaloy further, but also embrittles it due to the uptake of hydrogen gas into the cladding. A fuel-cladding chemical interaction (FCCI) between Zircaloy and UO_2 is also possible between 1600 °C and 1800 °C. [30] In cases where strong PCMI exits, another source reports that cladding melting may initiate at temperatures as low as 1300 °C due to the incipience of FCCI between UO_2 and Zircaloy. [31] (As a side note, strong PCMI may have a number of causes, one of which is another design basis accident, the RIA. A reactivity initiated accident may cause an abrupt thermal expansion of the fuel pellet. When the fuel pellet comes in contact with the cladding, the cladding temperature may increase from 350 °C to 600 °C. [32] Zircaloy's response to transients such as reactor power ramps or swings in reactivity is degraded as radiation damage accumulates in the cladding.) By 1900 °C, the Zircaloy has completely melted. This discussion should illustrate the point that Zircaloy is highly vulnerable under LOCAs due, in large part, to the fact that temperatures and chemical reactions during a LOCA may exceed Zircaloy's abilities to withstand them.

In 10 CFR § 50.46, the NRC has established acceptance criteria for the design of ECCS systems in LWRs. The following criteria must be met for postulated LOCAs: 1.) the peak cladding temperature must not exceed 2200 °F (1200 °C); 2.) the maximum cladding oxidation must not exceed 17 % of the total cladding thickness; 3.) the hydrogen generated from a Zircaloy-steam reaction must not exceed 1 % of the theoretical hydrogen production if all cladding in the core were to react; 4.) any change in the core geometry must be calculated to result in a geometry which is still "coolable"; 5.) long-term cooling must be sufficient to control decay heat and cool the core to acceptable levels. [33] Zircaloy cladding types are being pushed to their limits and if increased safety margins are desired, one approach would be to develop an advanced cladding with improved properties over Zircaloy.

1.4 Silicon Carbide as a potential solution to Zircaloy's limitations.

Silicon Carbide (SiC) exhibits a number of desirable properties which support its candidacy for use as a fuel cladding in LWRs. This work will present data and evaluations of SiC samples tested under PWR conditions which are intended to support the development of SiC-based LWR fuel claddings.

1.4.1 SiC and Improved Safety/Reliability and Economics

Compared to Zircaloy, SiC is less chemically active which results in improved corrosion resistance and reduced susceptibility to hydrogen embrittlement. [23] Reduced chemical activity will help to allow longer cycle lengths and provides resistance to deleterious chemical reactions under accident conditions (i.e. LOCA, RIA, etc.). Another positive attribute is SiC's ability to maintain strength at high temperatures (1600+ °C), allowing for higher power densities (reduced capital costs), and better performance under thermal variations that may occur as a result of transients. [34, 35] Highly pure SiC has a published melting point of 2545 °C compared to Zircaloy's melting point of 1900 °C. SiC has a high thermal conductivity (which exceeds that of nearly all other ceramics and some metals), a low thermal expansion coefficient, and a lower creep rate than Zircaloy. A high thermal conductivity and a low thermal expansion coefficient make SiC less susceptible to thermal shock as a result of LOCA or RIA accidents. These qualities all help to improve the economics and safety margins of a nuclear power plant.

1.4.2 SiC and Improved Sustainability: Resource Utilization and Waste Management

While Zircaloy may represent a neutronic improvement over stainless steel, SiC is a neutronic improvement over Zircaloy. Silicon carbide has a lower thermal neutron absorption cross section ($\sigma_{n,\gamma}$) which aids the neutron economy in the reactor and allows SiC to withstand higher neutron fluences since radiation damage from neturon absorption will accumulate more slowly. Improved neutronic properties and resistance to radiation damage will improve fuel utilization by allowing longer cycle lengths and higher burnups beyond the present limit of 62 GWd/MTU. Additionally, SiC is inherently a low activation material which will make it easier to dispose of when its core residence time has come to an end. [36] These properties of SiC would allow improvements in the areas of sustainability and waste management.

1.5 Objectives and Scope

The majority of the work conducted involved the post-irradiation examination (PIE) of prototype three-layered (Triplex) tubular SiC cladding designs and several methods for bonding distinct SiC pieces together. Samples of different constructions were placed in the Advanced Cladding Irradiation (ACI) test loop inside the MIT research reactor (MITR-II) and irradiated under PWR coolant conditions. At various intervals, samples were removed from the test loop and inspected for dimensional changes, corrosion, degradation of mechanical properties, and degradation of thermal properties.

Various sample preparation and analysis methods were developed in order to collect these data. A new xenon-flash instrument was used to measure the thermal diffusivity of irradiated and un-irradiated samples. This allowed

the relative quantification of the extent of radiation effects. The thermal diffusivity of single-layered SiC tubes was compared to Triplex SiC tubes as well. An in-house burst test was used to determine the hoop strength of irradiated and un-irradiated Triplex designs. Dimensional, mass, and volume measurements were used to help understand the fate of SiC/SiC bond specimens. Scanning electron microscopy (SEM) and energy dispersive X-ray spectroscopy (EDX) were used to help characterize sample surfaces and observe damage phenomena from the burst tests and bond specimens.

2 Introduction to SiC: Crystal Structure, Manufacture, Test Materials, and Test Conditions

Silicon carbide is a ceramic, which, generally speaking, is a term used to describe a non-metallic, inorganic material with a high melting point. More specifically, SiC is a member of a subcategory of ceramics called "structural ceramics" which are characterized by their high strength, high hardness, and strong wear resistance. [37]

2.1 SiC Crystal Structure

Silicon carbide's various properties can be attributed to its crystal structure. Silicon carbide is known to form more than 200 different polytypes (crystal structures) which arise as a result of different periodic stacking of six molecular "bilayers".[9] (Figure 2.1) Each bilayer consists of two close packed planes of Si and C. Unit cells having even numbers of bilayers have hexagonal symmetry, and unit cells with odd numbers of bilayers are cubic (or rhombohedral). Rhombohedral and hexagonal SiC polytypes are termed α-phase SiC (α-SiC) and cubic SiC is called β-SiC. A shorthand known as the Ramsdell notation is used to describe the various SiC polytypes. In the Ramsdell notation, a number denoting the number of bilayers in the unit cell comes first, followed by a C, H, or R which denotes the crystal symmetry (cubic, hexagonal, or rhombohedral). For example, in Figure 2.1, "3C" represents a unit cell of three bilayers with cubic symmetry. The "6H" crystal of SiC has six bilayers with hexagonal symmetry. The most common polytypes of SiC are 3C (β-SiC), 4H, 6H, and 15R (with the latter three all considered α-SiC). [38] It is said that the stacking order of the different polytypes does not result in significant differences in physical properties. [37]

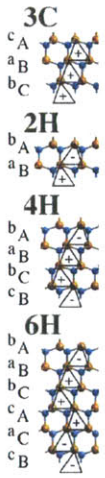

Figure 2.1: Four common polytypes of SiC, each comprised of stacks of different bilayers of Si and C atoms. Adapted from [39].

When the bilayers stack together, they form tetrahedra of Si_4C or SiC_4 as shown in Figure 2.2. The bonds between the Si and C atoms have a primarily covalent nature, with slight ionic bonding characteristics due to silicon having a higher electronegativity than carbon. The dominant covalent nature dictates that the most stable SiC structures are

[9] The six fundamental bilayers are denoted as bA, cA, aB, cB, aC, and bC.

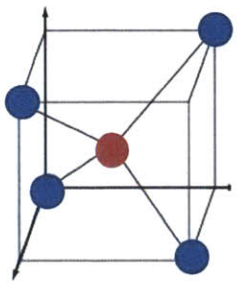

Figure 2.2: Tetrahedral arrangement of Si and C atoms. In the SiC crystal structure, the central (red) atom may be a C while the outer (blue) atoms may be Si atoms, or vice versa.

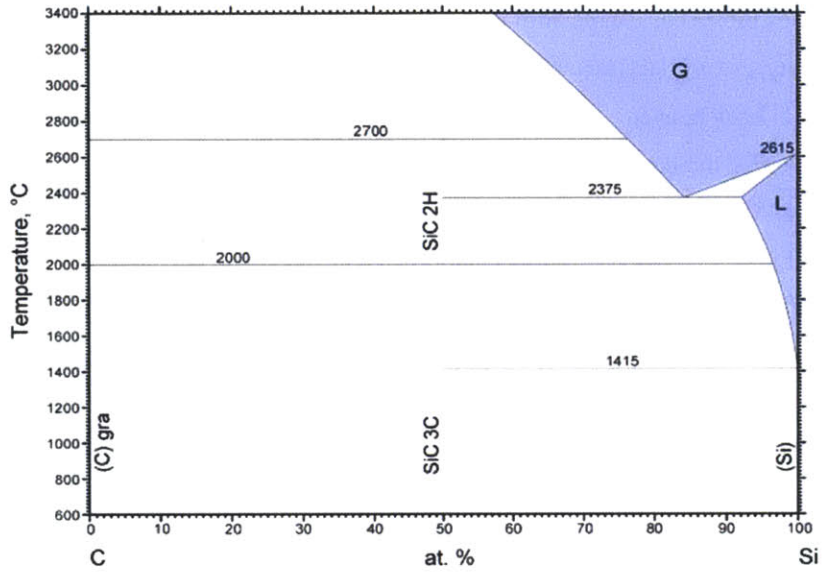

Figure 2.3: Binary phase diagram for SiC. β-SiC is more stable at lower temperatures, but undergoes a phase change to α-SiC at higher temperatures (~2000 °C). [40] The shading represents a single-phase field while the white background represents as two-phase field.

comprised of Si and C in stoichiometric (1:1) amounts. For stoichiometric SiC, phase stability is a strong function of temperature with (3C) β-SiC reported to be more stable at lower temperatures, while α-SiC dominates the high temperature regime as depicted in Figure 2.3.

2.1.1 Mechanical Properties of SiC

Silicon carbide, due to its crystallinity, is susceptible to brittle fracture. However, as will be discussed later in this thesis, novel manufacturing techniques can eliminate (or at least mitigate) the extent of brittle fracture in SiC materials. Brittle fracture is a process by which cracks form and propagate through a cross section of the material in a direction perpendicular to the direction of the imposed load. At room temperature, most ceramics will experience fracture prior to any plastic deformation. For plastic deformation to occur in ceramics, dislocations in the crystal structure must be able to diffuse in response to the applied stress. Ceramics such as SiC are hard and brittle because the motion of the dislocations (slip) is very difficult owing to few slip systems along which the dislocations may travel. [41]

Generally, measured fracture strengths of ceramic materials are lower than those predicted from a consideration of the bond strengths. This is due to the unavoidable presence of flaws in the crystal structure of a ceramic. Flaws act to concentrate and amplify applied stresses which leads to the formation of cracks. Flaws may exist in the material as a result of the manufacturing and processing of the ceramic, or as a result of neutron damage, or as a result of applied mechanical stresses. It is impossible to eliminate all flaws in a crystalline material.

2.1.2 Thermal Conductivity in SiC

Thermal conduction is the transfer of heat from a region of high temperature to a region of lower temperature within a particular substance. The *thermal conductivity* of a material is a quantity which describes the ability of that material to transfer heat. Equation 1 represents Fourier's heat conduction equation for steady-state conditions.

$$q'' = -k\nabla T \tag{1}$$

Here, q" represents the heat flux (heat flow per unit area per unit time), k is the thermal conductivity, and ∇T is the temperature gradient through at 3-dimensional conducting medium. Typical units for the three parameters are as follows: q" = [W/m^2], k = [$\frac{W}{mK}$], and ∇T = [K/m]. The thermal conductivity is related to the *thermal diffusivity* via the following relation:

$$\alpha = \frac{k}{\rho\, c_p} \tag{2}$$

where α is the thermal diffusivity (having units of [m^2/s]), k is the thermal conductivity, ρ is the bulk density, and c_p is the specific heat of the material at constant pressure (with units of [$\frac{J}{kgK}$]). Thermal diffusivity is most often measured using a thermal flash technique to be described later in this thesis. The specific heat may be measured using a differential scanning calorimeter, and the density of the specimen is most often measured using either a liquid density gradient column technique or Archimedes' method.

There are two main modes by which heat may be transported in solid materials: the movement of free electrons and/or the travel of vibrational lattice waves (also known as phonons). [41] Atoms in the crystal lattice vibrate due to thermal energy. If an atom gains or loses thermal energy, its vibrational frequency will increase or decrease (respectively) and this change will be transmitted to other, nearest neighbor atoms through the atomic bonds. This results in traveling lattice waves and the transport of phonons. As a semi-conductor, SiC has a low density of valence band electrons which means that phonons are the primary mode of thermal energy transport in SiC. Defects in the crystal structure play a large role in the scattering of phonons and, thus, the ease of heat conduction in SiC. Phonons may be scattered by irradiation-induced point defects (vacancies and interstitials), defect clusters (voids and dislocation loops), grain boundaries, and phonon-phonon interactions (known as umklapp scattering). [42] Each type of phonon scattering tends to operate over different energy ranges and may be considered separable such that the overall thermal resistance of a material is the sum of the thermal resistances due to each type of phonon scattering. (Equation 3) Here,

k is the total thermal conductivity, and the reciprocal of the thermal conductivity is the thermal resistivity.

$$\frac{1}{k} = \frac{1}{k_{grain\,boundary}} + \frac{1}{k_{umklapp}} + \frac{1}{k_{defect}} \tag{3}$$

Low temperature irradiation of SiC (200 - 800 °C) tends to produce point defects which very effectively scatter phonons and reduce the thermal conductivity/diffusivity. By the time a ceramic has been irradiated to a damage state of a few displacements per atom (dpa), the effect of phonon-defect scattering dominates over other types of phonon scattering, and the reduction of thermal conductivity reaches a saturated state. Moreover, when phonon-defect scattering exceeds phonon-phonon scattering, the temperature dependence of the ceramic's thermal conductivity is greatly weakened. [42] See Section 3.3.2 for a description of dpa estimates for SiC under neutron irradiation.

An alternative expression for the thermal conductivity in SiC which is seen frequently in the literature draws on an analogy to the kinetic theory of gases. For an isotropic solid, the thermal conductivity may be given by the following:

$$k = \frac{1}{3} v c_v \lambda \tag{4}$$

where k is the thermal conductivity, v is the phonon group velocity, c_v is the specific heat at constant volume, and λ is the phonon mean free path. [43] The phonon mean free path is limited by impurities, grain boundaries, irradiation-induced defects, and phonon-phonon scattering. [44]

2.2 Some Applications of SiC

Owing to SiC's hardness, wear resistance, high melting point, electrical conductivity, low neutron cross section, and other desirable properties, SiC has found many uses. For years, SiC has been used as an abrasive, a refractory, and as a resistive heating element in electric furnaces. SiC also features in automotive water pump seals, ballistic armor, roller bearings, and heat exchangers. SiC has been being used as the primary fission product barrier in TRISO (tri-structural isotropic) fuels for gas-cooled nuclear reactors and as diagnostic temperature monitors for radiation environments. SiC is also being considered as a first-wall material for nuclear fusion reactors and as fuel cladding for LWRs.

2.3 Introduction to SiC Samples

The experiments and findings herein are based primarily on two SiC test materials: 1.) a tubular SiC LWR-type cladding and 2.) bonding materials for bonding two distinct SiC pieces together such that the bond can survive PWR operating conditions with adequate margin. The two material types are described in Sections 2.3.1 and 2.3.2, and manufacturing methods relevant to SiC are described in Section 2.3.3.

2.3.1 Triplex Silicon Carbide Cladding Design

Since 1999, Gamma Engineering has been developing and testing SiC cladding for commercial LWRs. In 2005, Gamma Engineering and Innovative Technologies International (NovaTech) formed a joint venture called Ceramic

Tubular Products, LLC (CTP). CTP and its partners have expressed a number of goals for the SiC cladding designs including: allowing an increase in burnup to at least 80 GWD/MTU, reducing operating fuel failures, and improving safety margins for DBAs such as LOCAs and RIAs.

Previous CTP Design Previous work at MIT involved duplex SiC cladding designs. [45, 23] The duplex designs consisted of a dense, inner monolith of SiC and an outer, composite layer made of woven SiC fibers. The monolith is manufactured via a process called chemical vapor deposition (CVD). The SiC fibers are woven around the monolith, and then a SiC matrix fills the voids in the woven composite via a process of either chemical vapor infiltration (CVI) or polymer impregnation and pyrolysis (PIP). The monolithic SiC serves to provide hermeticity in order to contain fission gases, and the outer SiC_f/SiC composite layer helps reinforce the monolith and provide a "graceful" failure mode should the tube rupture during an accident. See Section 2.3.3 for a more detailed description of relevant manufacturing methods.

Current CTP Design The investigation of Triplex SiC cladding designs began more recently and continues at the time of this writing. As the name implies, the Triplex cladding designs, illustrated in Figure 2.4 have three parts: 1.) a dense inner monolith, 2.) a composite layer of SiC fibers woven in a SiC matrix, and 3.) a thin outer layer of SiC called an environmental barrier coating (EBC). As mentioned in the previous paragraph, the monolith is manufactured via a process of CVD. For the composite layer, the SiC fibers are woven around the central monolith, and a CVI process is used to fill the void space within and around the fibers with additional SiC. The monolithic SiC serves to provide hermeticity in order to contain fission gases, and the outer SiC_f/SiC composite layer helps reinforce the monolith and provide a pseudo-ductile failure mode should the tube rupture during an accident. The EBC is a thin (50-150 μm) SiC coating applied to the outside of the composite layer in order to protect the composite layer of the cladding from corrosion. Previous experiments have shown that, when loaded internally, the composite and EBC layers may share between 21.6 % and 37 % of the total hoop load. [46] The monolith, thus, is the primary load bearing structure in the Triplex design.

The dimensions, and uniformity of dimensions, vary from sample to sample. The samples were made in very small volumes on a lab scale. In most cases, the monolith and composite layers are each about 50 % of the total tube wall thickness of the Triplex samples. Table 3.1 summarizes the dimensions and construction of five representative Triplex samples.

In this work, samples consisting of only a monolith layer will be referred to as "monolith-only" samples. Samples consisting of the three layers described above, and depicted in Figure 2.4, will be called "Triplex" samples. The layer consisting of SiC fibers in a SiC matrix, will be referred to as the "composite" layer. This is consistent with the terminology used in [45], [46], and [47].

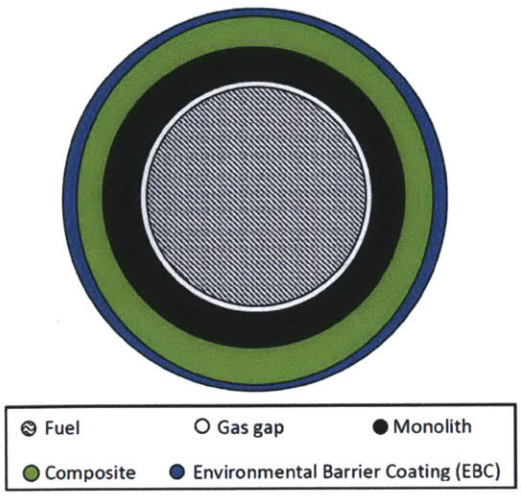

(a) Illustration of the Triplex cladding design. (Not drawn to scale.)

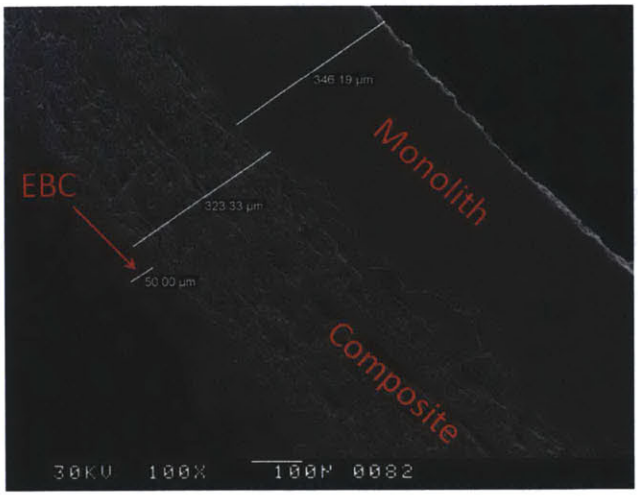

(b) SEM micrograph showing the three layers of the Triplex tube.

Figure 2.4: Illustration and SEM micrograph of the Triplex cladding design.

2.3.2 Bonded-Block Specimens: SiC/SiC Bonding Study

As illustrated in Figure 2.5, after fuel pellets have been loaded into a fuel rod, the top of the rod must be sealed tightly with an end cap in order to retain the helium fill gas and any fission gases produced. On top of the last UO_2 pellet is an insulating pellet (often made of alumina), and pressing down on top of the insulating pellet is a spring located between the end cap and the insulating pellet. The spring is used to keep the fuel pellets firmly located at the bottom of the fuel rod. The space occupied by the spring is a plenum which allows for the accumulation of gases. The material used to plug the top of the fuel rod must be able to withstand the same environment as the rest of the rod. Additionally, the end cap should have the same (or similar) thermal expansion coefficient, swelling behavior, thermal conductivity, hardness, etc. as the material used for the cladding itself.

For fuel pins clad in Zircaloy, the Zircaloy end cap is welded into place. However, for the proposed ceramic SiC cladding, a different means for sealing the end cap to the top of the cladding will be needed. In order to test several methods for bonding a SiC end cap to the top of a SiC fuel rod, several blocks bonded together via different methods were irradiated in the ACI test loop in the MITR-II under the same conditions used to test the Triplex specimens.

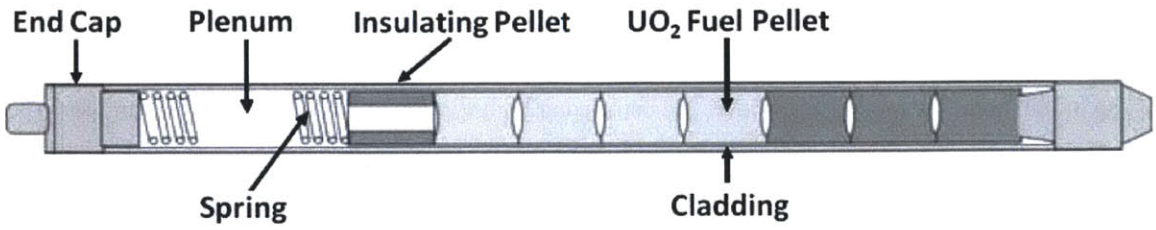

Figure 2.5: Representation of typical LWR fuel pin. Adapted from [7].

Figure 2.6 shows the general construction of the "bonded block" specimens[10], and Table 2.1 shows a range of values for the dimensions labeled in Figure 2.6. Dimensions specific to each bond specimen before and after irradiation can be found in Tables 4.4 and 4.5 respectively. The figure on the left in Figure 2.6 shows that two blocks of equal size and construction are bonded together on their broadest faces such that a certain length of each block is left "free" or un-bonded. The figure on the right of Figure 2.6 depicts an edge view of the blocks.

Each block is an α-phase SiC product called Hexoloy SA® manufactured by Saint-Gobain. Hexoloy SA® is formed by pressureless sintering of a submicron-size SiC powder which results in a self-bonded, fine grain SiC block with a manufacturer specified density of approximately 3.10 g/cm^3 compared to a theoretical density of 3.21 g/cm^{3}for α-SiC. A natural boron (B_4C) sintering aid in 0.6 w/o quantities is used in the manufacturing process.

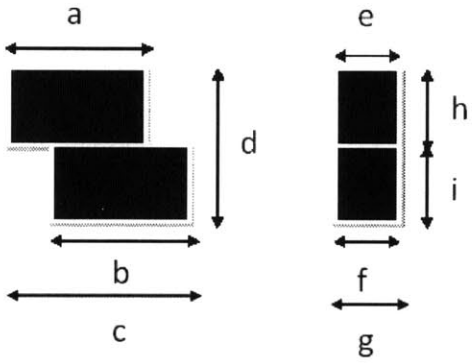

Figure 2.6: Diagram showing the construction of bonded block specimens.

Six bond specimens were irradiated in total, and three bonding methods were used to fabricate these six specimens. Thus, method 1 was used for two of the samples, method 2 was used for two samples, and method 3 was used for two samples. One bonding method used a TiC/SiC tape with an organic binder. A second method used a type of glass-ceramic called calcium aluminate (CaO-Al_2O_3). The third method bonded the two halves together by placing a 10 μm Ti foil between the two halves, heating the two halves, and then pressing them together under 30 MPa of pressure. To fabricate each specimen, two larger blocks of Hexoloy SA were bonded together. These blocks, now bonded, were cut length-wise to give two "identical" specimens bonded with the same method under the same conditions.

2.3.3 Relevant Manufacturing Techniques

In nature, silicon carbide exists as the rare mineral known as moissanite. A methodology for producing synthetic SiC was patented by Edward Acheson in 1893. In order to produce bulk SiC for use as an abrasive, Acheson formed the company Carborundum, which continues to produce SiC to this day. The Acheson process [48] combines carbon from coal derivatives (coke) with silica (SiO_2) or aluminosilicates (Al_2O_3-SiO_2) and heats the combination in a resistance furnace resulting in SiC via the general reaction in Equation 5.

$$SiO_2 + 3C \rightarrow SiC + 2CO \tag{5}$$

[10] A bonded block specimen consists of the two halves that make up the bonded pair. If reference is being made to a half of the bond specimen, it will be stated explicitly.

Table 2.1: Range of values for various dimensions of the bonded block specimens.

	Length (mm)
a	22.3
b	22.3
c	28.7
d	18.9
e	11.8 - 13.1
f	11.4 - 13.1
g	11.8 - 13.4
h	9.4
i	9.4

Contemporary fabrication techniques, which allow the fabrication of more specialized SiC products (beyond abrasives) include sintering, gas phase reaction, direct conversion (reaction bonding), and polymer pyrolysis. Pressureless sintering takes micron or submicron size SiC particles, adds small amounts of sintering aids (often boron or carbon), and then heats the material in a sintering furnace to temperatures of around 2000 °C. [38] This method of producing SiC yields a highly dense material with greater than 95% of the theoretical density of 3.21 g/cm^3. Pressureless sintering was used in the manufacture of the Hexoloy SA α-SiC blocks discussed in Section 2.3.2. In a reactor environment, the boron sintering aid presents a concern because the boron is localized on the grain boundaries and produces helium thanks to the sizeable (n,α) cross section of ^{10}B . Reaction bonding forms SiC by reacting SiC and particles of carbon with metallic silicon in vapor or liquid form. This method yields a lower density product which contains residual silicon which is known to degrade the mechanical performance of the silicon carbide under certain conditions. [38] The deleterious effects of excess silicon are particularly noticeable at high temperatures and/or in the presence of neutron or ion radiation.

The following paragraphs describe the manufacture of the three parts of the Triplex samples: the monolith, the composite, and the EBC.

Monolithic SiC Chemical vapor deposition (CVD) produces highly dense[11], highly pure (stoichiometric), and highly crystalline SiC. A reactant gas such as methyltrichlorosilane (CH_3SiCl_3) or ethyltrichlorosilane ($C_2H_5SiCl_3$) undergoes a decomposition reaction or a reaction with a hydrogen carrier gas, respectively, in order to deposit SiC on a pre-existing substrate. The SiC may or may not be removed from the growth substrate at the end of the process. [38, 47]

The monoliths for the Triplex samples discussed in this work were composed of β-SiC manufactured by Trex Advanced Materials using a proprietary method referred to as CVC^{TM}. The Trex CVC^{TM} method is a variation on the CVD method where highly pure SiC particles are dispersed within the reactant chemicals and deposited on a substrate

[11] Approximately 100% of the theoretical density of 3.21 g/cm^3.

or mandrel (Figure 2.7). The fine SiC particles are said to act as nucleation sites upon which additional SiC layers may deposit from the reactant chemicals. Trex claims that this method produces an equiaxial, stress-free grain structure well suited to high temperature operation. [49]

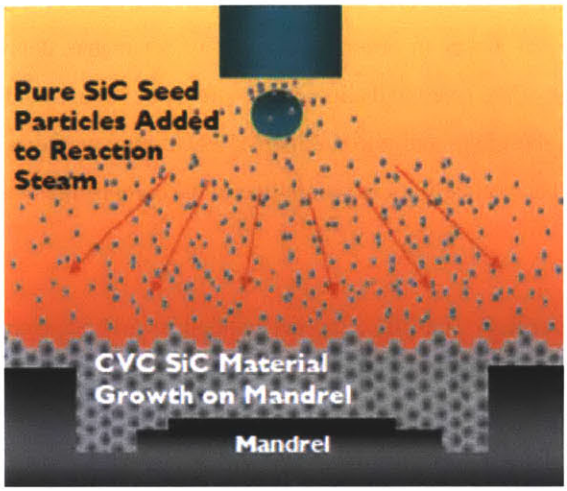

Figure 2.7: Depiction of Trex CVC (modified CVD) method used to manufacture the SiC monolith. From [49].

Fibrous SiC Polymer pyrolysis is often used to produce long SiC fibers for use in composites. The process begins with a strand of a carbon-silicon organic polymer which is cured and pyrolzyed to produce SiC.[12] Producing highly crystalline, stoichiometric fibers is very important for the chemical and mechanical stability of the fibers at high temperatures in a radiation environment. [50] It took decades to develop stoichiometrically pure fibers.

The fibers used to manufacture the composite portion of the Triplex tubes were Hi-Nicalon Type S SiC fibers produced by Nippon Carbon Co., Ltd. The Hi-Nicalon Type S fibers are an evolution of earlier fibers (Nicalon and Hi-Nicalon) thanks to different manufacturing which results in a dense (3.10 g/cm^3), highly crystalline, and highly stoichiometric fiber. Polymer pyrolysis is used in the manufacture of Hi-Nicalon Type S to transform an organic polycarbosilane (Si-C-O) fiber into crystalline β-SiC according to the generalized reaction sequence in the equation below.

$$SiC_xO_y \rightarrow SiC_{(s)} + SiO_{(g)} + CO_{(g)} \tag{6}$$

Additional curing of the fiber via electron beam irradiation is used to reduce the oxygen content in the product and to promote the formation of more Si-Si, Si-C, and C-C bonds by breaking any remaining hydrogen or hydrocarbon bonds that survived the pyrolysis step. [51, 52, 53]

Composite SiC Once the fibers have been manufactured, the fiber tows are wrapped around the monolith into a "preform". Pores and gaps in the fibrous preform are then filled with a SiC matrix material via CVI in order to produce a dense fiber/matrix composite. CVI is similar to CVD in that a reactant gas is used to deposit SiC on the prescribed substrate. When densifying the composite, the substrate is the SiC fiber preform. A common method for

[12] Pyrolysis is the thermochemical decomposition of an organic material at high temperature leaving behind mostly carbon as a residue.

industrial infiltration of composite preforms uses a technique of isothermal-isobaric CVI, a process which may take hundreds of hours. Faster methods for CVI include forced-flow CVI, thermal gradient CVI, and a combination of the two. [54] These methods may reduce the time for CVI to tens of hours.

An additional feature which may be applied to the fibers prior to the CVI treatment is that a pyrolytic carbon interphase may be deposited on the fibers in order to provide a fiber-matrix debonding and slippage mode which would aid the plastic deformation of the tubes and allow for a non-brittle failure mode. [55] The interphase allows any cracks to be directed away from the fibers and into the matrix where they may dissipate. The interphase also allows the fibers to shift with respect to each other as a load is applied to the composite layer, perhaps in the event of cracking in the monolith. [56, 47]

SiC Environmental Barrier Coating The EBC, applied as the third and outermost layer of the Triplex samples, is deposited via CVI by a company called Hyper-Therm HTC.

2.4 The Advanced Cladding Irradiation

The samples investigated in this work are part of the Advanced Cladding Irradiation (ACI) project at the Massachusetts Institute of Technology research reactor, MITR-II, which is operated by MIT's Nuclear Reactor Laboratory (NRL). This project receives support from a number of sources in industry, academia, and national labs. Nuclear materials, the cladding in particular, must thrive under corrosive conditions, high pressures, high temperatures, varying water chemistry, and neutron fluences. These effects may be tested individually, but ultimately, the cladding will experience all at once when used in a reactor. Thus, ACI was designed to simulate the conditions present in a commercial PWR.

The MITR-II is a 6 MWt light-water-cooled, heavy water reflected, thermal reactor which utilizes a U-Al plate-type fuel in an aluminum vessel capped by a stainless steel lid. It operates 24 hours a day, 7 days a week for a period of 6-8 weeks at a time. MITR-II features several in-core irradiation locations where a test rig may be inserted into a dummy fuel element for maximum flux exposure. At the irradiation location for the ACI experiment (indicated by the red arrow in Figure 2.8) when the ACI test rig is installed, the axially averaged thermal flux is 5.2×10^{12} n/cm^2-s and the fast flux (E > 0.1 MeV) is 6.5×10^{13} n/cm^2-s. Refer to Figure 2.9 for a plot of the axially averaged neutron energy spectrum in the ACI irradiation position. The power density, and therefore the flux, in the MITR-II is similar to that of a commerical LWR. MITR-II operates at atmospheric pressure with a core outlet temperature of about 50 °C.

In order to simulate PWR type conditions (temperature, pressure, water chemistry, etc.) using the low pressure, low temperature MITR-II, the ACI experiment utilizes a pressurized and heated loop with strict chemistry control which is inserted through the reactor lid and into the irradiation position as shown in Figure 2.10. The loop "thimble", shown in Figure 2.10, acts as a secondary barrier between the ACI loop coolant and the reactor coolant. A titanium tube which houses the samples is inserted inside the thimble. All ACI coolant flows within this titanium tube, and a gap between the inner titanium tube and the outer thimble is filled with CO_2 gas in order to insulate the (~50 °C) reactor coolant from the (~300 °C) loop coolant. The ACI loop coolant is pumped down the inner titanium tube and up through the sample module as depicted in Figure 2.11 .

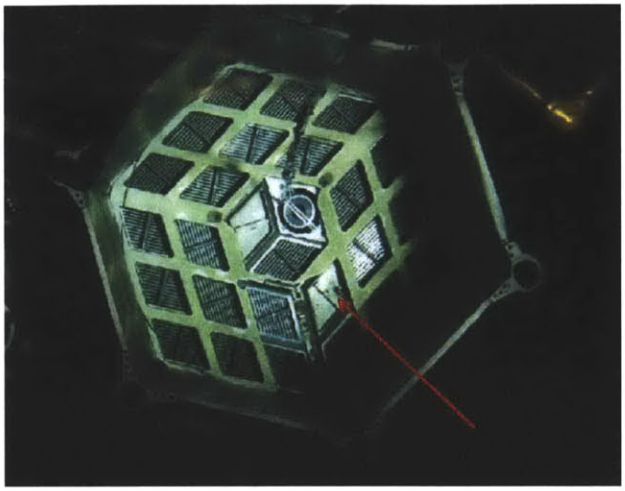

Figure 2.8: This is a top down view of the MITR-II core with the ACI irradiation location indicated by an arrow. A solid dummy element is shown in the irradiation location. The picture was taken during a reactor shutdown. [47]

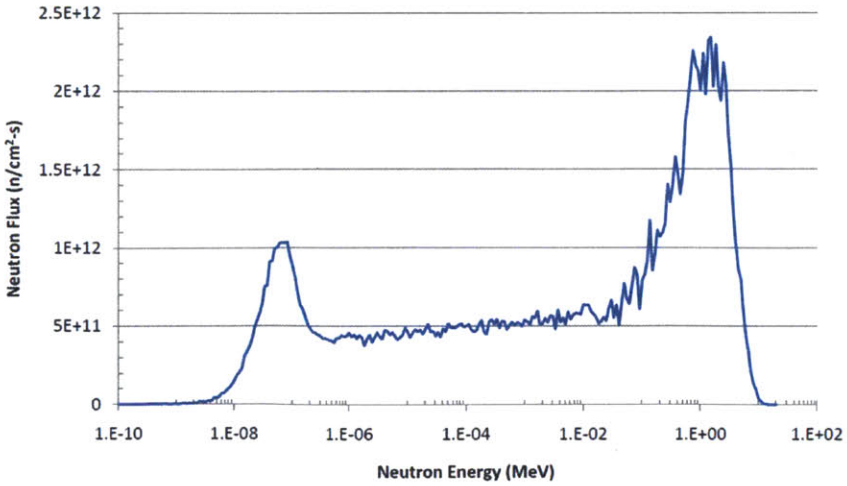

Figure 2.9: Axially averaged flux profile for the ACI irradiation location in MITR-II. Calculated with MCNP [47].

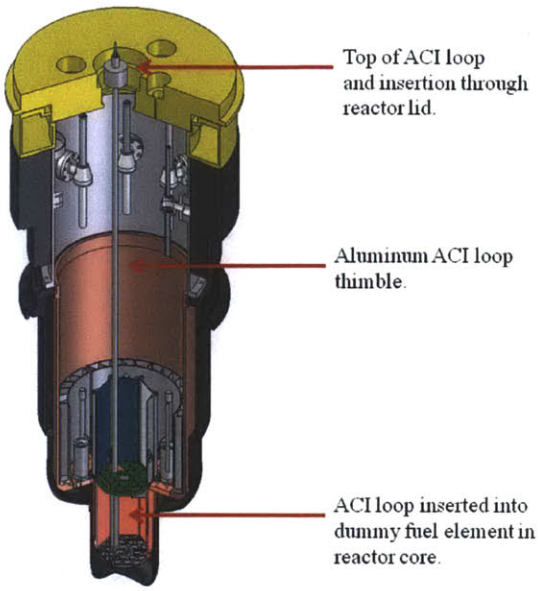

Figure 2.10: ACI loop "thimble" inserted into a dummy element at specified irradiation position in the MITR-II core. Adapted from [47].

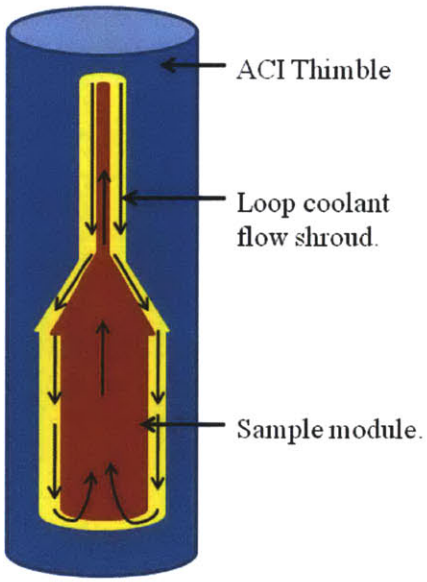

Figure 2.11: Schematic of coolant flow in the ACI test loop. Coolant flows down the titanium tube (yellow), around the outside of the sample module (red). Coolant is then forced up through the middle of the sample module which may house different types of samples: SiC tubes, blocks, transmission electron microscopy (TEM) discs, etc.

The coolant inside the ACI loop is maintained at 300 °C by programmable heaters. Even if the reactor were to shut down and its coolant were to drop below its normal operating temperature of ~ 50 °C, the heaters would respond to maintain loop temperature. A series of pumps keep the loop pressurized to 10.3 MPa, and a circulating pump maintains a coolant flow rate of 0.25 kg/s. The loop pressure of 10.3 MPa is notably lower than the operating pressure of a PWR (15.5 MPa). This pressure was chosen during the design of the loop so as to minimize the thickness of the

loop tubing in order to ensure that the loop fits within in-core space restrictions. Since there is a hydrogen overpressure in a commercial PWR, the ACI loop contains 25 cc/kg of dissolved H_2 in the coolant. This reduces the presence of free oxygen and, in a commercial reactor, helps to protect the Zircaloy cladding from corrosion. This should benefit the SiC materials as well. For a more detailed description of the ACI test loop, its controls, and its operation, see References [45] and [47].

3 Mechanical Testing of SiC Triplex Tube Samples

In any LWR, the fuel cladding experiences various mechanical and thermal stresses. These stresses may change over the course of a cycle length and are subject to variation due to transients. As was discussed in Sections 1.1.1 and 1.3.2, the cladding experiences internal pressure due to the helium fill gas which pressurizes the cladding to 2 MPa. Counter balancing the internal pressurization of the cladding is the external pressure applied by the reactor coolant, which in a PWR, is on the order of 15 MPa. Initially, this external pressure puts compressive stresses on the cladding.[13] When at operating temperature and as burnup proceeds, the evolution of fission gases will further pressurize the inside of the cladding and net internal pressurization may occur. That is, the internal pressure may become greater than the external pressure (15 MPa) from the reactor coolant. In an accident scenario, cladding rupture due to internal pressurization is a principal concern. The cladding may be weakened during a LOCA as a result of increased fuel/cladding temperature and high temperature oxidation of the cladding. Higher temperature will also increase the internal pressure of the fuel rod as a result of increased fission gas production, increased gas pressure, and direct PCMI. RIAs may result in strong PCMI because of the rapid expansion of the UO_2 fuel due to the acute deposition of energy (and heat) from the reactivity accident. Additionally, when fuel is unloaded from the core during a refueling operation, the external pressure on the fuel will no longer be 15 MPa, but it will now be 1 atm (0.1 MPa). This net internal pressure puts the cladding in tension. Thus, it is important to establish the tensile hoop strength of the tubular Triplex fuel cladding prototypes via internal pressurization.

3.1 Hoop Test Rig

The hoop strength of two Triplex cladding prototypes (one irradiated and one un-irradiated) were tested via internal pressurization at room temperature. A cylindrical polyurethane plug with a diameter slightly smaller than the inner diameter of the Triplex tube and a length of 0.75 inches was inserted into the sample. The sample was then loaded onto a ram connected to a load sensing cell, and a second ram connected to a hydraulic pump was then used to apply axial pressure to the elastomeric insert (polyurethane plug). (Figure 3.1) As more and more force was applied, the plug expanded until it began to pressurize the inside of the tube. Only forces directed radially outward were transmitted from the plug to the specimen. Any axial force transfer is negligible and can be ignored.

The apparatus uses one load sensor and three micrometers. Two micrometers detect radial expansion of the tube and one measures the axial displacement of the hydraulic ram. The two micrometers used for the radial measurements each had two points of contact with the sample and those points were centered at the same axial location as the plug relative to the Triplex sample. The load cell measured how much force the hydraulic ram applied to the plug. CTP built and supplied the load frame for the hoop test rig, which was modeled after a similar apparatus used at the Oak Ridge National Laboratory. [58]

Figure 3.2 shows pictures of the actual hoop test apparatus used for the tests. The blue load cell, to which a stationary ram is attached, is an Interface 1200 load cell rated at 5000 lbf connected to an Interface 9820 strain gauge

[13] Note that SiC is stronger in compression than in tension.

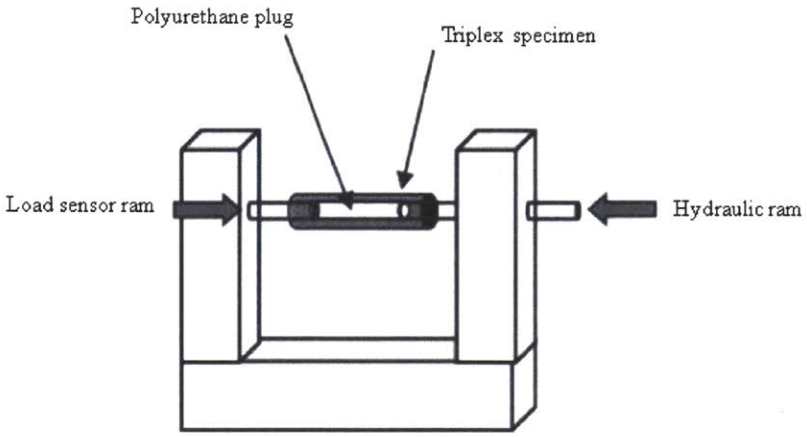

Figure 3.1: Simplified illustration of the hoop test apparatus. Adapted from [57].

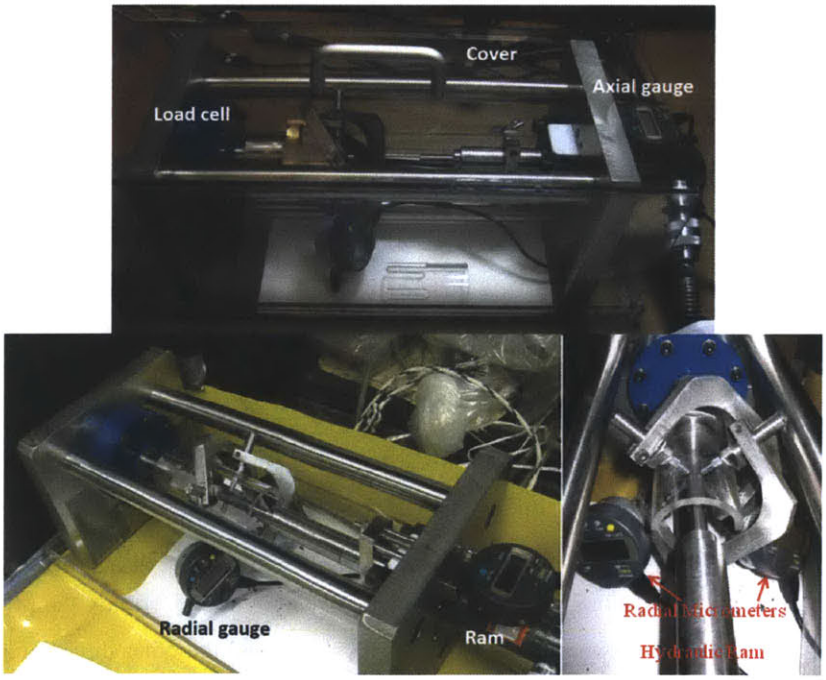

Figure 3.2: Hoop test rig. Load frame, digital micrometers, load cell, and hydraulic ram.

transducer with an accuracy of ± 2 lbf. The transducer sent an analog singal to an analog-to-digital converter which was read by a PC via a program written in LabView. The three micrometers are Mitutoyo ID-C digital gauges also connected to a PC with accuracies of ± 3 μm. The hydraulically actuated ram is moved via a hand-operated Simplex P22 10,000 psi hydraulic pump (not pictured). In order to help verify the load cell calibration, the hydraulic pump is connected to a mechanical test gauge. The data from the load cell and the three digital micrometers were recorded on a PC at a sampling rate of 5 Hz using an interface constructed in LabView.

3.2 Hoop Test Experimental Procedure

During preparation for insertion into the ACI loop, some Triplex tubes had been cut on both ends. This left the composite exposed to coolant, and a number of tube samples suffered preferential corrosive attack at the ends while in the ACI loop. When weight loss measurements were made in a previous work [47], 1/4 of an inch was removed from the top and bottom of each tube to remove the damaged ends. For consistency, 1/4 of an inch was also removed from the top and bottom of un-irradiated samples as well. Photographs of each sample were taken before and after the hoop test.

Once the sample was loaded on the load cell ram, the polyurethane plug was inserted. The radial micrometers were then centered over the plug, and then the hydraulic ram was moved into slight contact with the plug. The data acquisition was started, and then the hand operated lever on the hydraulic pump was used to slowly and steadily pressurize the plug. Increasing pressure was applied until the sample ruptured and the applied force dropped sharply. Once the sample had ruptured, additional ram displacement was used to demonstrate that the tube could not hold additional pressure.

The failed sample was then photographed while still on the hoop apparatus in its as-failed condition. The hydraulic ram was then retracted and the plug was removed and reused provided it had not undergone significant plastic deformation.

3.3 Hoop Test Data

A number of monolith only, duplex, and Triplex samples had been hoop tested in earlier work by Carpenter [47]. The work presented here has produced data for two more Triplex samples: one sample had been in-core in MITR-II for 9 months and the second sample was as-fabricated. Several samples from Carpenter [47] will be used for comparison and to help identify general trends; however, due to the statistical variation in the manufacture of all ceramics (Weibull statistics) and the limited number of samples tested, the data have significant variation.

Table 3.1 summarizes the dimensions and construction of five hoop tested Triplex samples. The samples highlighted in **bold** type (06-B and 25-2) were hoop tested in this work, and the other three samples (04-A, 04-B, and 06-C) were hoop tested by Carpenter [47] and will be used for comparison purposes. The length of sample 06-B is shorter than the others because an additional 1/4 inch had been removed for SEM analysis. (See Section 3.4.2 for SEM micrographs of hoop tested specimens.)

Table 3.1: Construction and dimensions of Triplex samples. Samples highlighted in **bold** type were hoop tested in this work, and the other three were hoop tested by Carpenter. The dimensions listed were the dimensions prior to hoop testing. *Sample 25-2 was in-core for 9 months. The total estimated fluence was 0.99 x 10^{25} n/m^2 and the estimated displacements per atom was 0.99 dpa. See Section 3.3.2 for an explanation of the dpa estimate method.

	Monolith Type	Composite Fiber Type / Matrix	EBC	Outer Diameter (mm)	Inner Diameter (mm)	Length (mm)	Months In-Core
04-A	Trex	Hi-Nicalon-S / CVI	HyperTherm CVI	10.10	8.36	35.80	0
04-B	Trex	Hi-Nicalon-S / CVI	HyperTherm CVI	10.10	8.36	35.80	0
06-C	Trex	Hi-Nicalon-S / CVI	HyperTherm CVI	10.03	8.38	35.80	0
06-B	**Trex**	**Hi-Nicalon-S / CVI**	**HyperTherm CVI**	**9.99**	**8.33**	**29.45**	**0**
25-2	**Trex**	**Hi-Nicalon-S / CVI**	**HyperTherm CVI**	**10.10**	**8.26**	**35.80**	**9***

The hoop test data for sample 06-B, an un-irradiated Triplex sample, is shown in Figure 3.3. The curve for axial displacement represents the displacement of the hydraulic ram from its initial position which had been zeroed when it was just barely in contact with the plug. Between approximately 40 and 50 seconds, the hydraulic pump lever was slowly depressed and the hydraulic ram was displaced rapidly (and nearly linearly) with only a small increase in force measured by the load cell. Over this period of time, the plug was compressed elastically and was not yet in full contact with the inner diameter of the tube sample. The time and force at which the plug was judged to have begun full contact and loading of the sample were 78.1 seconds and 205.99 N respectively. This judgment was made based on the beginning of a steeper slope to the Force vs. Time curve, and the force of 205.99 N is consistent with the onset of plug-tube loading from previous experiments. The curve labeled "Radial Displacement 2" is one of the two radial measurements taken at the same axial location along the tube. The other radial micrometer was not working at the time of the test. Also, note that the slight jogs in the Force vs Time curve (also seen in the Axial Displacement vs Time curve) were due to the pumping action of the hand-actuated hydraulic pump.

At approximately 140 seconds, the specimen failed, as evidenced by the sharp drop in the Force vs Time curve and the sharp increases in the Radial and Axial displacement curves. The ram was pumped further at ~ 160 seconds showing that the tube could not withstand additional force. Between 160 and 180 seconds some portion of the tube was able to support additional force as evidence by the slight bump in the force curve. Beyond 180 seconds the ram displacement was stopped, and slight relaxation in the force curve is evident as a result of the relaxation of the tube and slight decreases in pump pressure over time due to leakage of the pump's check valve. The force at rupture was taken as the highest force achieved prior to the sharp drop in the force curve. For sample 06-B, a peak force of 1828.83 N was achieved at a time of 143.1 seconds into the test. In order to determine the *true* applied force at rupture, the force at the onset of plug-to-tube contact is subtracted from the force at failure. Thus, for this sample the true applied force at failure is 1828.83 N - 205.99 N = 1622.84 N. A method for relating this force to the hoop strength will be discussed in the next section.

The hoop test data for the irradiated (9 months in-core, 0.99 dpa) Triplex sample 25-2 is shown in Figure 3.4. Similar to Figure 3.3, the ram axial displacement increases steeply until the plug has begun to load the inner diameter

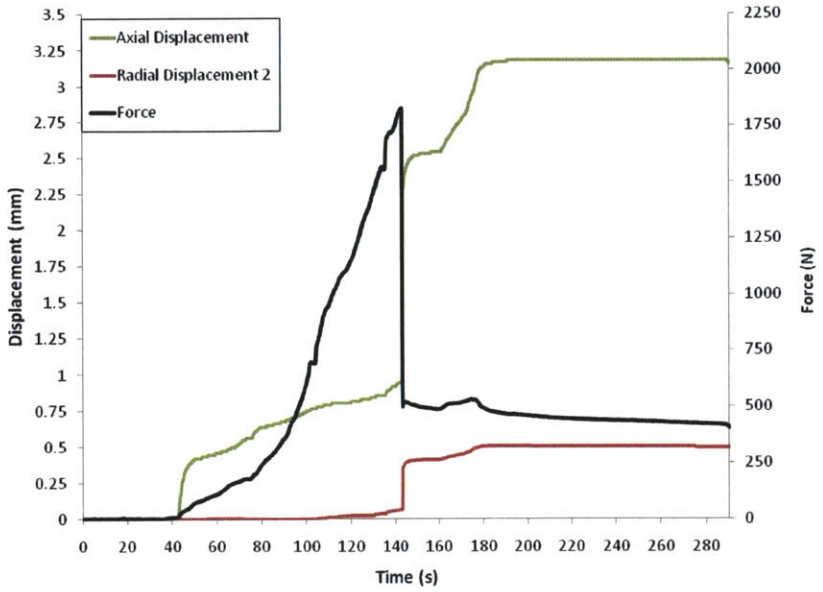

Figure 3.3: Hoop test data for un-irradiated Triplex sample 06-B.

of the tube at 83.1 seconds and 160.75 N. The force continues to rise until rupture at just after 250 seconds at a force of 1250.02 N. The true applied force was 1250.02 N - 160.75 N = 1089.27 N. Slight ram displacement continued beyond the point of rupture, and demonstrated that the tube could not support additional force. The force curve continued to relax as the tube and plug settled and slight pressure leaked from the pump check valve.

3.3.1 Calculation of Hoop Stress from Hoop Test Data

Some force is required simply to compress the plug into initial contact with the tube inner diameter. This force is not pressurizing the tube, it is compressing the plug so that it begins to make contact with the tube inner surface. As such, this force required to compress the plug into contact with the tube inner surface, F_{plug}, is subtracted from the peak force, F_{max}, measured from the plots above (Figures 3.3 and 3.4) and an *adjusted* maximum force, F_{adj}, is obtained.

$$F_{adj} = F_{max} - F_{plug} \tag{7}$$

The plug is assumed to be linearly elastic, homogeneous, and isotropic such that it may be treated as an incompressible fluid so that the pressure applied to the plug is also the internal pressure applied to the tube inner surface. In order to obtain the internal pressure at failure, P, the adjusted maximum force, F_{adj}, is divided by the area of the plug, A_{plug}:

$$P = \frac{F_{adj}}{A_{plug}} \tag{8}$$

Since the thickness of the Triplex samples is not negligible compared to the radius of the samples, the tubes should be treated as thick-walled cylinders. [59] The hoop stress is found from elasticity theory to be a function of the radial distance, r, from the centerline of the tube specimen. For composite specimens with a CVD inner monolith, the

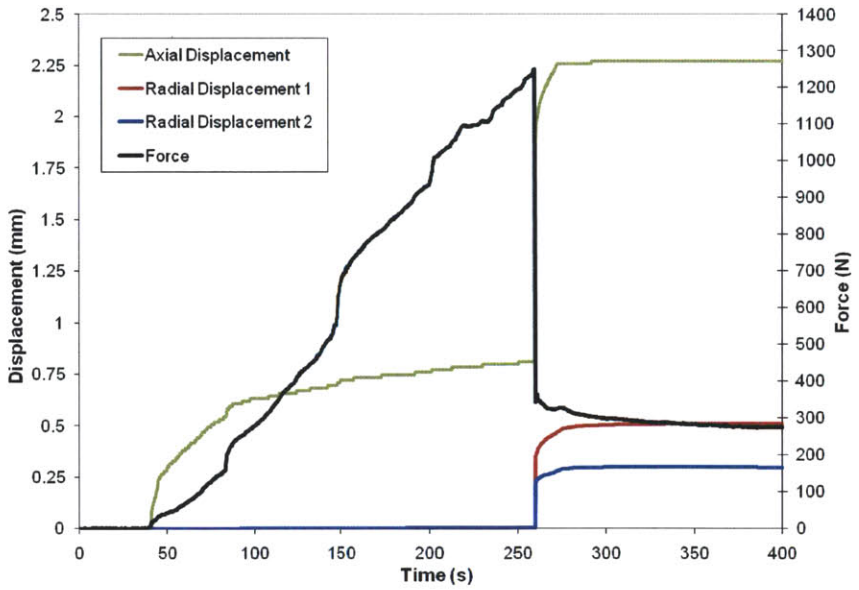

Figure 3.4: Hoop test data for Triplex irradiated sample 25-2.

inner surface is taken as the most likely site for crack initiation. This assumption is valid for three reasons: 1.) the maximum stress occurs at the inner surface, 2.) the dimpled surface of the specimen inner diameter may act as a stress concentrator, and 3.) experiments on similar materials have taken this approach. [57, 60, 61] The dimpled surface may be a result of slight roughness on the surface of the mandrel onto which the SiC was deposited during the CVD process. Figure 3.5 shows an SEM micrograph of the dimpled inner surface of the monolith. The hoop stress at failure, σ_θ, may be taken as:

$$\sigma_\theta(r) = \frac{r_i^2 P}{r_o^2 - r_i^2}(1 + \frac{r_o^2}{r^2}) \tag{9}$$

where r_i and r_o are the inner and outer radii of the tube respectively (prior to hoop testing) and P is the internal pressure calculated in Equation 8. [57] Since the maximum hoop stress has been assumed to occur on the inner surface of the sample, the variable r is set equal to r_i, resulting in a slight modification of Equation 9:

$$\sigma_\theta = \frac{r_i^2 P}{r_o^2 - r_i^2}(1 + \frac{r_o^2}{r_i^2}) \tag{10}$$

This equation (Equation 10) was used to calculate the hoop stress at failure.

3.3.2 Estimate of dpa

When comparing the radiation damage accumulated by different materials (perhaps from different experiments), a metric other than fluence is required because the fluence energy spectra may differ between experiments and because radiation damage accumulates in different materials at different rates. In SiC, and many other engineering materials, radiation damage is primarily by displacement of atoms from their lattice sites due to collisions with neutrons. Thus, a measure of the displacements per atom (dpa) in the sample has become the metric of choice for quantifying the

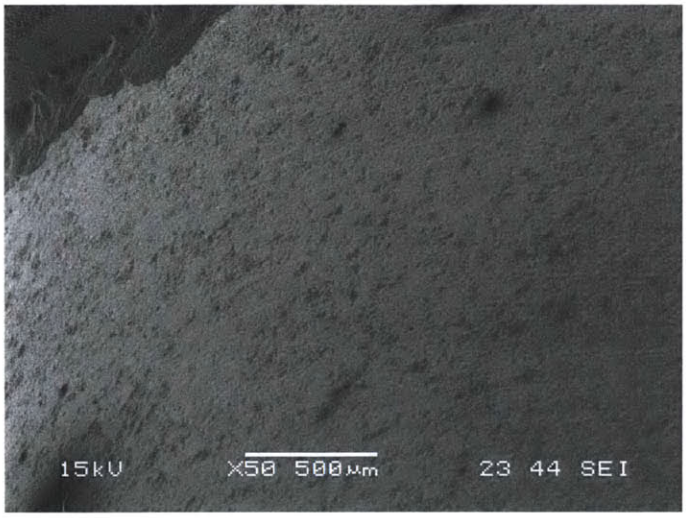

Figure 3.5: Sample 06-B dimpled monolith inner surface.

extent of radiation damage. Displacement damage is a threshold event requiring that a certain amount of energy be transferred from the incident neutron to the target atom in order to displace it from its lattice site. Atoms may also be displaced due to neutron capture as a result of the recoil the atom experiences when it relaxes from an excited state via the emission of a gamma particle.

A couple of methods are widely used for converting neutron fluence to dpa. Heinisch *et. al.* [34] tabulated displacement cross sections for displacement damage in SiC, and these data have been used with MCNP calculations to calculate a reaction rate for dpa due to a fast neutron fluence (E > 0.1 MeV). This was the method used by Carpenter [47]. It should be noted that the cross sections computed by Heinisch *et. al.* were based on dpa rates typical of LWRs: 2.4 dpa/effective full power years (EFPY) in BWRs, and 3.1 dpa/EFPY in PWRs. Since the spectrum in the MITR-II is harder than the spectrum in a typical LWR, this treatment may underestimate displacement damage in the samples.

Snead and others have suggested a dose equivalent of 1 x 10^{25} n/m^2 (E > 0.1 MeV) = 1 dpa in SiC. [42] This dose equivalent was used to convert fluence to dpa in this work. For example, if a sample saw 100 MWd, and full power for MITR-II is 4.8 MW[14], then the effective full power days (EFPD) is 20.8. The axially averaged fast flux (E > 0.1 MeV) in the MITR-II core at the ACI irradiation position was calculated to be 6.5 x 10^{13} n/cm^{2}s (6.5 x 10^{17} n/m^{2}s). Converting 20.8 days to seconds and multiplying by the fast flux (6.5 x 10^{17} n/m^{2}s) gives a fluence of 1.17 x 10^{24} n/m^{2}or 0.117 dpa in SiC.

3.3.3 Hoop Strength Data and Discussion

Section 3.3 presented the raw data collected during the hoop test and how to interpret it. Section 3.3.1 described how the data from Section 3.3 were used to calculate the maximum hoop strength of the samples. This section (Section 3.3.3) will present the calculated hoop strengths for the samples tested in this work, as well as the calculated hoop strengths of samples tested by Carpenter [47]. The constructions of these two groups of samples is the same and can

[14] At the time of the test, full power for the MITR-II was 4.8 MWt. It has since been uprated to 6 MWt.

Table 3.2: Pressures and hoop stresses at failure for 5 Triplex samples. Samples highlighted in **bold** type represent samples tested in this work. The remaining three samples were tested in Carpenter [47].

	Time In-Core (months)	MWd	dpa	Internal Pressure at Failure (MPa)	Hoop Stress at Failure (MPa)
06-B	**0**	**0**	**0**	**30.46**	**169.10**
25-2	**9**	**848**	**0.99**	**20.44**	**103.34**
04-A	0	0	0	46.84	256.21
04-B	0	0	0	51.28	279.28
04-C	0	0	0	41.27	231.23

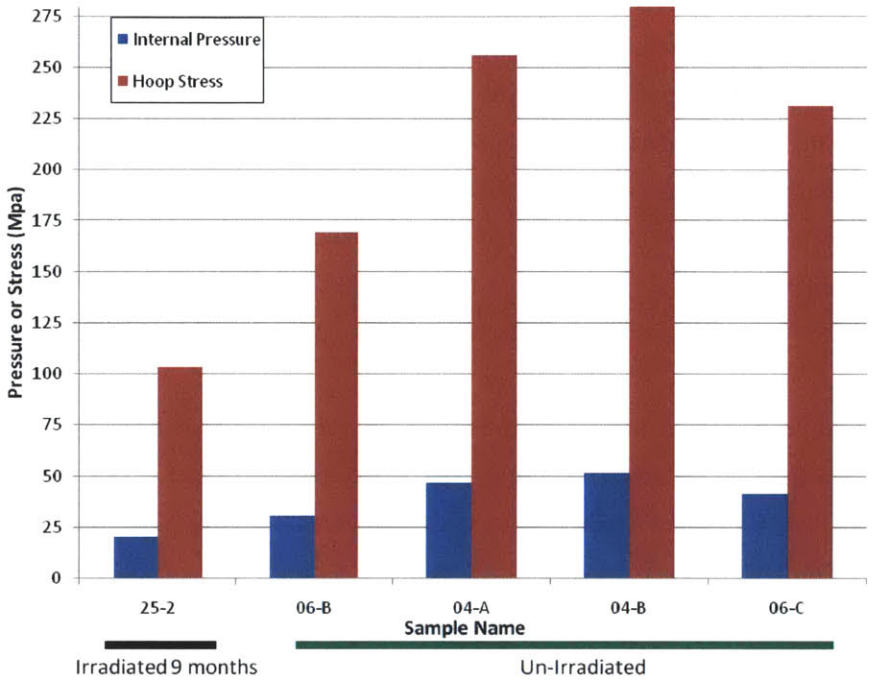

Figure 3.6: Internal pressure and hoop stresses at failure for 5 Triplex samples. Sample 25-2 was irradiated in-core for 9 months and the other four samples were not irradiated.

be found in Table 3.1.

Table 3.2 summarizes the internal pressures and hoop stresses at failure for the five samples considered here. Figure 3.6 represents the same data in graphical form. The irradiated sample (25-2) clearly possessed less hoop strength and ruptured at a lower internal pressure than the four un-irradiated samples. This result is consistent with findings in Carpenter [47] and Feinroth *et. al.* [46] for similar Triplex samples. That said, the volume of samples tested and the variations in manufacturing techniques between samples makes predicting the *amount* of tensile strength degradation between un-irradiated and irradiated Triplex samples difficult. It is critical to note that even in as-fabricated form, the specimens are not perfect. For example, 06-B had a radially varying wall thickness: 1.02 mm in one location, and 0.64 mm in another location. This is almost certainly responsible for sample 06-B's having a lower hoop strength than the virtually identical samples tested by Carpenter. Manufacturing variations play a role in the different mechanical strengths of the samples.

It is to be emphasized that only *cautious* descriptions of possible mechanisms underlying the mechanical degradation due to neutron irradiation in a corrosive environment may be made. Similar silicon carbide composites have been studied by other authors over the years, but no firm conclusions as to the underlying mechanisms of degradation in SiC_f/SiC composites have been drawn. The purity, crystallinity, and manufacturing of the samples, and the irradiation environment under which they were tested all play a role. The remainder of this paragraph lists known factors relevant to the mechanical properties of SiC and SiC_f/SiC composites. Free silicon in a SiC structure provides a site for fracture initiation. [62] Low purity fibers, with low density, and low crystallinity (e.g. Nicalon and Hi-Nicalon) may densify and harden with irradiation which can induce stress within the matrix, as the matrix itself (a higher grade of SiC) tends to swell with irradiation. [55] This promotes the formation of microcracks within the matrix. Low purity fibers with significant oxygen content have displayed poor dimensional and mechanical stability with irradiation. [63] Numerous papers by the same group of authors have argued the importance of the interfaces between the pyrolytic carbon interphase and the fibers and the matrix for determining the overall mechanical performance of the fiber/matrix composite. [53, 50] Radiation damage within SiC irradiated at lower temperatures is primarily by the accumulation of individual point defects (vacancy/interstitial formation); however, small interstitial clusters may also contribute to radiation damage manifested as swelling. [64, 65, 66] Undoubtedly, other effects may play a role in the irradiation behavior of SiC and SiC_f/SiC composites; and identifying which of the possible effects is present in a sample is challenging.

The severe instabilities facing the low purity fibers (Nicalon and Hi-Nicalon) should not be as prevalent for the Triplex samples tested here, which used Hi-Nicalon Type S (HNTS) fibers. The HNTS fibers have demonstrated good mechanical and dimensional stability in tests by other authors. [53, 56] That said, there are known mismatches between properties of the HNTS fibers and the CVI SiC matrix despite both being β-SiC. For example, HNTS fibers are reported to have a higher coefficient of thermal expansion (CTE) than CVI SiC. [56] At elevated temperature, the disparity between the CTEs may generate stresses betwen the matrix and the fibers which, if not relaxed, may promote crack initiation during the room temperature hoop tests. A mismatch in the irradiation-induced swelling due to differences in defect accumulation between the fibers and the matrix is also possible. [56] If there were a difference in swelling between the fibers and matrix, this would cause localized stresses and may, on its own, initiate microcracks, reducing the hoop strength of the irradiated samples. Differences in the behavior of the fibers and matrix material have been recorded to result in de-bonding between the matrix and the fiber during irradiation which tends to reduce the strength of the composite. [55]

Corrosive attack at the tube ends was noticed for the irradiated sample 25-2. The formation of SiO or SiO_2 would constitute an impurity and would compromise the dimensional and mechanical stability of the composite. The affected ends were cut off prior to hoop testing, but it is possible that water penetrated the porous composite layers. Silicon oxides are amorphous, experience densification with irradiation, and generally degrade the strength of the SiC host. [63]

The CVD β-SiC monolith may have experienced degradation as result of radiation effects magnified by the presence of impurities. While CVD SiC is expected to be highly pure, the purity of the samples could not be verified since

an elemental analysis was not performed in this work. Free silicon, in particular, can greatly reduce the strength of β-SiC under irradiation. [62] In the reaction bonded β-SiC tested in Reference [62], it was found that the degradation in the fracture strength was due to differential irradiation-induced swelling in the lattice parameters of the free Si lattice and the host SiC lattice. This resulted in misfit strains where cracks initiated at free silicon particles. The CVD SiC tested in this work was likely of higher purity than the reaction bonded SiC in [62] (which had ~ 10% free Si), but this type of mechanism may still bear some responsibility for the mechanical degradiation of the irradiated CVD monolith.

Not only do the fibers and the matrix need to have compatible properties, but the composite and the monolith should also possess compatible thermal, chemical, and mechanical properties. Another contributor to the decrease in hoop strength of the irradiated Triplex sample is that the monolith and composite may behave differently as a result of the thermal, corrosive, and radiation stimuli. In a limited study, Feinroth *et. al.* determined that applying a composite layer to a monolith might increase the strength by ~22-37% above the strength of the monolith alone. [46] The data from Carpenter [47], were less conclusive, and the extent of load sharing between the monolith and composite layers is uncertain. Given that there is different behavior between the fibers and the matrix, it is likely that there is different behavior between the composite (fibers and matrix) and the monolith. If the bonding between the composite and monolith is compromised by radiation effects (such as swelling), differences in thermal expansion, or corrosion, this would reduce the strength of the Triplex sample as a whole.

A few studies, such as those by Dienst [67, 68], show significant decreases in the fracture strength of CVD SiC at doses nearing 10 dpa. Since sample 25-2 was only irradiated to roughly 1 dpa, a direct comparison is not appropriate. However, a large body of data compiled by Snead *et. al.*, show minimal changes in the fracture strength of a broad group of CVD SiC samples irradiated at relevant temperatures and doses. [38] Since the majority of the strength of the Triplex design seems to come from the monolith [46], the monolith would have to degrade considerably for the hoop strength of the Triplex tube as a whole to degrade significantly. The hoop strength of sample 25-2 (irradiated to 0.99 dpa) is less than 50 % of the average hoop strength of the un-irradiated samples in Table 3.2. This extent of degradation for the types of high-grade SiC materials used in the Triplex samples is not found in the literature. The literature data were not, however, obtained for samples irradiated in a corrosive environment. These ACI data *were* obtained for samples irradiated in a corrosive environment. One possibility is that surface corrosion of the monolith inner diameter acted to further concentrate stresses on the inner surface. As was mentioned in Section 3.3.1, it is believed that the maximum hoop stress occurs on the inner surface and that the dimples on the inner surface concentrate this stress. Henager *et. al.* reported significant pitting in monolithic CVD SiC samples after 4000 hours of exposure under a corrosion study using water at 300 °C and 10 MPa. [69] These are virtually the same coolant conditions as those found in the ACI loop. By approximately 5400 hours, Henager *et. al.* reported that the pitting was removed, and general corrosion with noticeable weight loss was then observed. Sample 25-2 was exposed in the ACI for approximately 6500 hours and was likely to have experienced these same phenomena. Henager and co-workers reported that the pitting forms with little or no weight change, a finding supported by the weight change analysis of the monolithic samples in [47]. Localized corrosive pitting, in addition to the existing dimples, may help to account

for the significant degradation of the hoop strength in the irradiated Triplex samples.

As Zircaloy currently represents the standard for LWR cladding, a comparison is in order. First, the strength of Zircaloy is highly dependent on temperature. At 280 °C, Zircaloy-2 has an ultimate tensile strength (UTS) of 320 MPa and 430 MPa for unirradiated and irradiated ($2.7x10^{20}n/cm^2$) Zircaloy-2 respectively. [70] This strength decreases with increasing temperature, and the UTS of Zircaloy at 280 °C is roughly half of its UTS at room temperature. [70] A few Zircaloy tubes were irradiated in the ACI and are mentioned in Carpenter [47]. Un-printed data for one of these tubes (sample "N1-1") shows that the tube remained intact even under an applied hoop stress of 436 MPa. The strength of SiC has a much lower temperature dependence than Zircaloy, but the hoop strength for the irradiated Triplex sample from this work (103.3 MPa) cannot match the room temperature hoop strength of a Zircaloy cladding. Some irradiated Triplex samples of a different construction tested by Carpenter [47] meet or exceed the estimated hoop strength for Zircaloy at 300 °C. SiC composites appear to have the potential to exceed Zircaloy's strength, especially at elevated temperature, but more experiments are needed to arrive at a suitable design and a consistent manufacturing method.

3.4 Fracture Mechanisms in Triplex Cladding

The propagation of cracks though the Triplex cladding system can be observed on both a macro and micro scale.

3.4.1 Visual Inspection

Various fracture patterns are evident even under simple visual inspection. Figure 3.7a shows the crisscrossing seams of the composite weave under the EBC. In Figure 3.10c sample 06-B displays a characteristic fracture pattern after hoop testing to failure. At both ends ends there are "V"-shaped cracks connected by a straight axial crack which has broken through all layers of the sample. Notice also that the fractured pieces are still connected as a whole, unlike the fractured monolith-only samples tested by Carpenter [47]. Figure 3.8 shows pictures of a sample ("T-2") constructed with a monolith only. Prior to hoop testing, the sample appears very similar to the Triplex-type samples. After failure, however, T-2 has not maintained any integrity and clearly exhibits brittle failure.

The crisscross pattern of the fibers is not visible in sample 25-2 (Figure 3.9a and 3.9b) because its EBC is thicker than the EBC applied to sample 06-B. Similar fracture patterns were observed in sample 25-2 (Figures 3.9c and 3.9d). At the center of the tube, where the polyurethane plug is placed, the pressure and energy for fracture are the greatest, and when the tube fails, the pressure is high enough to rupture the tube at high angles to the directions of the fibers. As the crack propagates axially, away from the center of the tube, the fracture driving force decreases and the crack then propagates along the directions of least resistance — parallel to the directions of the fibers which are woven in a crisscross pattern. When the crack propagates along the fibers, the fibers themselves are not ruptured, but the crack is directed through the weaker matrix and around the fibers. When compared to the brittle failure of the monolith-only samples, the Triplex samples exhibit what has been called a "graceful" failure mode. Unlike the monolith-only samples, when the Triplex samples failed, they maintained some structural integrity, and it appears that they should be able to prevent the release of UO_2 fuel pellets while maintaining a coolable geometry.

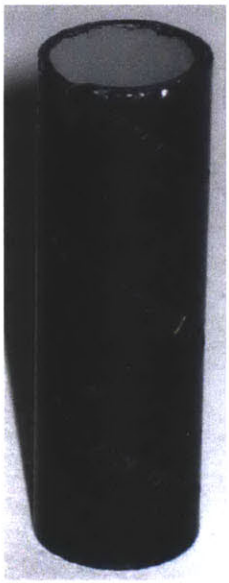

(a) 06-B Before hoop test.

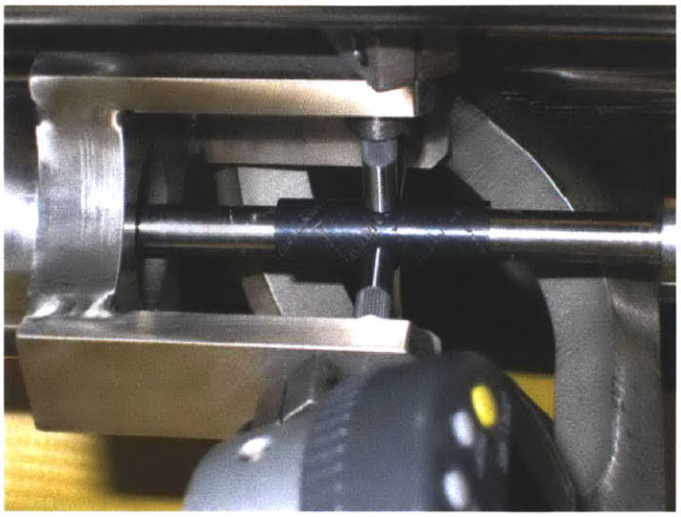

(b) 06-B Mounted on hoop test rig.

(c) 06-B after hoop test.

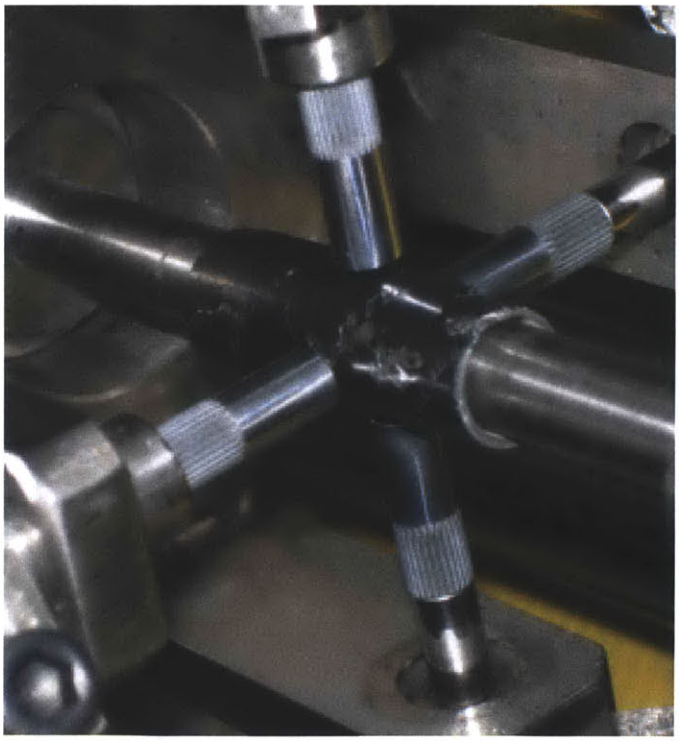

(d) 06-B after hoop test while still mounted on hoop test rig.

Figure 3.7: Sample 06-B before and after hoop testing.

(a) Monolith only sample T-2 before hoop test.

(b) Monolith only sample T-2 after hoop test. Catastrophic brittle failure.

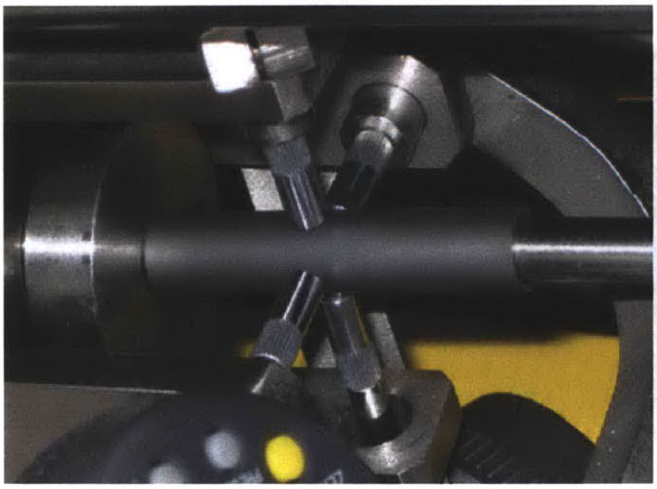

(c) Monolith only sample T-2 loaded on hoop test rig prior to failure.

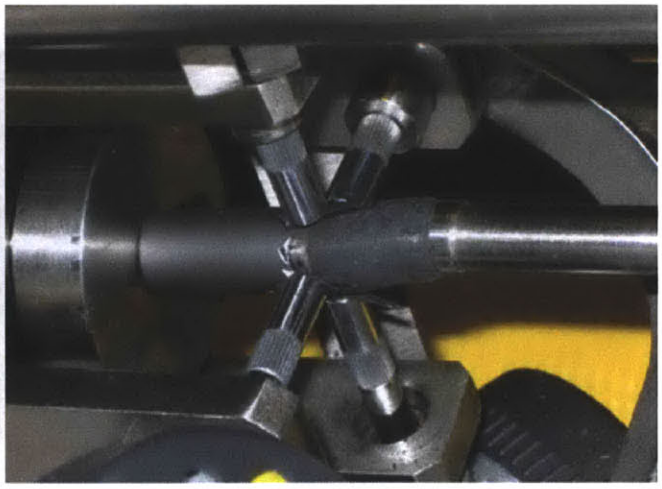

(d) Monolith only sample T-2 after failure.

Figure 3.8: Images of sample T-2 constructed with a monolith only, no composite construction. Brittle failure. Adapted from [47].

(a) 25-2 before hoop testing. The weave patter is not visible through the thicker EBC.

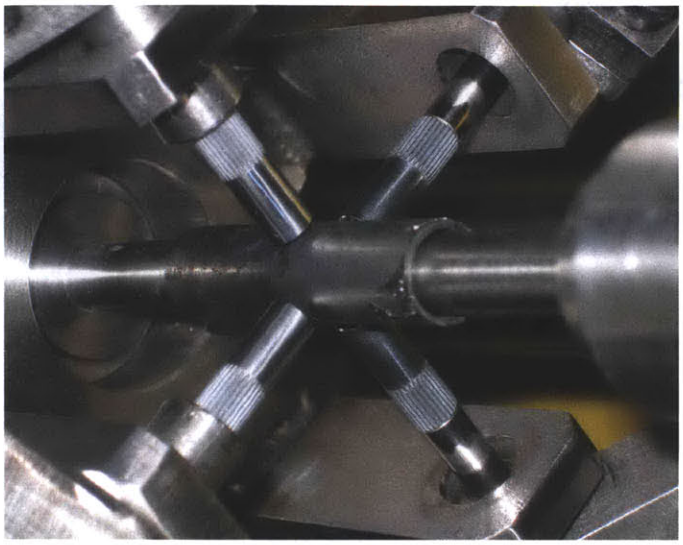

(b) 25-2 mounted on the hoop test rig prior to failure.

(c) 25-2 after failure displaying "v"-shaped cracks at both ends and an axial crack connecting the two ends.

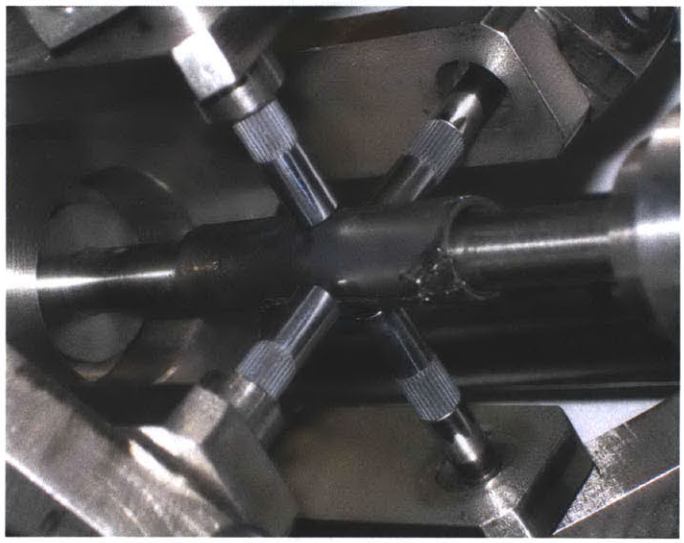

(d) 25-2 after failure while still mounted on the hoop test rig.

Figure 3.9: Images of Triplex sample 25-2 before and after hoop testing.

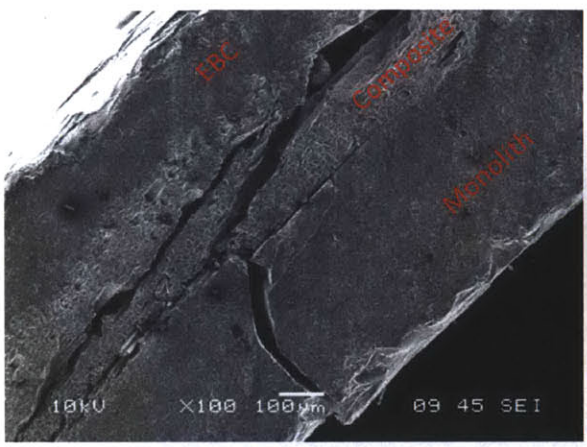

(a) SEM of sample 06-B after hoop testing.

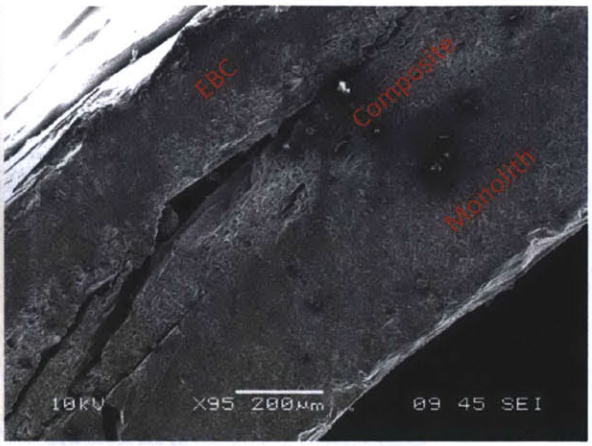

(b) 06-B after hoop test. Image continues from the right side of Figure 3.10a.

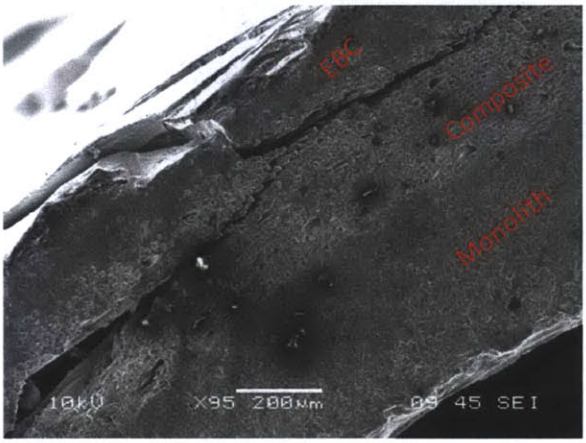

(c) 06-B after hoop test. This figure continues from the right of Figure 3.10b.

Figure 3.10: SEM of sample 06-B after hoop testing. Crack initiates on monolith inner face, traverses the composite layer, exits the EBC.

3.4.2 SEM of Hoop Tested Samples

SEM was used to take a closer look at the failed Triplex specimens. Several interesting fracture patterns were observed and the propagation of cracks could be followed from their point of origin to their point of termination. Figure 3.10 shows the propagation of cracks from their origin, on the inner monolith, to their termination, when they breach the outside of the tube. As was mentioned in Section 3.3.1 the inner monolith surface was taken as the point of greatest hoop stress, and the SEM images support the claim that this is where the initial fracturing originates. In Figure 3.10a the monolith ruptures and the crack breaks straight through the monolith, perpendicular to its surface. The energy from this crack then transfers into the composite layer where it begins to dissipate by moving laterally through the composite. Some debonding between the composite and the monolith is evident closest to the point where the crack from the monolith first contacts the composite layer. Looking from left to right in the micrograph in Figure 3.10b, the crack slowly propagates radially outward as it moves laterally away from the initial crack in the monolith. As the

crack continues to move laterally through the composite, it propagates radially outward and dissipates energy now via the breaking of the interface between the matrix and the fibers (Figure 3.10c). Eventually, when the energy has been reduced, the crack propagates through the matrix/fiber interface one fiber at a time. Once the crack has reached the fringes of the composite layer, it breaches the EBC (Figure 3.10c).

Micrographs from the Triplex sample 04-A, which was hoop tested in [47], but whose micrographs were obtained in this work, shows similar crack morphologies in Figure 3.11. Again, the monolith fractures first, and the crack breaks straight through the monolith, perpendicular to its surface (Figure 3.11a). The crack then proceeds into the composite and there is debonding between the monolith and composite layers close to the monolith crack site. Figure 3.11c shows the crack traversing the composite layer to its termination via the fracture of the outer EBC. There may also be a manufacturing flaw evident in this micrograph: the composite layer seems to be very thin compared to the composite layer bordering the region in Figure 3.11c. This type of flaw would result in a high susceptibility to fracture and allow the crack to more easily penetrate the total tube thickness. In Figures 3.11d through 3.11f, the crack continues to propagate laterally between the composite and EBC layers, thanks to composite/EBC debonding. Meanwhile, exposed fibers are also visible. Finally, the crack breaches the EBC for a second time. The reason for the second breach of the EBC initiated by a single crack in the monolith was probably a combination of the apparent manufacturing defect and the fact that there was substantial composite/EBC debonding which allowed the crack to propagate between the two layers without dissipating much energy. The composite layer is clearly the key component for dissipating fracture energy and arresting crack propagation.

Triplex sample 04-B (hoop tested in [47], SEM performed in this work) demonstrates the initiation of microcracks in the composite between the matrix and the fibers as well as monolith/composite debonding which leads to faster crack propagation (Figure 3.12). These types of fracture morphologies are evident in other Triplex samples and support the importance of the composite layer for controlling the fracture behavior of the Triplex tubes. Maintaining monolith/composite contact forces the cracks into the composite layer where they may dissipate through the composite via fiber/matrix debonding along the lengths of the fibers. As the contact between the matrix and fibers is broken, the fibers may now bridge the gap and bear the load.

Another feature of the hoop fracture in the Triplex tubes is the axial crack in the center of the tube illustrated in Figures 3.7 and 3.9. SEM of this axial crack shows fiber pullout from the composite matrix and rupture of the fibers at angles nearly perpendicular to their length. Figure 3.13 compares the axial crack morphology between Triplex samples 06-B, 04-A, and 04-B. The fibers in sample 06-B (Figure 3.13a) were pulled farther out of their matrix before they ultimately fractured. In contrast, the fibers in samples 04-A and 04-B did not pull out nearly as far. Samples 04-A and 04-B fractured at higher internal pressures and hoop stresses than sample 06-B. It may be that greater pseudo ductility in 06-B (easier fiber/matrix debonding) allowed the fibers to pull out further before rupture while simultaneously compromising the ultimate strength of the tube. Stronger bonding between the fibers and the matrix in samples 04-A and 04-B would reduce the fiber pullout while perhaps affording a higher hoop strength.

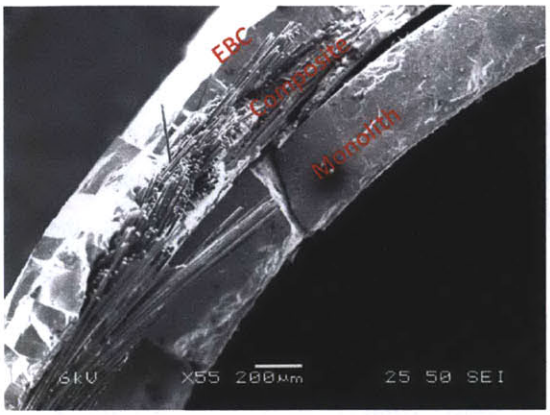

(a) 04-A initial monolith fracture and immediate propagation to composite.

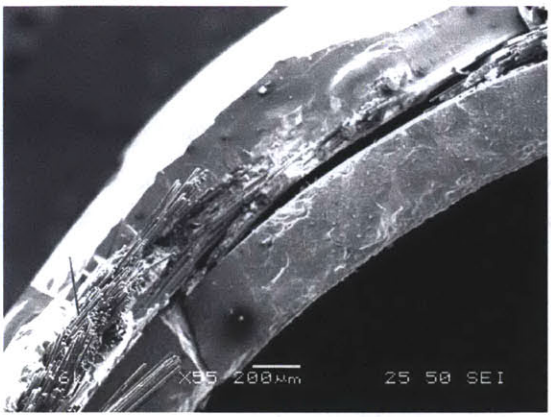

(b) 04-A propagation of crack laterally through the composite layers. Substantial composite/monolith debonding.

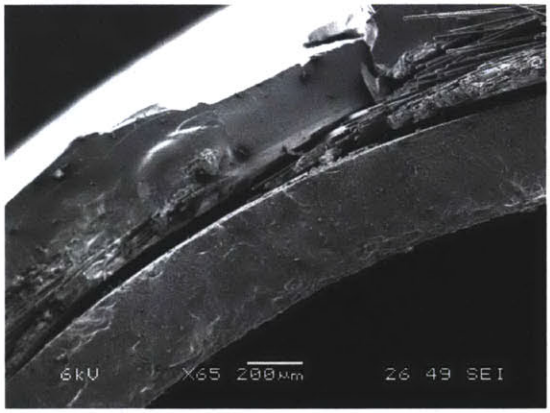

(c) 04-A: propagation of crack through the composite and rupturing the EBC.

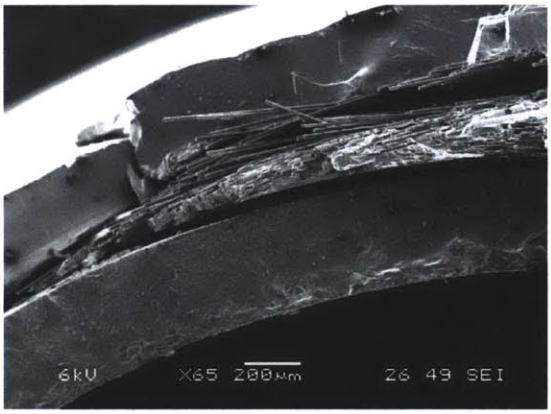

(d) 04-A continued lateral crack propagation.

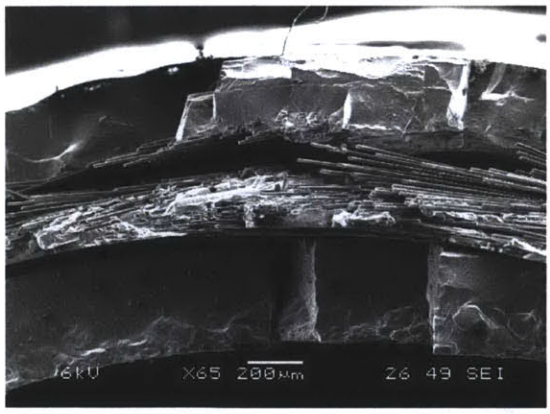

(e) 04-A lateral crack propagation and composite EBC debonding.

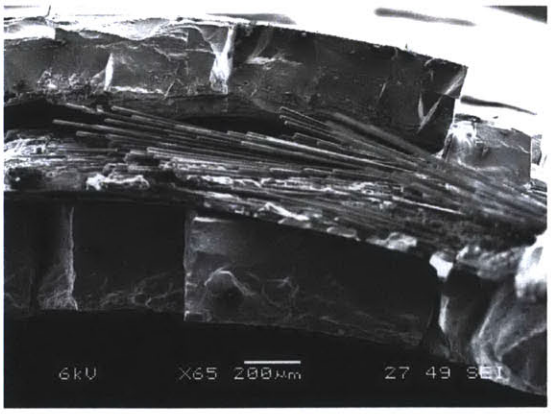

(f) 04-A crack propagation between the composite and EBC layers. Final EBC rupture.

Figure 3.11: SEM micrographs of Triplex sample 04-A after hoop test. Follow the crack propagation from left to right. SEM was done in this work. Hoop testing was done by Carpenter [47].

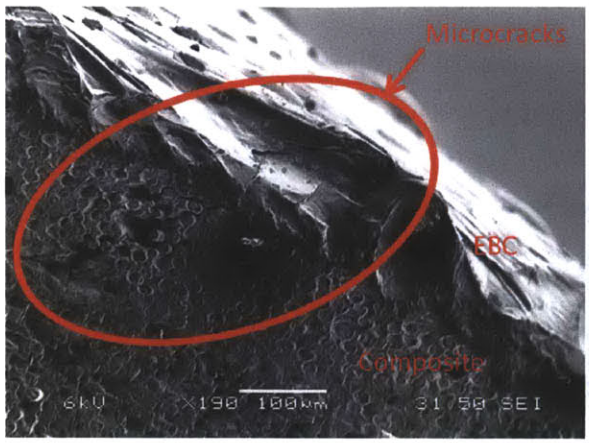

(a) Microcrack initiation in composite layer. Microcracks circled in red.

(b) De-bonding between monolith and composite.

Figure 3.12: Micrographs of Triplex sample 04-B.

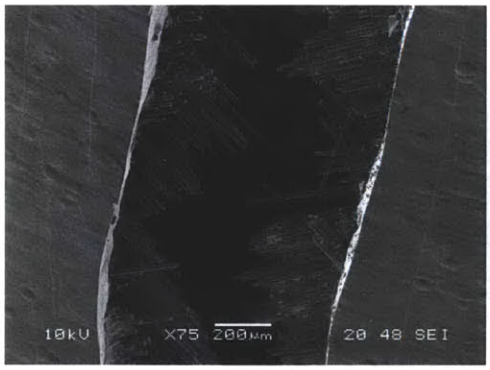

(a) Axial crack and fiber pullout in 06-B.

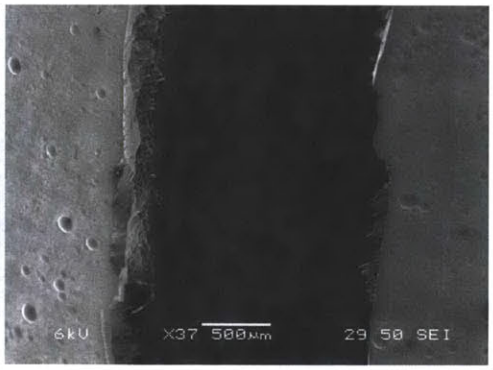

(b) Axial crack and fiber pullout in 04-A.

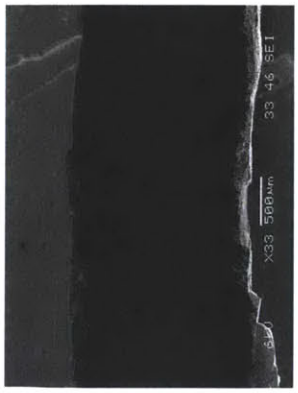

(c) Axial crack and fiber pullout in 04-B.

Figure 3.13: Axial cracking and fiber pullout.

4 Bonded-Block Specimen Irradiation and Analysis

Once the UO_2 fuel has been loaded into the fuel cladding, the top of the cladding must be plugged with an end cap. (Refer to Figure 2.5.) In the case of a Zircaloy cladding, the end cap is simply welded in place, but for a ceramic SiC cladding, a method to bond SiC to SiC will be required. The manufacturing methods discussed in Section 2.3.3 are not applicable to the problem of fitting an end cap because they are used to build a SiC structure sequentially from the inside out. The bonding method chosen would ideally provide the same strength, hermeticity, and resistance to degradation as the SiC cladding itself. Otherwise, the end cap becomes the weakest link in the ceramic cladding and might negate any operational or safety advances that were gained by switching to a SiC cladding system. In order to help identify suitable end cap solutions, three SiC/SiC bonding methods were tested in the ACI loop. These methods and the constructions of the bond specimens were discussed in greater detail in Section 2.3.2, but Table 4.1 provides a summary.

Table 4.1: Constructions and compositions of the six bond specimens tested.

Sample Number	Manufacturer	Block Composition	Bonding Method
1	PNNL	α-SiC Hexoloy SA	TiC/SiC tape with organic binder
2	Torino	α-SiC Hexoloy SA	calcium aluminate (CaO-Al_2O_3)
3	St. Gobain	α-SiC Hexoloy SA	10 μm Ti foil
4	PNNL	α-SiC Hexoloy SA	TiC/SiC tape with organic binder
5	Torino	α-SiC Hexoloy SA	calcium aluminate (CaO-Al_2O_3)
6	St. Gobain	α-SiC Hexoloy SA	10 μm Ti foil

4.1 Bond Specimen ACI Irradiation

The six bond specimens were photographed, weighed, and measured prior to their insertion into the ACI test loop. The six bond specimens were stacked in two columns of three within a single ACI sample module. Figure 4.1 shows one column of three bond specimens with a single specimen outlined in red. The sample module was then loaded into the designated irradiation position in the MITR-II as discussed in Section 2.4. The samples were only in-core for a short period of time just prior to a major planned outage of the MITR-II. The exposures and estimated dpa for each bond specimen are summarized in Table 4.2 .

Table 4.2: Total time the bond specimens were exposed to high temperatures and neutron fluxes. *EFPD = effective full power days

	Hours	Days	MWh	Fluence (n/m^2)	dpa
Neutron Flux Exposure	679	28.3 EFPD*	3260	1.59×10^{24}	0.159
High Temperature Exposure (T > 275 °C)	1071	44.6	-	-	-

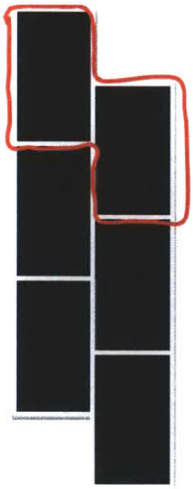

Figure 4.1: One column of three bond specimens. Single specimen outlined in red.

4.2 Bond Specimen PIE

After approximately 1.5 months, the ACI experiment was removed from the reactor core and the sample module was disassembled in a hot cell. It was found that five of the six specimens failed by complete debonding of the two halves of the bonded pair. The five failed specimens were removed for PIE and the surviving sample was later re-inserted into the ACI loop for further irradiation.

4.2.1 Bond Specimen Visual Analysis

Once the activity of the samples had decreased to a point where they were safe to handle, they were removed from the hot cell and photographed. Figure 4.2 shows before and after photographs of samples 2 and 5, both of which used the same bonding method—a calcium aluminate (CaO-Al_2O_3) glass pressed between two Hexoloy SA blocks. Both samples display the same coloring and texturing at the bond interface before and after irradiation. Before irradiation, there is a discoloring at the interface between the two bonded halves. This may be excess calcium aluminate or a component used in the processing. After irradiation, the two bonded faces of the samples (the two pictures at the bottom right in Figures 4.2a and 4.2b) have an irregularly shaped white spot which does not cover the entire face. This white spot is characteristic of the calcium aluminate bond material. SEM/EDX analysis of this feature is described in Section 4.2.2. There is also a line below which the bond face is a dark gray and above which the bond face is a lighter gray. The dark gray area corresponds to the area of the block which was bonded to the second block of the pair constituting the bond sample. The light gray area is the over-hanging, un-bonded or free portion of the face as shown in the "before" images on the left in Figures 4.2a and 4.2b. Recall from Section 2.3.2 that the bonded samples 2 and 5 were originally the same piece which was cut down the middle in order to separate sample 2 from sample 5 such that they should be mirror images of each other. The faces from the sectioning are not perfectly straight and their surfaces are not as smooth as the rest of the sample surfaces.

Before and after photographs of samples #3 and #6 are shown in Figure 4.3. Both samples 3 and 6 used a 10 μm

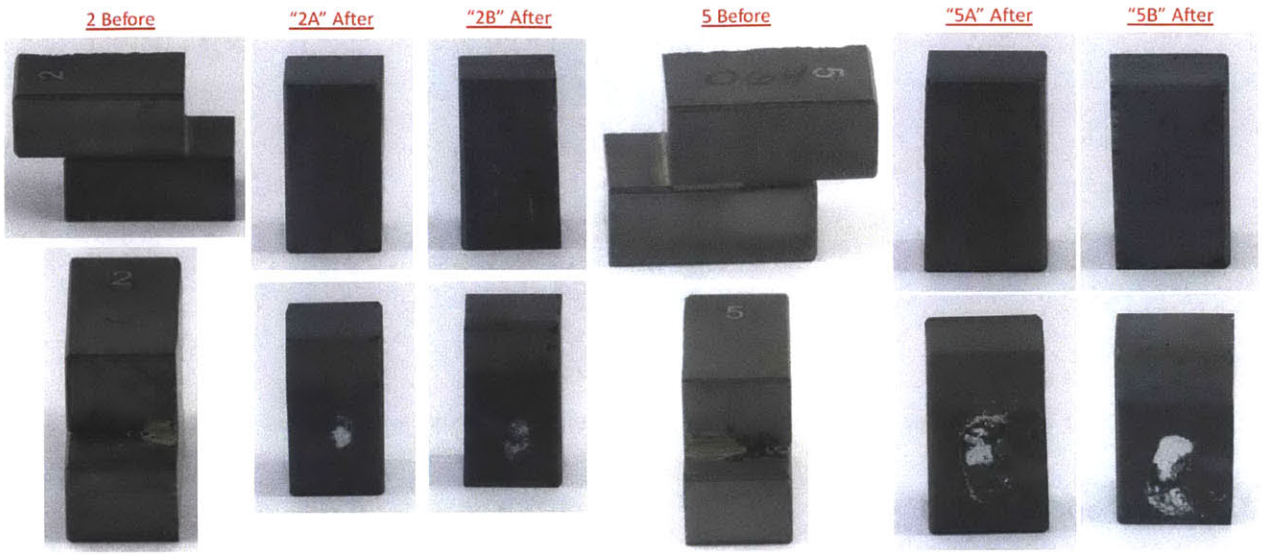

(a) Bond sample #2 before and after ACI irradiation.

(b) Bond sample #5 before and after ACI irradiation.

Figure 4.2: Bond samples #2 and #5 after ACI irradiation. Both 2 and 5 are the same construction: calcium aluminate bond method.

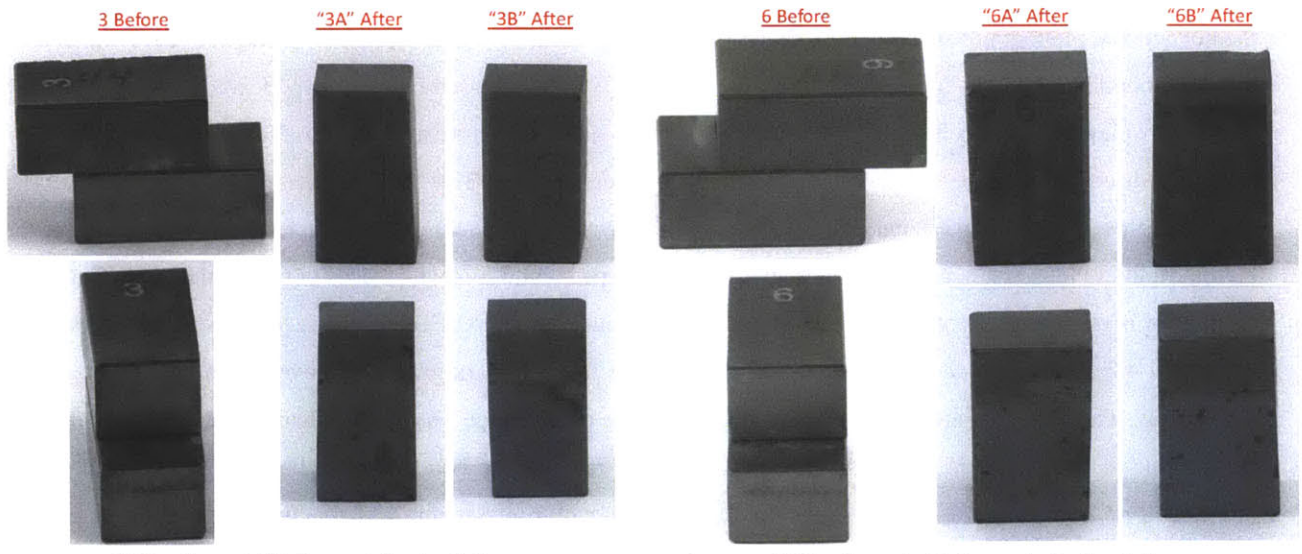

(a) Bond sample 3 before and after irradiation.

(b) Bond sample 6 before and after irradiation.

Figure 4.3: Bond samples 3 and 6 (same construction) before and after ACI irradiation.

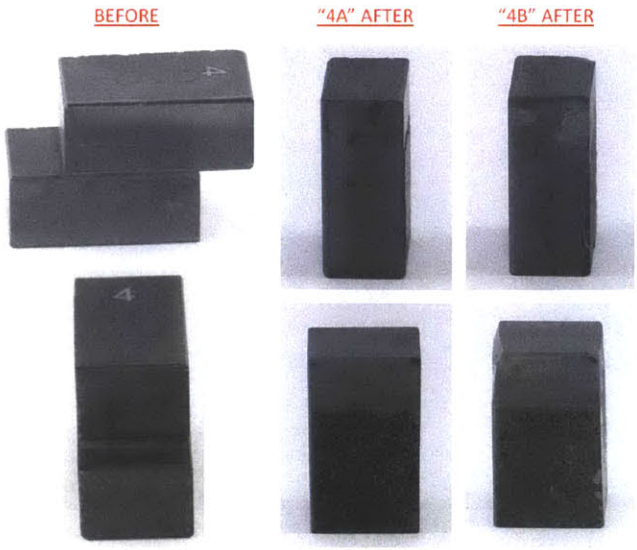

Figure 4.4: Bond sample 4 before and after ACI irradiation.

thick titanium foil to bond the two Hexoloy SA blocks together and were cut from the same parent bonded block. Both samples show some material overflow at the bond interface in the before images. In both samples, the after images of the bonded portion of the bonded face is a light gray with small dark spots. The un-bonded (free) portion of the bonded face is a darker gray. SEM and EDX analysis of the bonded and free areas of the bonded face are presented in Section 4.2.3.

Sample #1, whose twin is sample #4, survived the irradiation in the ACI loop which failed the bonds in the other 5 specimens. Thus, bond sample 1 was returned to the ACI loop for further testing, and only sample #4 is pictured in Figure 4.4. A number of characteristics are evident in these images. First, there is a small amount of material overflow in the bond seam of the sample prior to irradiation. (This feature was observed in all of the bond samples.) Second, the bonded area of the bonded face has a mottled appearance (images at the right in Figure 4.4) and even appears to have some elevation above the bare surface on the adjacent un-bonded surface which indicates that at least some of the original TiC/SiC tape remains. Third, the un-bonded area of the bonded face has a light gray color. Lastly, some of the edges of the sample after irradiation appear less straight than they did prior to irradiation.

4.2.2 Bond Specimen SEM/EDX Analysis — Bond Samples 2 and 5

After the initial visual analysis of the photographs in Section 4.2.1, SEM/EDX was used to characterize the bond surfaces at the microscale and to determine the elemental composition in the vicinity of the bonds. Both halves of each specimen were analyzed in this manner.

Figure 4.5 shows SEM micrographs of the border (or "bondline") between the bonded and un-bonded areas of the bonded face of sample "2A". As was seen in the photographs (Figure 4.2), the bonded side is a dark gray while the un-bonded side is a light gray. The 500x magnified image shows that the surface of the bonded side appears to have less porosity than the un-bonded side. It was postulated that this reduced porosity was due to residual calcium

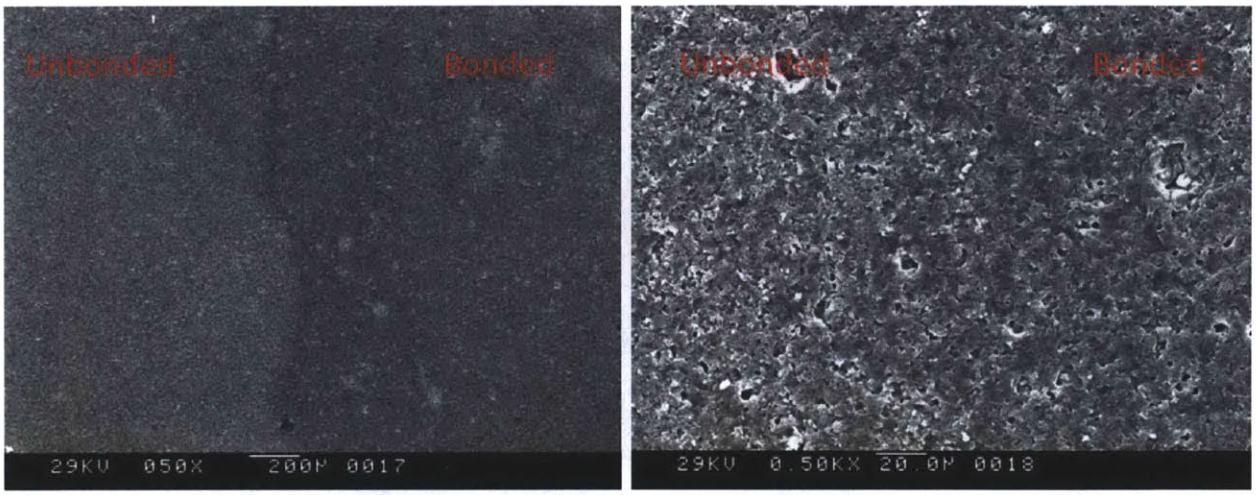

(a) 50x magnification of the bondline of sample "2A"

(b) 500x magnification of the bondline of sample "2A".

Figure 4.5: SEM (two different magnifications) of the borderline between the bonded and un-bonded areas of the bonded face of sample "2a".

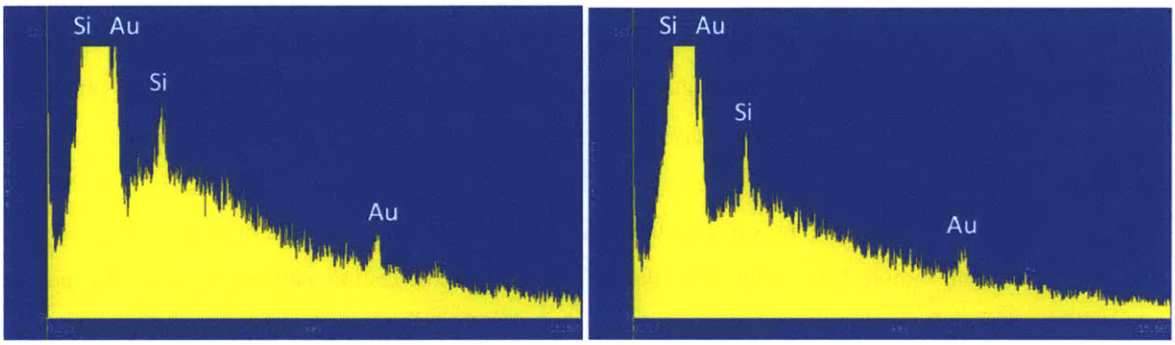

(a) Un-bonded region EDX spectrum of sample 2A.

(b) Bonded region EDX spectrum of sample 2A.

Figure 4.6: EDX spectra of the un-bonded and bonded regions of sample 2A. y-axis = the number of counts, x-axis = energy of X-rays emitted from the sample.

aluminate (glass-ceramic) bonding agent filling in some of the surface porosity. When EDX spectra of the bonded and un-bonded sides were compared, however, the spectra were identical (Figure 4.6). The samples had been coated in gold in order to make them more visible in the SEM, hence the "Au" label in Figure 4.6. Silicon conducts electricity well and has a large primary peak and a small secondary peak. The y-axis is the number of counts that the detector measured over the 5 minute counting period. The x-axis represents the energy of the characteristic x-rays emitted by elements present in the specimen upon excitation by the EDX source. Since the compositions on both sides of the bondline in Figure 4.5 appear to be the same, it could be that significant pressure had been applied when the two halves of sample 2 were bonded and that this pressure compacted the surface in the bonded region, reducing its surface porosity.

Next, the white spot evident in the conventional photographs was investigated in the SEM. Figure 4.7 shows the white spot on sample 2A at different levels of magnification. Following the red arrows, the magnification goes from a

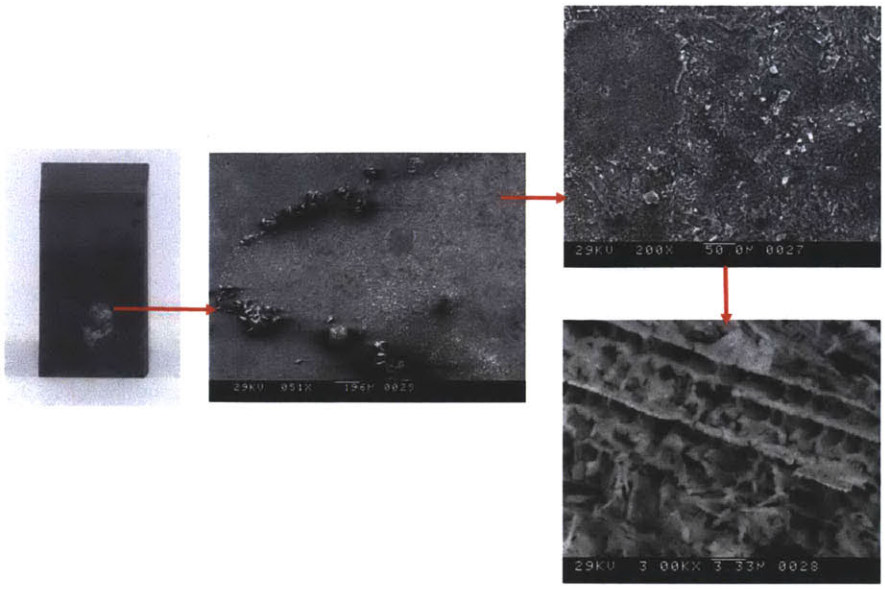

Figure 4.7: A series of magnifications of the white spot on sample 2A.

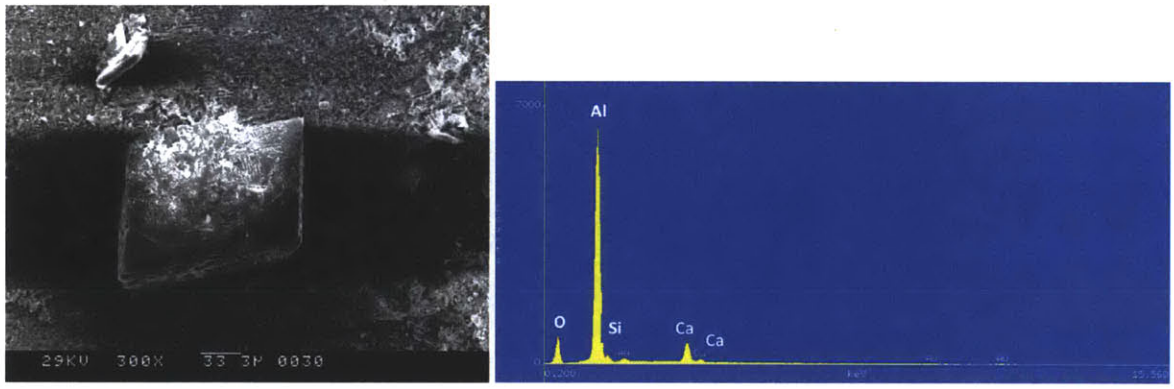

(a) Rhombohedral white spot crystal from 2A.

(b) EDX spectrum from the crystal identifies O, Al, Si, and Ca.

Figure 4.8: SEM and EDX of rhombohedral crystal from the white spot on sample 2A.

conventional camera, to 51x, to 200x, and finally, to 3000x. The 51x image shows a series of rhombohedral crystals arranged at the edges of the white spot. The 200x and 3000x magnifications show the highly porous and irregular surface of the white spot. The next figure shows a micrograph and an EDX spectrum of one of the rhombohedral crystals bordering the white spot. The EDX spectrum shows large peaks for oxygen, silicon, aluminum, and calcium. This is clear evidence that the crystals surrounding the white spot are, in fact, remnants of the calcium aluminate ($CaO\text{-}Al_2O_3$) bond material. An EDX spectrum (Figure 4.9) of the white region surrounding the crystal reveals the presence of the same elements: O, Al, Si, and Ca. Additionally, it appears that there is some iron impurity present which may have deposited as corrosion products from the ACI loop.[15]

SEM/EDX images and spectra from sample 5 are very similar to the types of images and spectra obtained from sample 2. This consistency was expected given that samples 2 and 5 have the same construction. Figure 4.10 shows the

[15] Iron oxide spears have been observed in the ACI loop in the past.

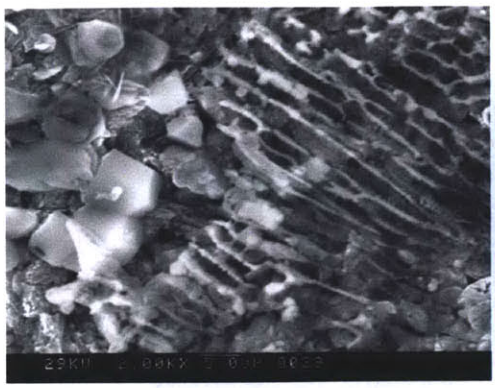

(a) 2000x view of the white spot near the calcium aluminate crystal from Figure 4.8.

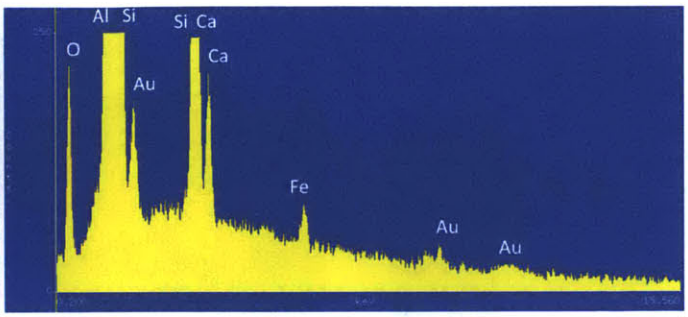

(b) EDX spectrum of region in Figure 4.9a.

Figure 4.9: SEM and EDX of area surrounding the crystal from Figure 4.8a; Fe, Ca, O, Al, and Si are present.

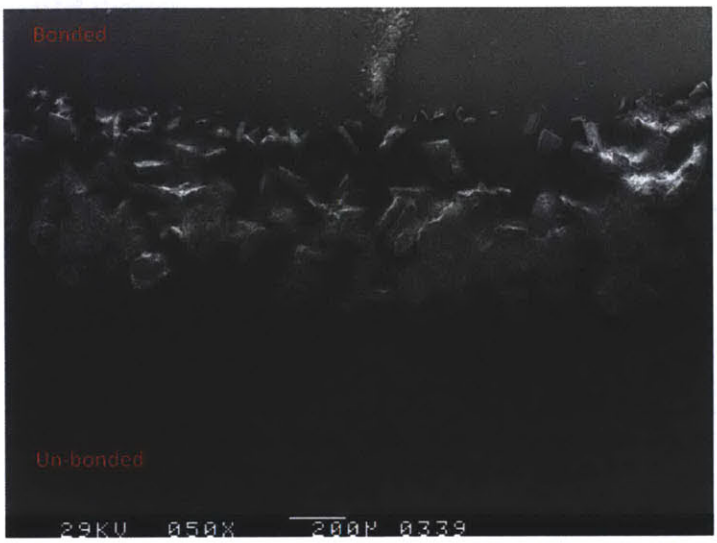

Figure 4.10: Rhombohedral calcium aluminate crystals on the between the bonded and un-bonded regions of sample 5A.

bondline between the bonded and un-bonded areas of sample 5A. Again, the white spot in sample 5A was surrounded by the rhombohedral type crystals which seemed more prevalent in sample 5A than in sample 2A. Figure 4.11 shows more images of the crystals in sample 5A, including several crystals which were located farther away from the white spot, yet still in the bonded region. No crystals have been observed in the un-bonded regions. A 2D elemental map confirming the crystals as calcium aluminates, shown in Figure 4.12, was generated from EDX data of the single crystal pictured at the bottom right in Figure 4.11. The white dots indicate counts for the elements listed above in red. The crystal is rich in Ca, Al, and O, and is devoid of Si.

The majority of the white-colored spot in observed in samples 2 and 5 (pictured in Figures 4.2, 4.7, and 4.9) does not seem to have any particular order. It appears that the calcium aluminate may be amorphous in this region which would make sense since calcium aluminate is a type of glass-ceramic. The crystals represent well-ordered calcium aluminate, the presence of which is more difficult to explain. As was discussed in Section 3.3.3, amorphous SiC fibers

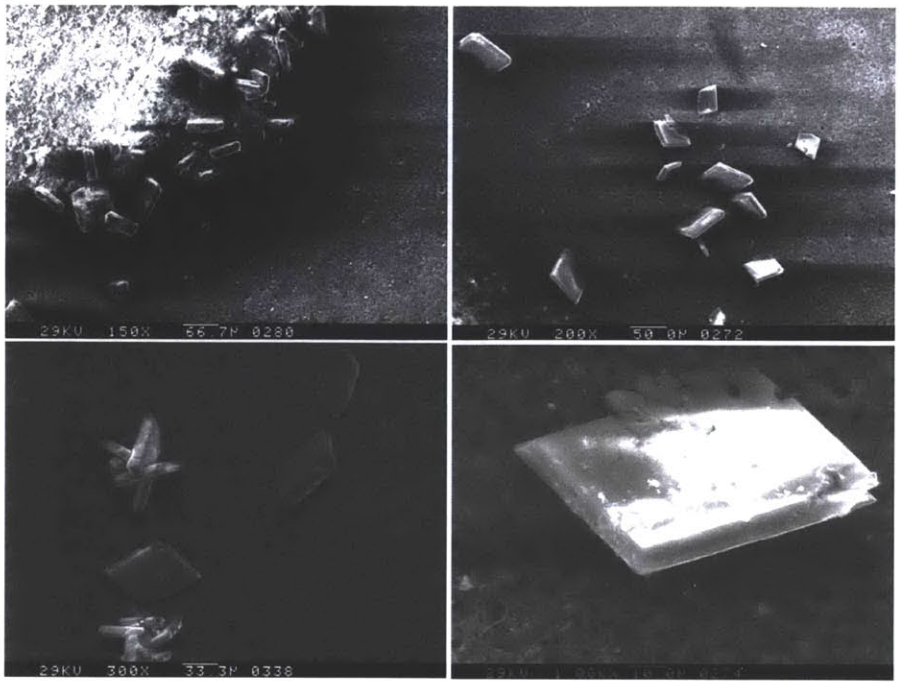

Figure 4.11: SEM from sample 5A. Top Left: calcium aluminate crystals bordering the white spot region. Top right and bottom left: Groups of crystals. Bottom Right: a single crystal.

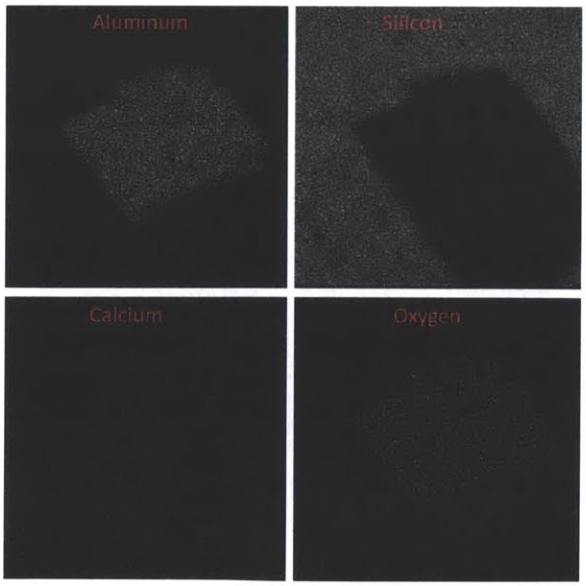

Figure 4.12: 2D elemental map of a lone calcium aluminate crystal. White spots indicate the presence of the element highlighted in red.

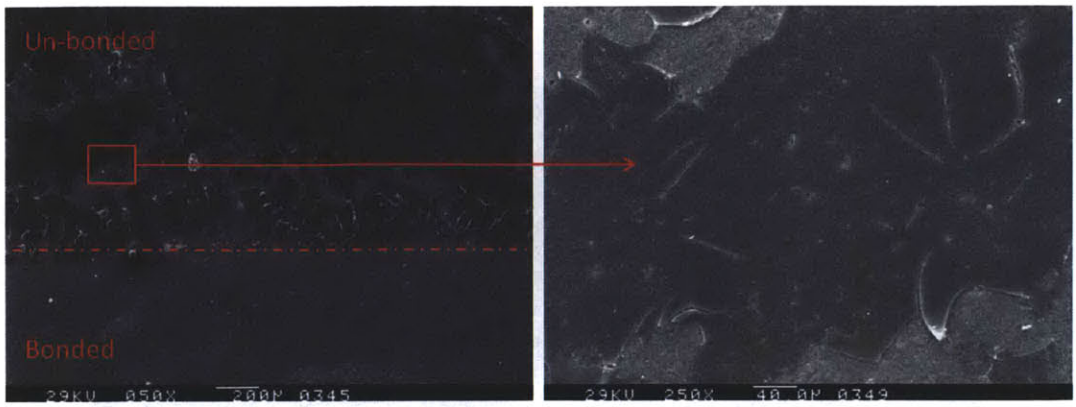

Figure 4.13: Micrographs of the bondline region of sample 6A.

may densify, gain long-range order, and crystallize during irradiation. The same effect is seen in vitreous silica. [55] It is possible that neutron irradiation in the ACI loop has conferred ordering and crystallization to the fringes of the calcium aluminate bond material. Another explanation for the presence of some calcium aluminate crystals bordering a sea of amorphous calcium aluminate is that the CaO-Al_2O_3 was not cooled rapidly enough when it was processed onto the samples. In order to produce the glass-phase calcium aluminate, it must be cooled rapidly in order to prevent crystallization. [71] If additional crystallization had occurred either due to irradiation or manufacturing variations, the mechanical properties of the bond between the two Hexoloy SA blocks would be weakened because crystalline aluminosilicates have inferior mechanical properties when compared to their amorphous (glass-like) counterparts. [72]

4.2.3 Bond Specimen SEM/EDX Analysis — Bond Samples 3 and 6

As in the previous section, SEM/EDX will be used to compare samples 3 and 6 which both were bonded by a 10 μm thick titanium foil pressed between the two Hexoloy SA blocks with 30 MPa of pressure. Figure 4.13 shows the bondline region of sample 6A in both 50x and 250x magnification. The dark region at the top of the micrograph represents overflow of some material from the bonded region during the manufacturing process. The micrograph to the right in Figure 4.13 shows a 250x view of the region bounded by a red box in the figure at the left. The bondline region of sample 3A looks very similar to the bondline region of sample 6A. EDX spectra were taken for this bond overflow material in both samples 3A and 6A, and are displayed in Figure 4.14. The overflow regions depicted on both micrographs look similar in that they are darker than the underlying pure SiC substrate and that they have a crackled appearance. The 1000x magnification used for the micrograph of sample 3A (Figure 4.14a) shows small bright spots. The corresponding EDX spectrum on the left in Figure 4.14a shows the presence of small amounts of titanium and iron, in addition to the usual Si. This is the first evidence of the Ti foil. A few similar bright spots are visible on the micrograph for sample 6A. Due to the scale on the EDX in Figure 4.14b, if any Ti or Fe peaks exist, they are not visible.[16]

SEM micrographs and an EDX spectrum from within the bonded regions of samples 3 and 6 confirm the presence

[16] Since only an image of the EDX file was saved, the spectrum cannot be re-made with a different scale.

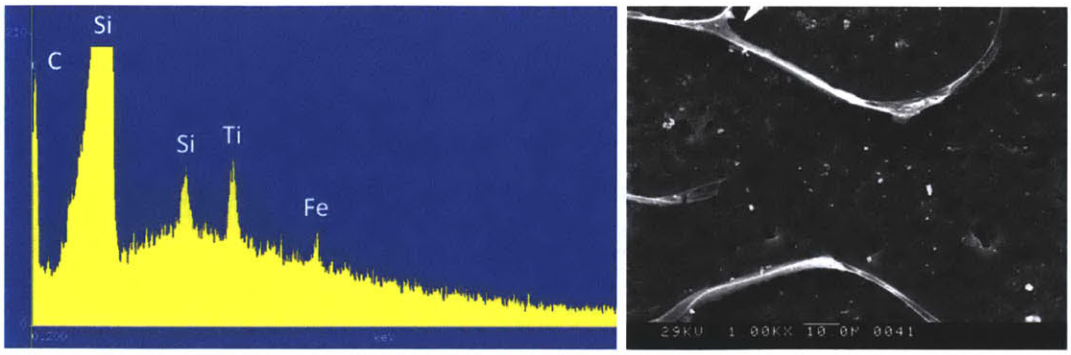

(a) EDX of bond overflow in sample 3A.

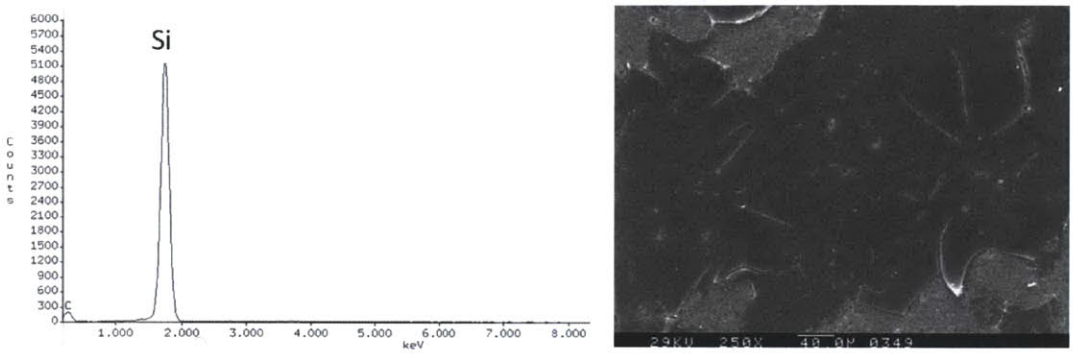

(b) EDX and SEM of bond overflow in sample 6A.

Figure 4.14: Comparison of the micrographs and EDX spectra from samples 3A and 6A.

of a titanium bond agent along with two other metals. First, consider Figures 4.15a and 4.15b which show crystal fields and a branched pattern evident in micrographs from both samples 3 and 6. When the SEM is trained on a grouping of the bright crystals (left in Figure 4.15c) and an EDX spectrum is obtained (right in Figure 4.15c), there are peaks for Ti, Fe, Ni, and Si. It is believed that these bright crystals are iron and nickel oxides deposited as corrosion products from the ACI loop and that they are not components of the bonding material. These oxides may have been deposited after the bond had failed. Similar bright oxide crystals have been observed in SEM micrographs on other, unrelated samples.

If the large, bright crystals are metal oxides unrelated to the bond material, then where is the titanium bond material localized? Below, in Figure 4.16a, a micrograph and a 2D element map were obtained for a 2000x magnified view of the branched pattern first shown above at 200x magnification in Figure 4.15b. These images indicate that titanium is present only in the branches and not in the darker regions between branches which are silicon carbide. Close inspection of the 2D maps show that titanium is localized in the branches where there is simultaneously a decrease in the counts of silicon. At high magnifications, the branches themselves were found to contain very small, bright crystals, which EDX confirmed were rich in titanium and carbon with traces of oxygen and iron. The two micrographs at magnifications of 2500x and 10000x in Figure 4.17a show the small bright crystals in question. An EDX spectrum taken from one of the crystals is also pictured. When a second EDX spectrum was taken in the dark region surrounding the small crystals, a spectrum characteristic of pure SiC was obtained (Figure 4.18) with perhaps slight traces of Fe and O. In what is

(a) Crystal field 100x magnification.

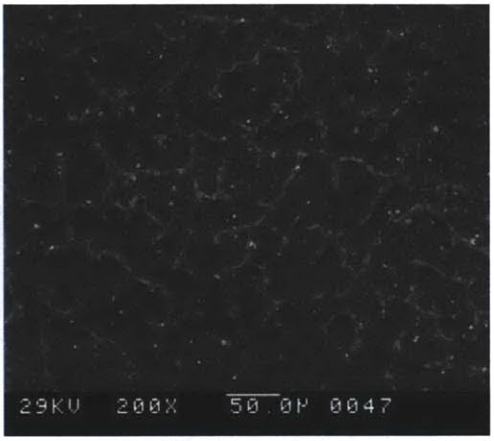

(b) Crystal field with branched pattern at 200x magnification.

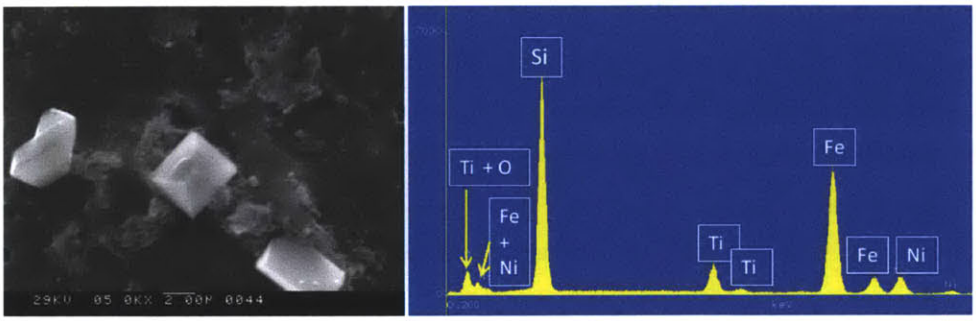

(c) Individual crystals from the crystal field at 5000x magnification with EDX spectrum.

Figure 4.15: Micrographs from the bonded region of sample 3A containing crystals.

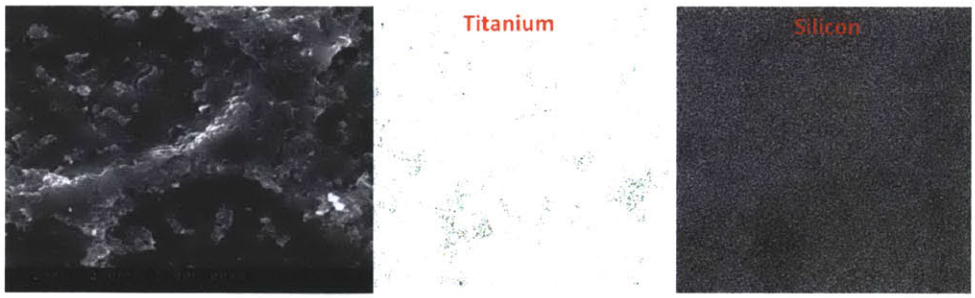

(a) SEM micrograph and 2D EDX map of the branched region shown at left. Dots on the white background are counts of titanium. White dots on the black background are Si counts.

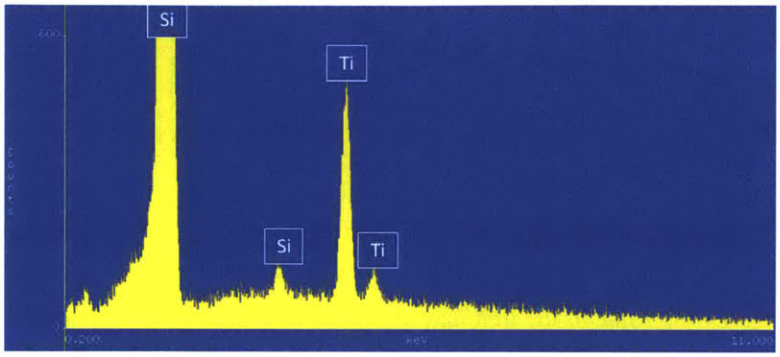

(b) EDX spectrum showing titanium and silicon peaks.

Figure 4.16: Micrographs and EDX spectra showing the location of titanium in the branches in the bonded regions of sample 3A. The same is seen in sample 6A.

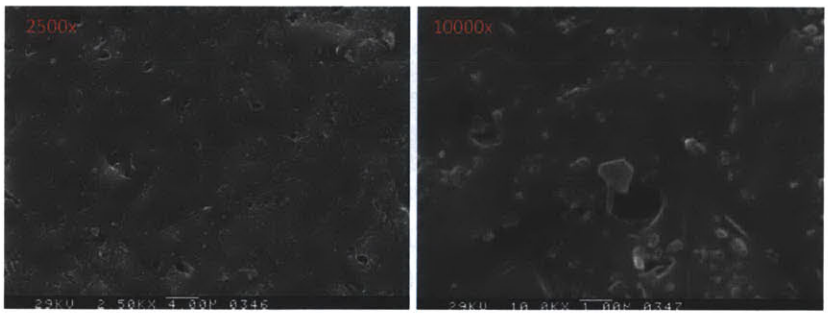

(a) Nano-scale titanium crystals in the branches of the bonded region in sample 6A.

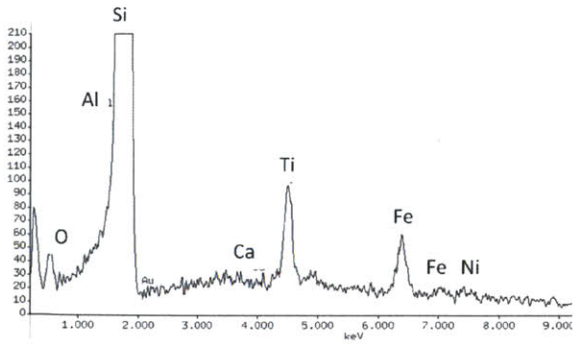

(b) EDX spectrum of the large crystal pictured in the center of the right-most image in Figure 4.17a.

Figure 4.17: Nano-sized titanium crystals in the bonded region of sample 6A.

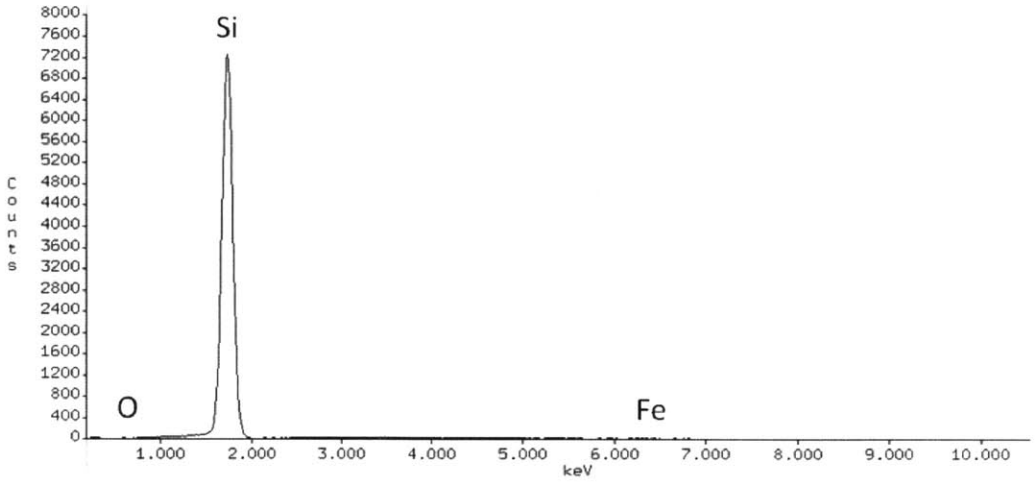

Figure 4.18: EDX spectrum of dark region surrounding the bright crystals picture in Figure 4.17a.

considered "commercially pure" titanium, iron may exist with a maximum concentration of 0.25 w/o, and oxygen may be present to a maximum of 0.4 w/o. [73] These common trace impurities in titanium may account for their presence in the spectrum in Figure 4.17b. Some of the iron may also have been deposited as corrosion products from the ACI loop.

What the micrographs and EDX spectra presented above are indicating is that the titanium is localized primarily within crystals in branch-like patterns in the bonded regions of samples 3 and 6. If the 10 μm Ti foil had remained intact, in its as-fabricated form, one would expect to see much more Ti. This is not the case, and may be evidence that not only did the foil fail and the two Hexoloy SA blocks separated, but that the foil itself was then degraded and removed from the exposed bond faces. The seemingly low concentrations of titanium in this branch-like pattern may also be evidence that the foil did not adhere uniformly to the surfaces of the two blocks. If this is the case, then it may be one reason for the ultimate failure of the bond. Very little was revealed by the manufacturer about the bonding method used in these samples which makes it difficult to conjecture about the possible failure modes, but one possibility is that the thermal expansion coefficients of SiC and titanium are very different. From room temperature to 700 °C, Hexoloy SA is quoted with a coefficient of thermal expansion of $4.02 \text{x} 10^{-6}$ mm/mm K. [74] Commercial grade titanium, on the other hand, has a coefficient of thermal expansion of $9.9 \text{x} 10^{-6}$ mm/mm K, more than twice that of the Hexoloy SA. [73] Differential thermal expansion may have generated shear stresses on the bond, which may have contributed to its failure in both samples 3 and 6.

4.2.4 Bond Specimen SEM/EDX Analysis — Bond Sample 4

Samples #1 and #4 were bonded using a TiC/SiC "tape" with an organic binder. Sample #1 survived the initial 1.5 months in the ACI loop, while sample #4 did not. The following SEM/EDX images will be used to help describe the nature of the bonding and to help explain possible reasons for the bond's failure in sample 4. First, consider the micrographs taken at the boundary between the bonded and un-bonded areas of the bonded faces. Figure 4.19 shows the bondline on samples "4A" and "4B", the two blocks which were originally bonded together as sample 4, but which

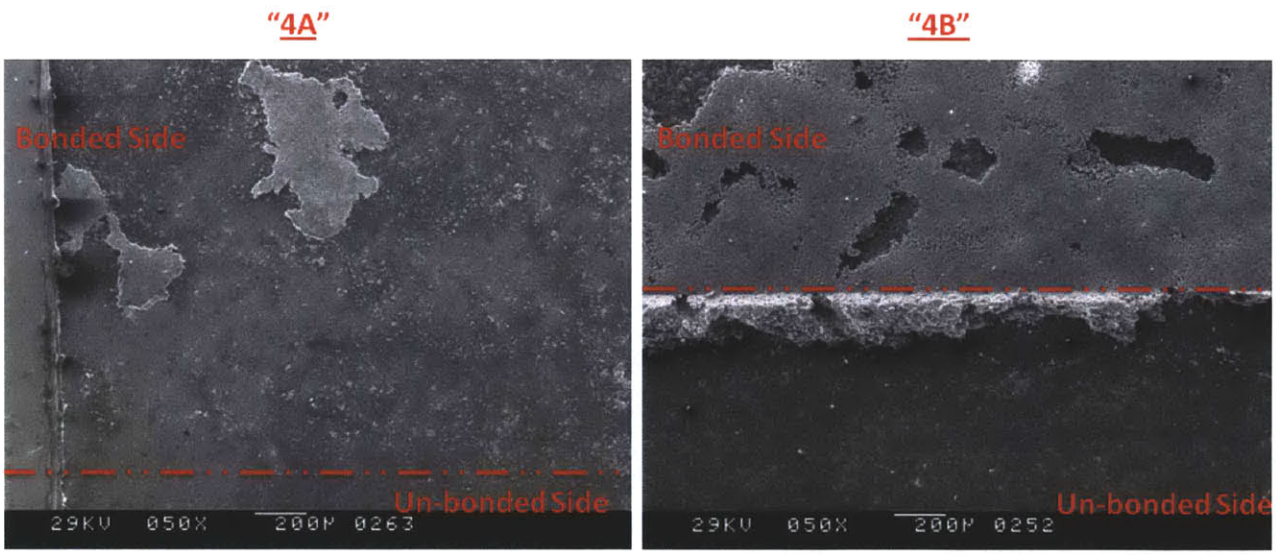

Figure 4.19: Micrographs of the bondline between the bonded and un-bonded sides for samples 4A and 4B (the two halves of sample 4).

are now separated. The bonded side of the samples is above the red dashed line and the un-bonded side is below the dashed line. In the micrograph for sample 4B, the light colored flat region pockmarked with dark holes is the bond material (TiC/SiC tape + organic binder). Notice that some of the bond material was not pressed between the two blocks and extends into the un-bonded side of the dashed line. This excess material is not as flat as the material on the bond side of the dashed line. In contrast, the micrograph for sample 4A shows mostly a flat SiC base material with occasional lumps of bond material. Figure 4.20 shows two more micrographs comparing the complementary bonded regions of sample 4A and 4B. It appears that the bond material missing from side 4B remains adhered to side 4A and the two may fit together like two puzzle pieces. It is not known why more bond material would remain on the 4B half than on the 4A half.

EDX spectra were obtained for both the bond material and the base SiC material. Figure 4.21a shows the spectrum for the un-bonded region of sample 4A. This spectrum is consistent with the EDX spectra obtained from the un-bonded regions of every bond sample investigated in this work. Only silicon and carbon were detected. By contrast, an EDX spectrum (Figure 4.21b) from the bond material on the bonded side of sample 4A shows strong peaks for silicon and titanium with smaller peaks for iron and a trace of aluminum. This spectrum for the bond material confirms the titanium bond material, but the presence of the iron and especially the aluminum was somewhat surprising.

Taking a closer look at the bond material reveals that it is quite porous and that it is certainly the thickest remaining deposit of the three bond methods observed in this work. In the other two methods, after failure, the bond material appears to be little more than a thin film, unevenly distributed over the surface of the SiC substrate. The fact that such a thick deposit of the TiC/SiC tape remains on samples 4A and 4B suggests that the bond material itself has reasonable resistance to the ACI loop environment. Figure 4.22 shows a piece of the bond material in increasing magnifications from 50x to 500x to 5000x. The red box in the top left of Figure 4.22 highlights a bright spot within the bond material. The next image, in the top right of Figure 4.22, centers on this bright spot at 500x magnification. The bright spot is

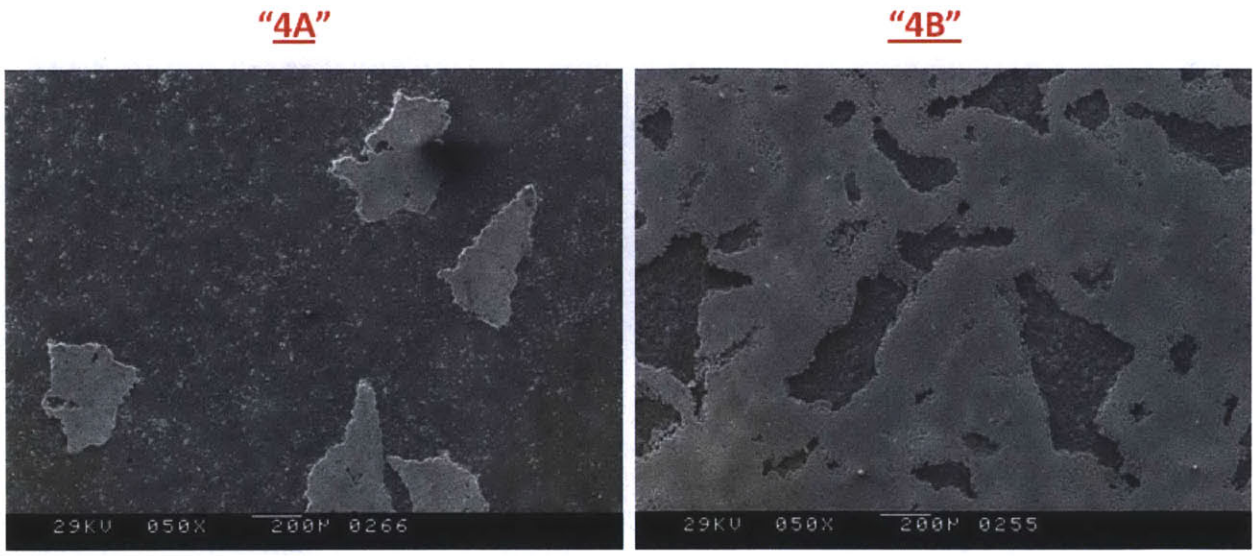

Figure 4.20: Complementary bonded regions of sides 4A and 4B.

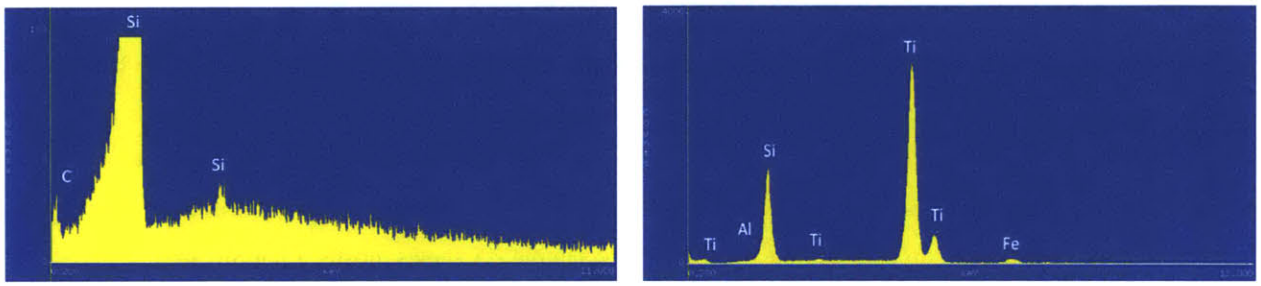

(a) EDX spectrum of un-bonded region of sample 4A. Showing C and Si.

(b) EDX spectrum of the bond material in the bonded region of sample 4A. Showing Ti, Al, Si, and Fe.

Figure 4.21: EDX spectra for sample 4A.

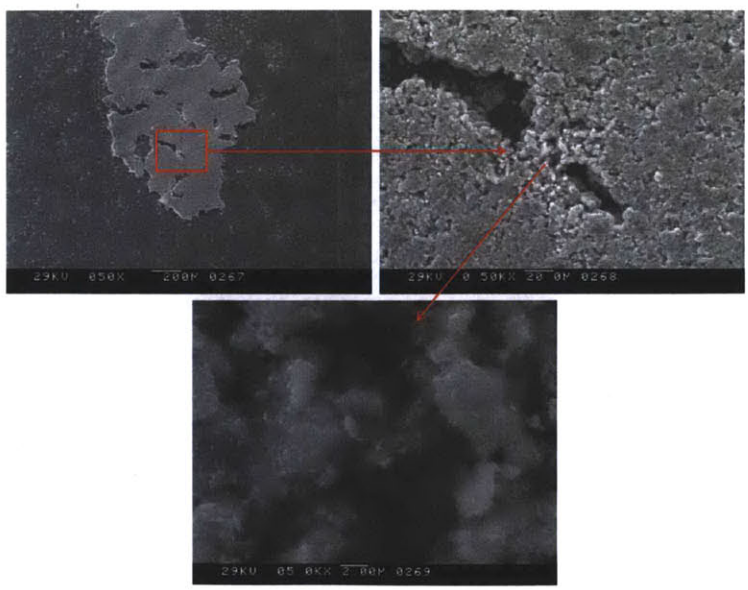

Figure 4.22: Micrographs of the bond material from sample 4A showing bright spots with a needle-like structure.

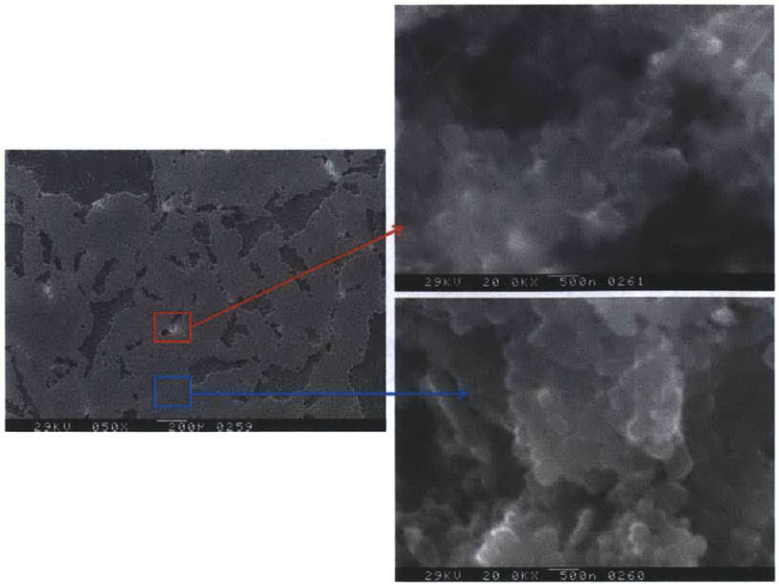

Figure 4.23: Bright spots on sample 4B contain needles. Away from the bright spots, no needles are found. The micrograph at left is magnified at 50x, and the micrographs at right are magnified at 20000x.

shown again at 5000x magnification in the bottom center micrograph in Figure 4.22. A needle-like crystal morphology was discovered in this third micrograph.

The same bright spots were also seen on sample 4B as can be seen in the left image in Figure 4.23. The left-most image shows the pockmarked surface of the bond material with a number of bright spots dotted across the surface. One such bright spot is boxed in red and magnified to show the needle-like crystals in the top right image of Figure 4.23. Please note the scale and the magnification of the top right micrograph displaying the needles: 20000x magnification and the scale is listed as 500 nm. These needles are very small. The blue box and blue arrow in Figure 4.23 show that in the bond material away from the bright spots, no needles are visible. This proves that the small needle-like crystals are localized at the bright spots which are unevenly distributed across the bond material. After determining that the bright needles are localized in particular regions of the bond material, EDX was used to help determine the elemental identity of the needles. The EDX spectrum at the right in Figure 4.24 shows that the needles are comprised of aluminum and that the substrate that the crystals are located on is the titanium-based tape.

Based on the micrographs in Figures 4.22 and 4.23, it would appear that these bright spots and their crystals are only found in regions of the bond material which have dark holes of missing bond material. No bright spots were observed in a solid mass of "un-damaged" bond material. This leads to speculation about the reason/purpose for the existence of these needles. If the needles existed at their present positions at the time of fabrication, then they may have had an effect on the de-bonding of sample 4, since they are only present at the sites where bond material from one half of the sample has been pulled off by the other half of the sample. On the other hand, if the needles were not present at the time of fabrication, it is possible that they deposited as corrosion products from the ACI loop. If this were the case, it is difficult to explain why they only appear in some of the sites where some of the bond material is missing and not at all of the sites where bond material is missing. These needles are comprised of aluminum, and no

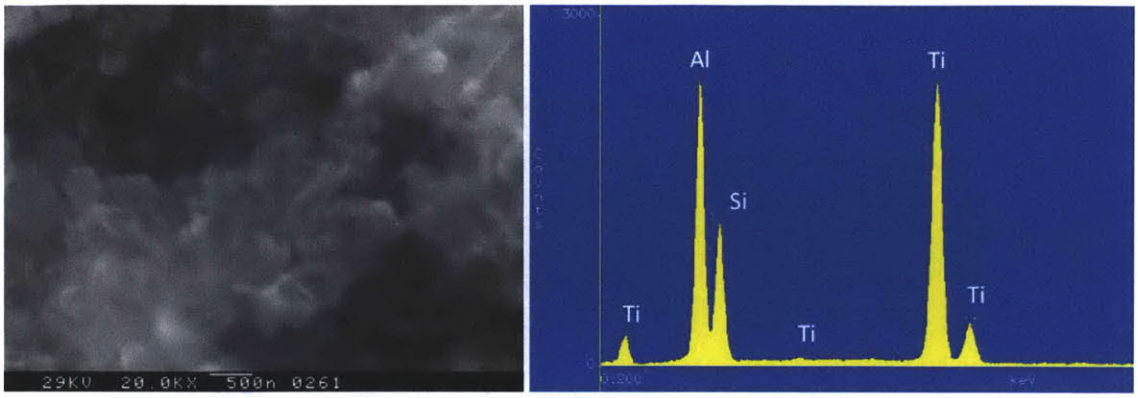

Figure 4.24: Left: SEM of needles from 4B bond material. Right: EDX spectrum of the needles: Ti, Al, and Si are present.

Table 4.3: Summary of weight loss in the failed bond specimens.

Bond Sample #	Pre-Irradiation Mass	Post-Irradiation Mass	% Mass change ($\frac{Final-Initial}{Initial}$ 100)	Absolute Mass Change (g)
2	15.65982	15.60996	-0.31846	0.04987 ±0.00012
3	15.41152	15.40952	-0.01301	0.00200 ±0.00012
4	16.73282	16.70407	-0.17185	0.02876 ±0.00011
5	16.95425	16.90109	-0.31353	0.05316 ±0.00014
6	17.23185	17.22304	-0.05114	0.00881 ±0.00012

aluminum was found in any of the other four bond samples. This would seem to rule out the possibility that these needles are due to corrosion products. Aluminum is not listed as an impurity in quoted data for commercially pure titanium, but it is possible that aluminum impurities were present at the time of manufacture. For commercially pure grades of aluminum (depending on the tempering) the tensile strength and yield strength may range from 90 MPa to 165 MPa and 34 MPa to 154 MPa respectively. [75] Commercial titanium is significantly stronger with a tensile strength of 448 MPa and a yield strength of 379 MPa. [73] Although the strength of the Al needles is likely different from that measured for a macroscopic Al sample, it is possible that localized deposits of aluminum acted as sites for crack initiation and de-bonding.

4.2.5 Bond Specimen Weight Change Analysis

The bond samples were each weighed before and after irradiation and minor weight loss is reported for all samples following ACI irradiation. First, notice that the weight loss measured for each sample is very small. Second, notice that sample numbers 2 and 5, and sample numbers 3 and 6, exhibited very similar % mass changes. This makes sense given that samples 2 and 5 each used the same bond method (calcium aluminate glass-ceramic), and samples 3 and 6 each used the same bond method (10 μm titanium foil). Sample #4 was the only one of the samples bonded with TiC/SiC tape to fail and cannot be compared to its twin, sample #1. The weight loss appears to be related directly to the bonding method employed, and also indicates that the α-SiC Hexoloy blocks are chemically stable in the ACI

loop. The bond material may have been lost from the SiC substrate as a result of corrosion or erosion in the loop. A significant limitation of the ACI experiment is that it, presently, does not allow a means for determining exactly how long the bonds remained intact in the loop. The bonds failed within the ~1.5 month duration of testing, however, the time at which failure occurred during that period is unknown.

4.2.6 Bond Specimen Dimensional Change

The bond specimens were measured before and after irradiation. The dimensions of the specimens *prior* to irradiation are listed in Table 4.4. Table 4.5 presents the *post*-irradiation dimensions of the failed bond specimens, and the labeled

Table 4.4: Pre-irradiation dimensions of the bond specimens. Pairs of samples with the same bonding method are color coded. Bonding methods were summarized in Table 4.1. The figure at right describes the dimension labels.

	a (mm)	b	c	d	e	f	g	h	i
1	22.32	22.34	28.69	18.92	12.16	12.24	12.31	9.42	9.42
2	22.33	22.37	28.76	18.98	11.85	12.00	12.00	9.41	9.42
3	22.36	22.36	28.84	18.88	11.88	11.45	11.78	9.42	9.42
4	22.32	22.32	28.69	18.93	12.85	12.70	12.90	9.42	9.42
5	22.25	22.36	28.70	19.01	12.89	12.99	12.99	9.42	9.41
6	22.36	22.36	28.84	18.88	13.12	13.11	13.14	9.42	9.42

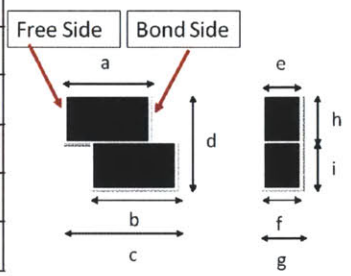

dimensions are explained by the adjacent figure. The "free side" is the side of the Hexoloy SA block which was overhanging and never bound to the other block. The "bond side" of the block is that which was initially bonded to the other block. Table 4.6 displays the % relative error in the post-irradiation dimensional measurements from Table 4.5. The absolute dimensional change between the pre-irradiation dimensions and the post-irradiation dimensions are listed in Table 4.7. The differences between the pre-irradiated dimensions and the post-irradiated dimensions in Table 4.7, should be considered cautiously as the pre-irradiation measurements were made by a different experimenter using a different set of measurement calipers. Additionally, the widths along a certain edge were not uniform, i.e. the sample might be wider at one end than at the other end. In order to account for this, a series of measurements were taken at different points along a given direction, and the results were then averaged. These average results were then compared to the pre-irradiation dimensions by subtracting the initial (pre-irradiation) dimensions from the final (post irradiation) dimensions. Despite knowing the absolute pre and post-irradiation dimensions with a precision of 0.1 - 0.3 % (as shown in Table 4.6), the calculated differences in Table 4.7 are so small that, in some cases, the error is larger than the calculated differences. Thus, the hand measurements made with digital calipers can not always provide data accurate enough for a sound statistical comparison. In the literature, linear variable differential transformers (LVDT) with an accuracy of 3 μm or optical gauges with an accuracy of 2.5 μm have been used to measure small dimensional changes. [76, 55] The use of an LVDT or an optical gauge would have improved the accuracy of the measurements.

The measured differences for which the error is smaller than the differences themselves will now be discussed. In most cases, the length (dimensions "a" and "b") of the Hexoloy SA blocks increased slightly, but in several cases,

Table 4.5: Dimensions of the bond samples after irradiation to 0.16 dpa. Colors correspond to blocks A or B from the same numbered sample. The small figure at right describes the dimensions. The error for each measurement is listed in Table 4.6.

	Length (mm)		Width (mm)		Height (mm)	
	a free	a bond	e free	e bond	h free	h bond
2A	22.448	22.410	11.952	11.717	9.518	9.415
3A	22.453	22.430	11.425	11.962	9.418	9.407
4A	22.338	22.367	12.957	12.473	9.448	9.442
5A	22.410	22.427	12.803	13.103	9.423	9.392
6A	22.437	22.413	13.410	12.768	9.448	9.423

	b free	b bond	f free	f bond	i free	i bond
2B	22.407	22.350	11.787	12.105	9.430	9.430
3B	22.338	22.393	11.863	11.517	9.407	9.417
4B	22.373	22.393	12.650	12.875	9.402	9.400
5B	22.363	22.257	13.000	12.655	9.412	9.423
6B	22.420	22.413	12.905	13.255	9.420	9.418

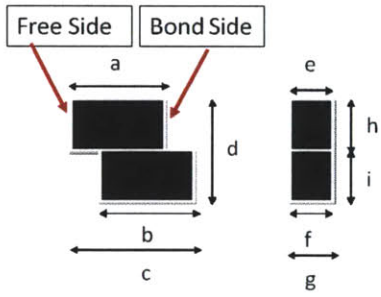

Table 4.6: % relative error in the measurements listed in Table 4.5.

	a free	a bond	e free	e bond	h free	h bond
2A	0.086 %	0.045 %	0.221 %	0.508 %	1.093 %	0.199 %
3A	0.111	0.134	0.452	0.414	0.124	0.129
4A	0.060	0.113	0.490	0.662	0.381	0.271
5A	0.138	0.093	0.365	0.284	0.347	0.105
6A	0.168	0.093	0.236	0.359	0.337	0.160
	b free	b bond	f free	f bond	I free	I bond
2B	0.125	0.155	0.301	0.424	0.100	0.274
3B	0.089	0.026	0.368	0.278	0.087	0.173
4B	0.097	0.068	2.293	0.383	0.183	0.190
5B	0.154	0.069	0.377	0.211	0.296	0.239
6B	0.144	0.136	0.127	0.156	0.212	0.124

Table 4.7: Comparison of pre-irradiation and post irradiation dimensions between the as-fabricated specimens and the as-irradiated specimens. All values have units of mm. Columns marked "Δx (post - pre)" are the differences when the pre-irradiation dimensions are subtracted from the post-irradiation dimensions. Columns marked "Δx (Bond - Free)" are the differences when the post-irradiation free-side dimension is subtracted from the post-irradiation bond-side dimension.

	Δa (post - pre-irradiation)	Error	Δa (Bond - Free) [mm]	Error	Δe (post - pre) [mm]	Error	Δe (bond vs free) [mm]	Error	Δh (post – pre)	Error	Δh (bond vs free)	Error
2A	0.118	±0.027	-0.038	±0.022	0.102	±0.037	-0.235	±0.065	0.108	±0.147	-0.103	±0.106
3A	0.093	0.035	-0.023	0.039	-0.455	0.073	0.537	0.072	-0.002	0.017	-0.012	0.017
4A	0.018	0.019	0.028	0.028	0.107	0.090	-0.483	0.104	0.028	0.051	-0.007	0.044
5A	0.160	0.044	0.017	0.037	-0.087	0.066	0.300	0.060	0.003	0.046	-0.032	0.034
6A	0.077	0.053	-0.023	0.043	0.290	0.045	-0.642	0.056	0.028	0.045	-0.025	0.035
	Δb (post - pre-irradiation)	Error	Δb (Bond-Free)	Error	Δf (post – pre)	Error	Δf (bond vs free)	Error	Δi (post – pre)	Error	Δi (bond vs free)	Error
2B	0.037	±0.049	-0.057	±0.045	-0.213	±0.050	0.318	±0.062	0.010	±0.013	0.000	±0.028
3B	-0.022	0.008	0.055	0.021	0.413	0.062	-0.347	0.054	-0.013	0.012	0.010	0.018
4B	0.053	0.022	0.020	0.026	-0.050	0.410	0.225	0.294	-0.018	0.024	-0.002	0.025
5B	0.003	0.022	-0.107	0.038	0.010	0.069	-0.345	0.056	0.002	0.039	0.012	0.036
6B	0.060	0.043	-0.007	0.044	-0.205	0.023	0.350	0.026	0.000	0.028	-0.002	0.023

the change is within the error of the measurement. When irradiated at 400 °C to a fast neutron fluence on the order of 1 dpa, Palentine reported a length increase in α-SiC of 0.55%.[17] [77] At a dose of 1 dpa and higher irradiation temperature (1000 °C), Senor *et. al.* reported a smaller length increase in Hexoloy SA of about 0.15%. [65] The data in the first column of Table 4.7 are within the reported ranges: above the data from Senor *et. al.*, but mostly lower than the data from Palentine. Based on the literature, then, small length increases should have been observed (between 0.15% and 0.55%) and this was indeed the case. The first column in Table 4.8 shows the % change of the lengths of the Hexoloy SA blocks after their time in the ACI loop. The % change in length ranges from 0.015 % to 0.719 %. Considering that these specimens were irradiated at a relatively low temperature of 300 °C, where dimensional expansion is more pronounced, these values are not unreasonable in the context of the data from Senor *et. al.* and Palentine which were obtained at higher irradiation temperatures. That said, the spread in the extent of lengthening is surprising. Looking at dimensions "e" and "f", the widths of the blocks, it is difficult to find a trend in the data. Some of the specimens saw slight increases in their widths, and others saw slight decreases. A striking observation comes when comparing the two halves of a given numbered specimen. For example, compare the % changes in the "e" and "f" dimensions from Table 4.8. It seems that an increase in the "e" dimension on sample XA is linked to a corresponding decrease in the "f" dimension on sample XB and vice versa. In the case of samples 3A and 3B, for example, the "e" dimension decreases by 3.8 % and the "f" dimension increases by 3.6 %. This type of behavior is evident in the other sample pairs as well.

[17] Recall that the fluence seen by the bond specimens was 1.59 x 10^{20} n/cm^2.

Table 4.8: Percent difference between the irradiated and un-irradiated states of the bond specimens. The free and bond-sides of the same block are also compared.

	% diff a (pre-irradiated vs. post-irradiated)	% diff a bond to a free (post irradiation)	% diff e (pre-irradiated vs. post-irradiated)	% diff e bond to e free (post irradiation)	% diff h free (pre-irradiated vs. post-irradiated)	% diff h bond to h (free post irradiation)
2A	0.530	-0.171	0.858	-1.986	1.151	-1.092
3A	0.417	-0.104	-3.830	4.590	-0.018	-0.124
4A	0.082	0.127	0.830	-3.801	0.301	-0.071
5A	0.719	0.074	-0.672	2.316	0.035	-0.337
6A	0.343	-0.104	2.210	-4.902	0.301	-0.265

	% diff b (pre-irradiated vs. post-irradiated)	% diff b bond to b free (post irradiation)	% diff f (pre-irradiated vs. post-irradiated)	% diff f bond to f free (post irradiation)	% diff i free (pre-irradiated vs. post-irradiated)	% diff i bond to i free (post irradiation)
2B	0.164	-0.253	-1.778	2.665	0.106	0.000
3B	-0.097	0.246	3.610	-2.965	-0.142	0.106
4B	0.239	0.089	-0.394	1.763	-0.195	-0.018
5B	0.015	-0.478	0.077	-2.690	0.018	0.124
6B	0.268	-0.030	-1.564	2.676	0.000	-0.018

If the bond between the two A and B halves of a bond specimen was constraining the expansion of the width of the blocks, one would expect to see that the bond-side width would be less than the un-bonded-side width after irradiation. Both the bond-sides and un-bonded-sides were measured and compared. In some cases one was greater than the other, but no clear trend developed. In order to effectively compare the dimensions of the block widths, the % change in the widths (pre-irradiation vs post-irradiation) of the free-side and the bond-side must be compared. If the % change in the width of the bond-side is less than the % change in the width of the free-side, then it would be reasonable to conclude that the bond is constraining the linear swelling. This comparison could not be made because the bond side dimensions had not been measured prior to irradiation.[18]

Anisotropic dimensional changes were observed, and these would certainly stress the bond at the interface between the two Hexoloy SA blocks. This anisotropy would apply a shear stress to the bond and may have contributed to its failure. Density measurements were made in order to determine if there was net volumetric swelling in the samples.

4.2.7 Bond Specimen Volumetric Swelling

Since the results of the dimensional measurements were somewhat difficult to analyze, the densities of the irradiated specimens were measured in order to determine if there were any volumetric changes. The densities of the failed irradiated bond specimens were compared to densities of un-irradiated Hexoloy SA blocks.

[18] It should also be mentioned that the specimens were in contact with the sample module and any force exerted by the samples on the module due to irradiation induced swelling may have also been a factor.

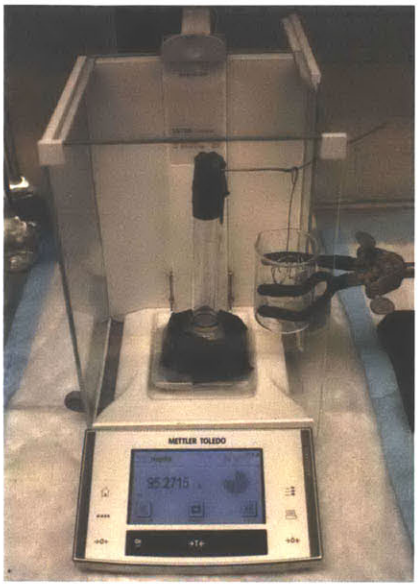

Figure 4.25: Experimental setup for determining sample density via Archimedes' method.

Experimental Procedure The densities were measured using Archimedes' method which works on the basis that the buoyant force exerted on a body immersed in a fluid is equal to the mass of the fluid displaced by the immersed body. The organic solvent xylene (C_8H_{10}) was used as the buoyant fluid because it has a low surface tension[19], relatively low volatility, and a reasonable density not much less than that of water. First, the samples were weighed on a balance with an accuracy to 1 in 1 x 10^5 g. Next, the density of the xylene was determined by filling a 50 mL volumetric flask to the marking and weighing the flask. The flask itself was calibrated before-hand using de-ionized water, so that the actual volume of the flask was known accurately prior to using it in the measurement of the xylene density. Since the sample densities were measured on different days, the temperature of the xylene fluctuated with the air temperature in the lab. Thus, each day, the density of the xylene was measured prior to measuring the sample densities. The experimental setup is pictured in Figure 4.25. A wire basket was hung on a structure attached to the base plate of the scale such that the basket was immersed in the xylene. The scale was then tared. The sample was then placed in the wire basket and immersed in the xylene. Knowing the dry weight of the sample, the density of the xylene, and the weight of the sample when immersed in the xylene, the density of the sample can be calculated according to the following scheme.

$$m_{displaced\,xylene} = m_{SiC\,dry} - m_{SiC\,immersed} \tag{11}$$

$$m_{displaced\,xylene} = V \times \rho_{xylene} \tag{12}$$

$$V = \frac{m_{displaced\,xylene}}{\rho_{xylene}} \tag{13}$$

$$\rho_{SiC} = \frac{m_{SiC\,dry}}{V} \tag{14}$$

[19]Low surface tension allows thorough wetting of the surfaces of the sample.

Table 4.9: Densities of irradiated bond samples and un-irradiated control samples.

(a) Irradiated bond sample densities.

	Density (g/cm^3)	Error (± g/cm^3)	Relative Error (%)
2A	3.0892	0.0077	0.2504
2B	3.0894	0.0073	0.2366
3A	3.0915	0.0121	0.3907
3B	3.0900	0.0011	0.0342
4A	3.0931	0.0076	0.2444
4B	3.0889	0.0088	0.2863
5A	3.0893	0.0089	0.2868
5B	3.0895	0.0086	0.2778
6A	3.0917	0.0089	0.2871
6B	3.0894	0.0098	0.3179

(b) Un-irradiated Hexoloy SA density.

Un-irradiated Hexoloy SA Sample #	Density (g/cm^3)	Error (± g/cm^3)	Relative Error (%)
93	3.1431	0.0016	0.0519
92	3.1458	0.0022	0.0693
83	3.1446	0.0042	0.1347
78	3.1447	0.0046	0.1465
77	3.1438	0.023	0.7322
76	3.1434	0.0095	0.3026

Table 4.10: Summary of the irradiation induced density changes in the bond specimens.

	Average Density (g/cm^3)	Error (± g/cm^3)
Un-irradiated	3.1442	0.0068
Irradiated	3.0902	0.0250

Un-irradiated Density – Irradiated Density = 0.0540 g/cm^3
error: ± 0.0259 g/cm^3

% volumetric swelling ($\frac{UnIrradiated\,Density - Irradiated\,Density}{UnIrradiated\,Density} \times 100\%$) : 1.72 %
error: ± 0.82

The weight of the dry specimen is given by $m_{SiC\,dry}$. The weight of the specimen while immersed in the xylene is given by $m_{SiC\,immersed}$. The volume of the displaced xylene equals the volume of the sample, and is given by V. The measured density of the xylene is given by ρ_{xylene}. Finally, the density of the SiC sample is given by ρ_{SiC}. Substituting Equation 11 into Equation 13 gives the following:

$$V = \frac{m_{SiC\,dry} - m_{SiC\,immersed}}{\rho_{xylene}} \tag{15}$$

Solving for $\frac{m_{SiC\,dry}}{V} = \rho_{SiC}$ results in Equation 16, which may be used directly to find the density of the Hexoloy SA specimens.

$$\rho_{SiC} = \frac{m_{SiC\,dry} - m_{SiC\,immersed}}{\rho_{xylene}} \tag{16}$$

Density Measurement Results The densities of the un-irradiated Hexoloy SA samples are listed in Table 4.9a. The densities of the un-irradiated samples are tabulated in Table 4.9b. A summary of the density data and the calculated volumetric swelling is provided in Table 4.10. At the irradiation temperature of 300 °C, swelling in SiC is by the accumulation of point defects: vacancies and interstitials. [38] In addition to point defect swelling, Hexoloy SA

will also experience swelling as a result of helium production. Recall that a boron sintering aid (0.6 w/o) is used in the manufacture of Hexoloy SA. In a thermal neutron flux, ^{10}B will capture a neutron and release an alpha particle (helium nucleus) which will tend to nucleate at the grain boundaries. In their work, Senor *et. al.* calculated that the ^{10}B sintering aid should be completely consumed in the Advanced Test Reactor (ATR) after 100 EFPD and a fluence of approximately 2.70 x 10^{24} n/m^2 (E > 0.1 MeV). [65] The fluence seen by the bond specimens irradiated in the MITR-II is comparable at 1.59 x 10^{24} n/m^2 (E > 0.1 MeV); therefore, the swelling due to helium evolution in the bond specimens should be close to saturation.

Unlike Hexoloy SA, CVD SiC irradiated at 300 °C, experiences swelling solely from point defect accumulation. The initial rate of swelling in SiC is quite high — 1.0 % swelling has been reported for CVD SiC after only 0.1 dpa. [38] Beyond 0.1 dpa, the rate of swelling decreases until it saturates at a volumetric swelling of between 1.1 % and 1.7 % at a neutron dose equivalent to about 1 dpa. [38] Recall that the bond specimens tested here were calculated to have experienced 0.159 dpa and 1.72 % swelling. No saturation swelling data could be found for Hexoloy SA in the literature, but Senor *et. al.* have reported that Hexoloy SA experiences swelling twice that of CVD SiC at 0.5 dpa. Thus, the saturation swelling of Hexoloy SA should also be higher than the saturation swelling of CVD SiC. The measured swelling for the bond specimens is 1.72 % which falls right on the saturation swelling for CVD SiC. At the doses seen by the bond specimens, it is likely that swelling due to helium is at or near saturation and that slight additional swelling due to point defect accumulation would occur at higher fluences before saturating at around 1 dpa.

The density measurements via the Archimedes' method have clearly established volumetric swelling in the bond specimens. It turns out that densities calculated from the masses and the measured dimensions of each block are consistent with the swelling measured via the Archimedes' method. Since the measured dimensional changes have significant anisotropy, it is concluded that the swelling of the bond specimens also has a significant degree of anisotropy. This differential swelling would have introduced shear stresses onto the bonds and contributed to their failure.

5 Thermal Diffusivity of Irradiated and Un-Irradiated Triplex Samples

A successful cladding design must be able to effectively conduct heat from its inner radius, facing the fuel, to the outer radius, where it may be removed by the coolant. This places importance on the heat conduction ability of the cladding. For instance, in the event of an accident such as a LOCA, cooler water from the ECCS will enter the core which may cause thermal shock to hot core internals like the cladding. A high thermal diffusivity/conductivity will reduce the cladding's susceptibility to fracture by thermal shock. Radiation damage may significantly reduce the thermal diffusivity of the cladding by introducing defects which scatter the phonons responsible for heat conduction in SiC. Comparing the thermal diffusivity of SiC samples before and after irradiation is important for understanding irradiation effects on thermal conduction in SiC. It may also be used to compare the extent of radiation damage experienced between samples irradiated to different doses. The layered Triplex samples are somewhat of an unknown quantity as far as heat conduction is concerned. Heat from the inside of the Triplex cladding must first be conducted through the monolith. Then it must traverse the boundary between the monolith and the composite layer. Finally, it must traverse the boundary between the composite layer and the EBC. Each boundary crossing represents an obstacle to heat transfer. Testing Triplex samples and monolith only samples will help to determine the heat conduction characteristics of SiC cladding.

5.1 Sample selection and preparation for thermal diffusivity measurements

Several un-irradiated and irradiated Triplex tubes along with several irradiated monolith only tubes were selected for thermal diffusivity measurements. Table 5.1 lists the samples, their constructions, and their dose exposures. Owing to the relative scarcity of SiC tube samples, the majority of the samples listed in Table 5.1 had been hoop tested prior to their preparation for thermal diffusivity measurements. Only samples 25-1 and 26-2 were as-irradiated specimens. For thermal diffusivity sample preparations, small square sections were cut out of the undamaged portions of the hoop tested tubes. Only sections whose inner and outer surfaces remained pristine and whose layers were intact were prepared. The irradiated specimens (especially the monolithic SiC) presented a challenge owing to their radioactivity and brittle nature. Thus, a series of aluminum clamps were designed in order to securely hold the samples while they were cut into pieces approximately 5.9 mm square using a Buehler Isomet low-speed saw equipped with a micrometer and a diamond coated blade. The clamps and the saw are pictured below in Figure 5.1. Additional images of the clamps are provided in Figure 5.2. A typical thermal diffusivity square cut from a Triplex sample is shown in Figure 5.3. The thickness of each sample was measured as this thickness is required input for the thermal diffusivity measurements.

Table 5.1: Constructions, exposures, and dpa for Triplex samples and monolith only samples tested for thermal diffusivity. *Monolith-only samples α-2 and T-1 were in the ACI loop, however they were located above the core. Samples 04-A through 06-C were never in the ACI loop. A discussion of the dpa calculation may be found in Section 3.3.2.

	Monolith Type	Composite Fiber Type / Matrix	EBC	MWd	Fluence (n/m^2)	dpa
04-A	Trex	Hi-Nicalon-S / CVI	HyperTherm CVI	-	-	-
04-B	Trex	Hi-Nicalon-S / CVI	HyperTherm CVI	-	-	-
06-B	Trex	Hi-Nicalon-S / CVI	HyperTherm CVI	-	-	-
06-C	Trex	Hi-Nicalon-S / CVI	HyperTherm CVI	-	-	-
25-1	Trex	Hi-Nicalon-S / CVI	HyperTherm CVI	848	0.99×10^{25}	0.99
26-2	Trex	Hi-Nicalon-S / CVI	HyperTherm CVI	848	0.99×10^{25}	0.99
α-2	α-SiC	-	-	0	0	0
T-1*	Trex	-	-	0	0	0
T-2	Trex	-	-	933	1.09×10^{25}	1.09

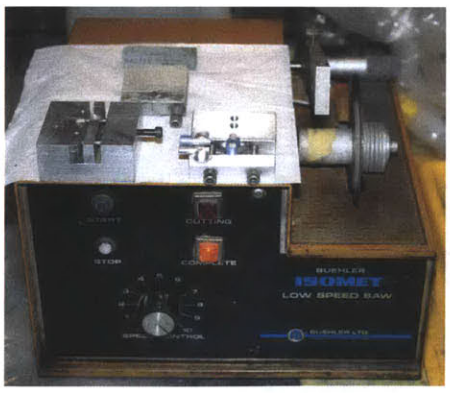

(a) Buehler Isomet saw with three sample clamps.

(b) Diamond-coated blade and clamp mounting arm.

(c) Micrometer attached to clamp arm.

Figure 5.1: Buehler Isomet low-speed saw with sample clamps.

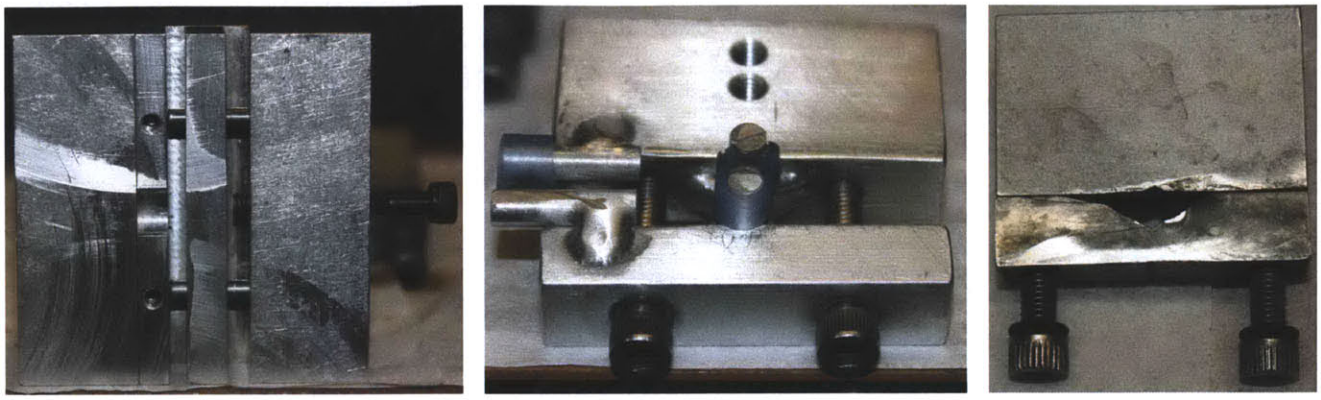

(a) Clamp for cutting the correct width of an already sectioned SiC piece.

(b) Clamp for sectioning and cutting hoop test shards to the correct length.

(c) Clamp for cutting whole tubes to correct length.

Figure 5.2: Clamps used for thermal diffusivity sample preparation.

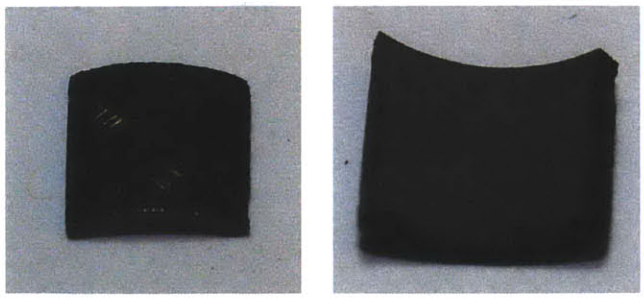

(a) Triplex thermal diffusivity square. Concavity facing down.

(b) Triplex thermal diffusivity square. Concavity facing up.

Figure 5.3: Concave up and concave down views of a Triplex thermal diffusivity square.

Ideal specimens for thermal diffusivity measurements using the flash method (the method employed here and discussed in the next section) have parallel plane surfaces on their top and bottom faces. Some uncertainty existed over the effect the curvature of the samples would have on the thermal diffusivity measurements. In order to address this, measurements were made with the concavity facing both up and down. These data are compared and discussed in Sections 5.4 and 5.5.

5.2 Thermal diffusivity measurement apparatus and procedure

The thermal diffusivity was measured via the thermal flash technique using a Netzsch LFA 447 NanoFlash® instrument. The LFA 447 uses a high power xenon flash lamp to flash the underside of the specimen, imparting thermal energy over the bottom face of the sample. A liquid nitrogen cooled InSb infrared detector then measures the temperature increase on the top face of the sample with respect to time. The thermal diffusivity is then calculated from the resulting temperature vs. time plot by using the included Netzsch Proteus®software. A schematic of the instrument internals as well as the instrument setup at the NRL is pictured in Figure 5.4.

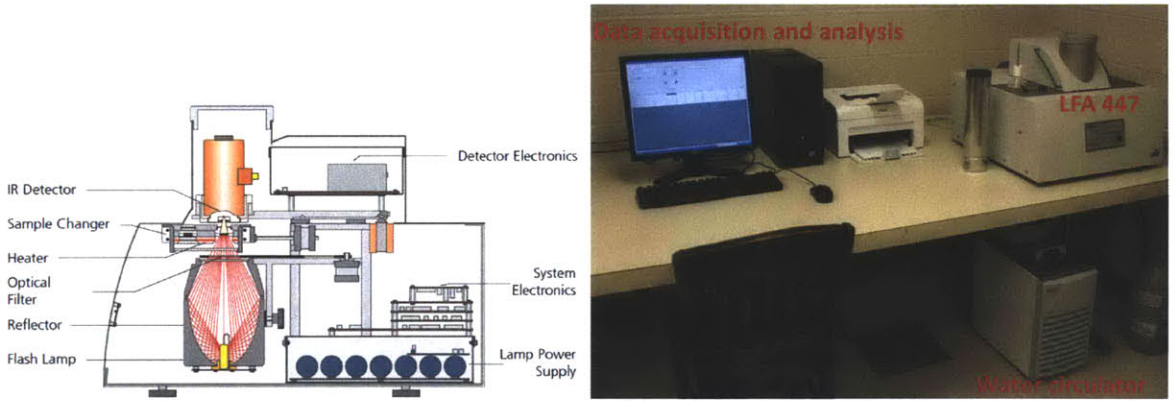

(a) Schematic of Netzsch LFA 447 design.

(b) LFA 447 setup at the NRL.

Figure 5.4: Schematic and setup of LFA 447.

In order to ensure that thermal energy is uniformly absorbed and emitted on the bottom and top faces of the specimen respectively, the sample is coated with a thin film of graphite. The sample is then placed in the sample holder which has space for four samples at a time. As was mentioned above, the thermal diffusivities were measured twice: once with the sample curvature facing down toward the lamp and once with the sample curvature facing up toward the detector. Figure 5.5 shows the empty sample holder with its circular masks. The masks are placed over the top of the samples in order to prevent any of the xenon lamp's energy from flashing through any gaps between the sample and the square sample holder. Figure 5.6 shows a sample holder with a sample inserted in both up and down directions.

The LFA 447 has a programmable heater mounted below the sample holder allowing it to measure the thermal diffusivity of the samples from room temperature (25 °C) up to 300 °C. Additionally, a Thermo Scientific recirculator is used to help control the sample temperatures by pumping water at 23 °C through a heat sink below the sample

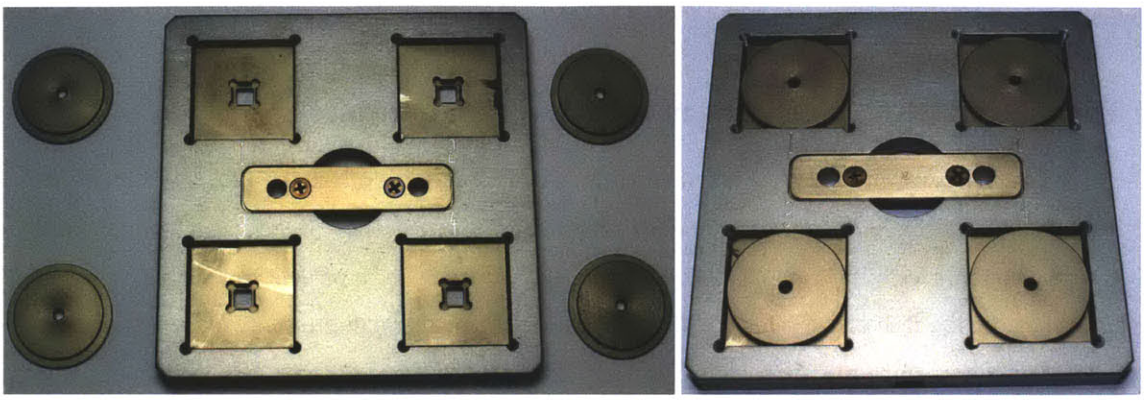

(a) Empty sample holder with masks.

(b) Sample holder with masks in place.

Figure 5.5: LFA 447 sample holders.

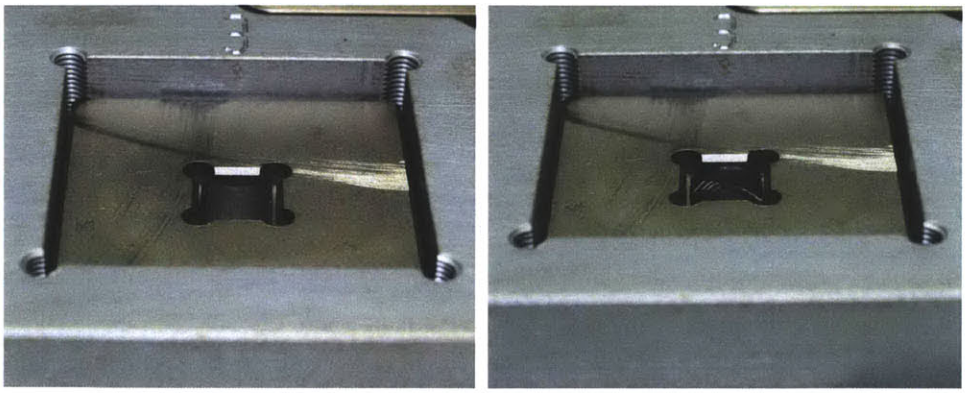

(a) Sample in holder with curvature facing up.

(b) Sample in holder with curvature facing down.

Figure 5.6: Triplex sample inserted in sample holder showing curvature up and down.

holder. Once the samples had been loaded, the LFA 447 was programmed to measure the thermal diffusivity of each sample 5 times at 25, 50, 75, 100, 150, 200, 250, and 300 °C.

5.3 Calculation of thermal diffusivity from LFA 447 output

The flash method for measuring thermal diffusivity was developed by Parker *et. al.* in 1961. [78] With their experimental setup, Parker and co-workers plotted a dimensionless curve with the same shape as that of the detector response vs. time plot displayed in Figure 5.7a. On the y-axis they plotted the dimensionless parameter $W = \frac{T}{T_{max}}$, where T is the temperature of the detector-side surface of the sample at a given time after the initial flash, and T_{max} is the maximum temperature achieved by the detector-side face of the sample. On the x-axis they plotted the following dimensionless parameter:

$$\omega = \frac{\pi^2 \alpha t}{L^2} \tag{17}$$

In the parameter ω, α is the thermal diffusivity in cm^2/s, t is the time in seconds, and L is the sample thickness in cm. In Parker's plot, when W = 0.5, $\omega = 1.38$, and t = "$t_{\frac{1}{2}}$" which is the time required for the detector-side surface of the sample to achieve half of the maximum temperature T_{max}. The thermal diffusivity was then calculated as follows:

$$\alpha = \frac{1.38 L^2}{\pi^2 t_{\frac{1}{2}}} \tag{18}$$

Again, α is the thermal diffusivity in cm^2/s, L is the sample thickness in cm, and $t_{\frac{1}{2}}$ is the time required for the detector-side surface to achieve half of the maximum temperature T_{max}.

A few years later, in 1963, Cowan developed a correction to the Parker method. This correction accounts for the radiative and convective heat losses which may be significant enough that the maximum temperature on the detector-side of the sample may only reach 10 - 20% of the value in the absence of losses. [79] The Netzsch Proteus software can be used to include the Cowan correction in the calculation of the thermal diffusivity at each temperature. Figure 5.7a shows the detector response typical of the SiC samples at a measurement temperature of 25 °C.[20] At time t = 0, the lamp flashes which registers a small spike at t = 0. The "detector response" (which is related to the temperature measured on the top face of the sample) quickly increases before leveling off and decreasing more gradually as heat is lost from the sample. Figure 5.7b shows the detector response curve with the fitted Cowan correction. The thermal diffusivity is then calculated from this fitted correction according to Equation 18.

5.4 Thermal diffusivity results for un-irradiated Triplex samples

The curvature of the sections of the tubular samples was a concern for the thermal diffusivity measurements. The theory developed by Parker, Cowan, and others over the years dealt only with samples having parallel top and bottom surfaces, and the instruments were built and calibrated for these types of specimens. In order to investigate the possible

[20] The shape of the detector response curve remains the same at any temperature. At higher measurement temperatures, the spike at t = 0 is smaller compared to the rest of the signal.

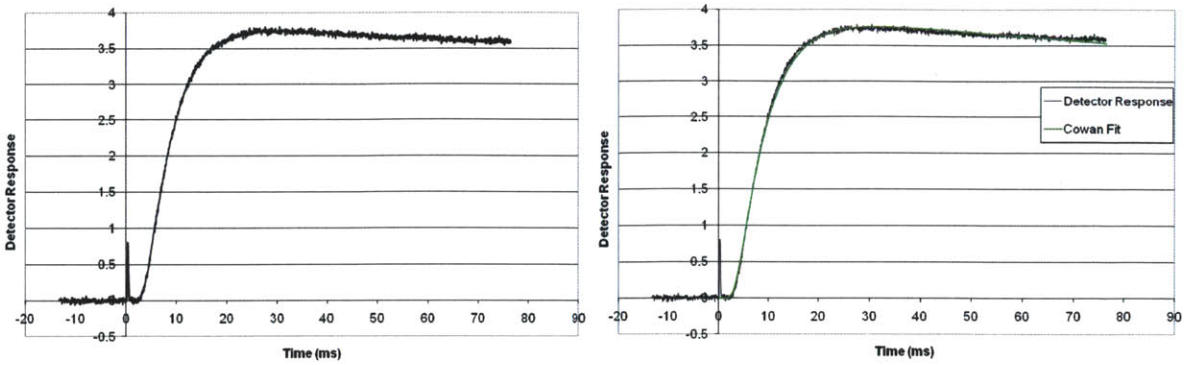

(a) Detector response vs. time at 25 °C.

(b) Detector response with Cowan fit.

Figure 5.7: LFA 447 detector response vs time with and without Cowan fit.

effects of having slight curvature in the samples, a total of 11 un-irradiated Triplex samples[21] (and 5 irradiated samples) were evaluated with the curvature facing both down and up with respect to the detector. The down and up data were then compared in Figure 5.8. The same plots from Figure 5.8 are re-plotted in 2D form in Figures 5.9 through 5.11 so as to show additional features. The plots show that the measurements taken with the curvature facing up are right on top of the measurements taken with the curvature facing down. In most cases, the up and down measured values for a given sample differ by less than 2 % at their point of greatest disparity. In the most dramatic difference between up and down measurements, 04-B 2 in Figures 5.8a and 5.9, the difference between the up and down measurements was 3.4 mm^2/s (12.5 %) at 25 °C, which diminished to a difference of 0.2 mm^2/s (1.5%) at 300 °C. Recall that heat conduction in SiC is primarily by lattice waves (phonons).[22] The thermal diffusivity decreases as the measurement temperature increases because phonon-phonon (umklapp) scattering increases with temperature to overcome the scattering contributions from grain boundary scattering and defect scattering.

An anomaly was observed in the plots for samples 04-A 1 (Figure 5.8a) and 06-B 2 (Figure 5.8b). The anomalies are more easily observed in the plots in Figures 5.9 and 5.10. In the 04-A 1 plot, the difference between the up and down measurements is 0.2 mm^2/s at temperatures of 75 °C and above. At 25 °C, the difference is 0.8 mm^2/s, but it is not unusual for the differences in the measurements taken at room temperature to be larger than the differences at higher measurement temperatures. There is, however, a slight jog in the plot for "04-A 1 down" at 50 °C which places the measured value above that for "04-A 1 up". This data point is the only point in the comparison where the down measurement is above the up measurement. The jog in the plot is more dramatic for the comparison of "06-B 2 down" and "06-B 2 up". At a measurement temperature of 75 °C, the difference between the two plots suddenly jumps from a difference of less than 0.1 mm^2/s at 50 °C to a difference of 3.8 mm^2/s at 75 °C. After this jump, at 100 °C, the difference drops to less than 0.1 mm^2/s; and the difference never exceeds 0.4 mm^2/s after 100 °C. The cause of these apparent anomalies is unknown; however, they are easily averaged out.

It is also important to note that different samples cut from the *same* Triplex tube may have been measured to have different thermal diffusivities. The most dramatic example is the difference between sample "06-C 2" and the other

[21] From Triplex tube 04-A, 2 squares for thermal diffusivity were fabricated. From Triplex tube 04-B, 2 samples were fabricated. From Triplex tube 06-B, 3 samples were fabricated for thermal diffusivity, and from Triplex tube 06-C, 4 samples were fabricated.

[22] See Section 2.1.2

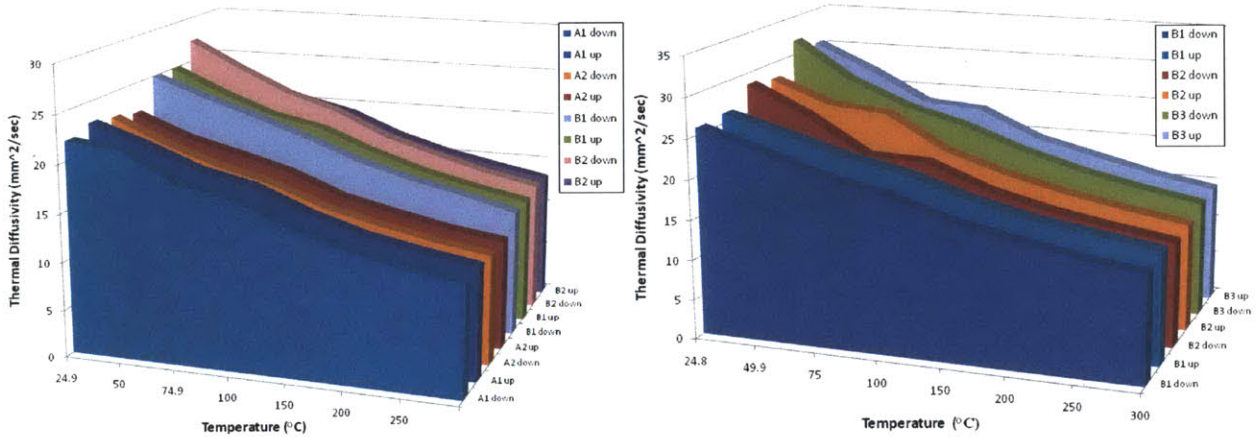

(a) Thermal diffusivity for samples cut from Triplex tubes 04-A and 04-B.(b) Thermal diffusivity for 3 samples cut from Triplex tube 06-B. Mea-
Two samples were cut from each tube. Each sample was measured withsurements were taken with curvature facing up and down.
the curvature facing up and down.

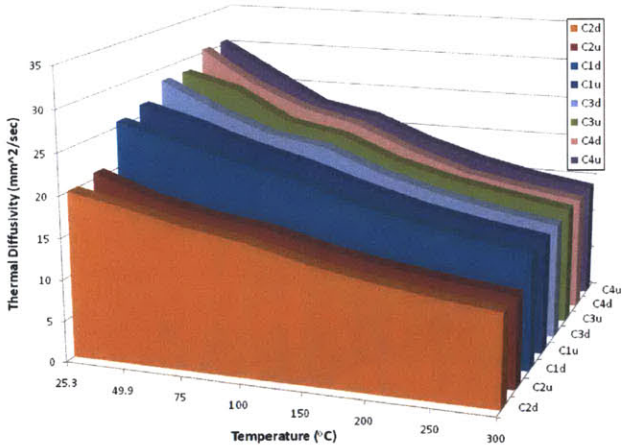

(c) Thermal diffusivity for 4 samples cut from Triplex tube 06-C. Mea-
surements were taken with curvature facing both up and down.

Figure 5.8: Comparison of the thermal diffusivities of 11 samples from 4 different Triplex tubes. For each of the 11 samples, the thermal diffusivity when the curvature is facing both up and down is plotted. Also see Figures 5.9 through 5.11 for 2D plots of the same data.

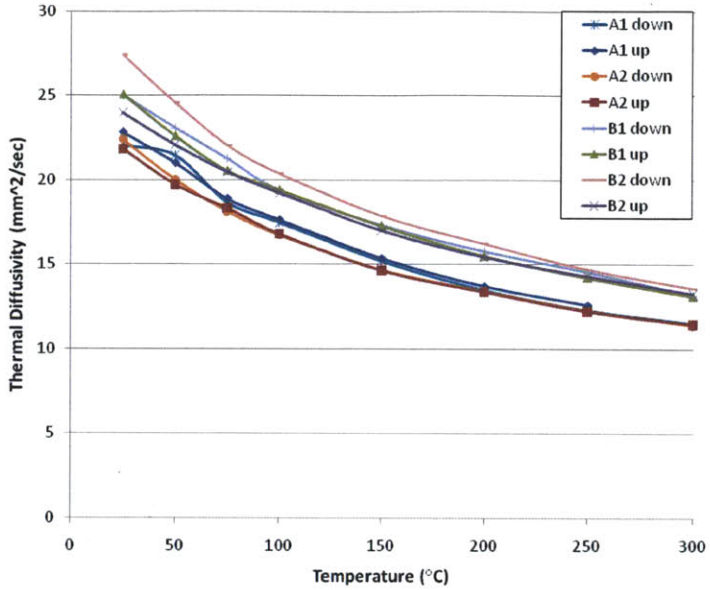

Figure 5.9: Thermal diffusivity of un-irradiated Triplex samples 04-A and 04-B. This is a 2D view of the plot from Figure 5.8a.

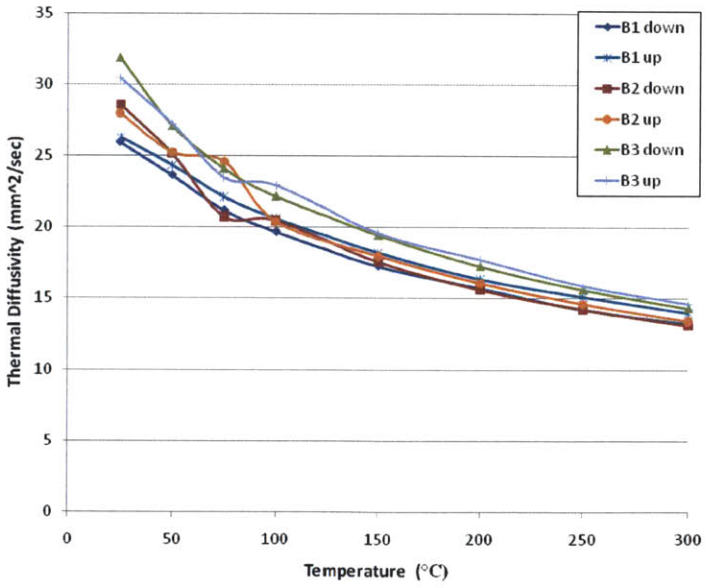

Figure 5.10: Thermal diffusivity of un-irradiated Triplex sample 06-B. This is a 2D view of the plot from Figure 5.8b.

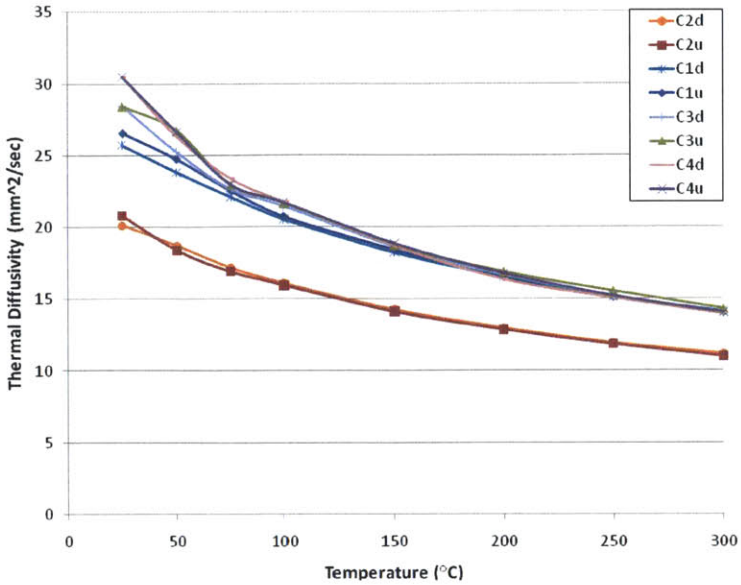

Figure 5.11: Thermal diffusivity of un-irradiated Triplex sample 06-C. This is a 2D view of the plot from Figure 5.8c.

06-C samples. The difference between sample 06-C 2 and samples 06-C 1 and 06-C 3 ranges between 5 and 6 mm^2/s. This difference is most likely due to damage to the interface between two or more layers of sample 06-C 2. The damage may have occurred when the sample was being cut for the thermal diffusivity measurements. Each of the four Triplex tubes from which thermal diffusivity squares were fabricated had been hoop tested. It is also possible that the hoop testing damaged the interface between the layers. Another possibility is that the layers in one part of the tube were in better contact with each other from the time of fabrication. Discontinuities at layer boundaries (and layer interfaces in general) would introduce strong phonon scattering centers which would degrade the thermal diffusivity. [80]

Since the differences between the curvature up and curvature down measured values for each sample were small, the plots from the group of samples which were cut from the same Triplex tube were averaged in order to arrive at an average thermal diffusivity for each of the four un-irradiated Triplex tubes. Figure 5.12 shows the thermal diffusivity plots for the four different tubes along with plots of similar composite SiC samples published by Yamada *et. al.* in Reference [81]. The data from Yamada *et. al.* were obtained for non-tubular SiC/SiC_f composites constructed of Hi-Nicalon Type S fibers infiltrated with a CVI SiC matrix. This is the same technique used to construct the composite layer of the Triplex samples. (See Table 5.1 for the constructions of the four Triplex samples.) No monolithic layer of SiC was present in these samples. Yamada's group also published data on the thermal diffusivity of composites utilizing a Tyranno SA SiC fiber with a CVI SiC matrix, which are also plotted in Figure 5.12 for comparison. The measured data for the Triplex tubes and the data published by Yamada *et. al.* are similar. Despite being constructed with three separate and distinct layers, the Triplex cladding designs exhibit higher thermal diffusivity than the composite-only data from Yamada and co-workers. The samples tested in the work by Yamada were 2.5 - 3.5 mm thick, and their entire thickness was made up of the CVI SiC/Hi-Nicalon Type S (or Tyranno SA) fibers. Roughly half of the ~ 1 mm thickness of the Triplex tubes was monolithic CVD SiC, and the other half was the CVI SiC matrix with

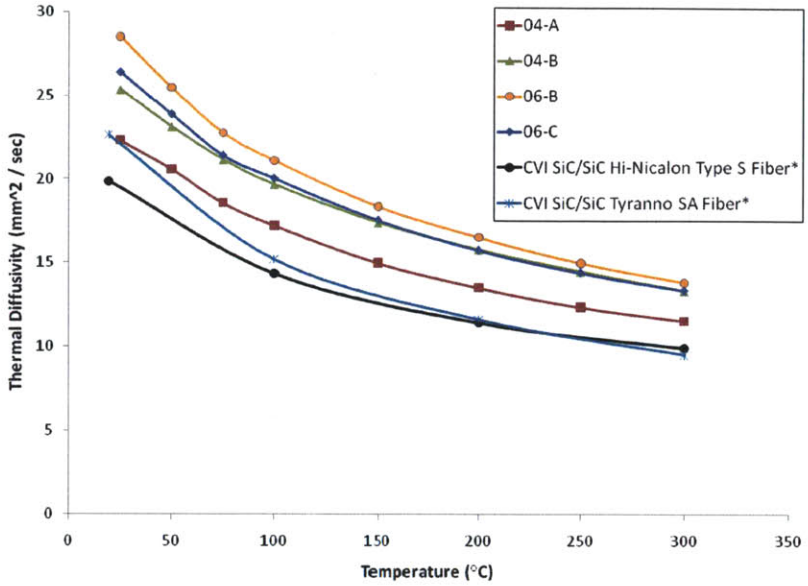

Figure 5.12: Averaged thermal diffusivities for the 4 un-irradiated Triplex samples. Published thermal diffusivities for un-irradiated CVI SiC composites (having no monolithic layer) made from high purity SiC fibers are plotted for comparison from [81].

Hi-Nicalon Type S fibers covered by the thin EBC on the outermost surface. Since the Triplex samples show a higher thermal diffusivity than the composite only samples of Yamada *et. al.*, this suggests that the thermal diffusivity of the composite layer is limiting.

Two more comparisons are in order. First, the thermal diffusivity of as-fabricated Zircaloy-4 cladding was measured by Bunnell *et. al.* to be 5.8 mm^2/s at 25 °C and 7.0 mm^2/s at 300 °C. [82] The thermal diffusivity of the un-irradiated Triplex samples ranges from 20 to 28.5 mm^2/s at 25 °C and 10 to 16 mm^2/s at 300 °C. So, in as-fabricated condition, the thermal diffusivity (and conductivity) of the Triplex samples is an improvement over Zircaloy.[23] The second comparison is between monolithic CVD SiC and Triplex SiC: the thermal diffusivity of un-irradiated CVD SiC (as measured by Senor *et. al.* [65]) is considerably higher than that of the un-irradiated Triplex samples. In Figure 5.13 the data reported in [65] are reproduced for reference. At temperatures of 25 °C and 300 °C, the thermal diffusivities from Figure 5.13 are 123 mm^2/s and 42 mm^2/s respectively. This is further evidence that composite SiC has reduced thermal diffusivity due to the phonon scattering centers introduced at the interfaces between the monolith, composite, and EBC layers.

5.5 Thermal diffusivity of irradiated monolithic and Triplex tube samples

The thermal diffusivities of irradiated monolithic CVD SiC and irradiated Triplex samples were measured in the same manner as the un-irradiated specimens. Each sample was measured with the curvature facing up and down. Once it was determined that the up and down measurements were equivalent, the up and down data were averaged in order to

[23] Radiation is known to significantly reduce the thermal diffusivity/conductivity of SiC, an effect that will be addressed in the following sections. The estimated thermal conductivity for the Triplex samples, calculated from the diffusivity data, is compared with published thermal conductivities for Zircaloy in Section 5.5.2.

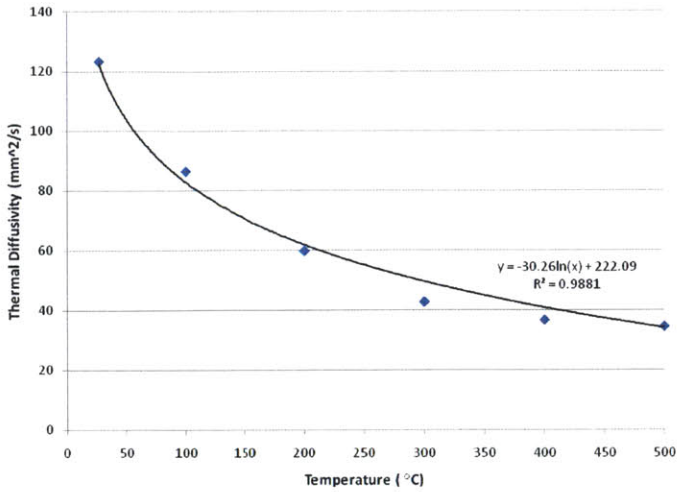

Figure 5.13: Thermal diffusivity of un-irradiated monolithic CVD SiC (β-SiC). Adapted from Senor *et. al.* (Reference [65]).

arrive at a final value for the thermal diffusivity of each specimen. A total of five specimens from the ACI loop were investigated. Their constructions and neutron exposures are listed in Table 5.1. In all, two irradiated Triplex samples and three monolithic samples were measured. Sample T-1 had been inside the ACI loop for the same amount of time as sample T-2; yet, T-1 had been located above the core and did not receive significant neutron exposure. Sample α-2 is made of monolithic α-SiC but was tested in the ACI loop above the core so it did not see significant neutron exposure. The α-SiC will be compared to the β-SiC used in all of the CVD Trex monoliths.

5.5.1 Thermal diffusivity of irradiated monolithic SiC

Beginning with the three monolithic SiC tubes, Figure 5.14 shows the thermal diffusivities for the up and down-facing trials of samples T-1 A, T-2 A, and α-2 A. This figure demonstrates the near equivalency of the data regardless of the orientation of the sample, especially at temperatures of 100 °C and higher. A small jog in the curves for samples α-2 A and T-2 A exists at 75 °C. This is the same type of anomaly observed at 75 °C in plots for the un-irradiated Triplex samples 04-A 1, 06-B 2, and 06-C 4 (Section 5.4 and Figures 5.8a, 5.8b, and 5.8c). The origin of this slight disturbance in the thermal diffusivity plots is unknown. The fact that it appears in a number of the sample plots, suggests that it may be systemic to the detector in the LFA 447.

Since plotting sample T-2 A together with samples T-1 A and α-2 A (in Figure 5.14) obscures features of its thermal diffusivity curve, T-2 A is plotted by itself in Figure 5.15. The *averages* of the up and down measured values for each of the three monolith-only samples are plotted together in Figure 5.16. One of the key observations to take away from Figure 5.16 is that the thermal diffusivity of T-1 A is higher (by a factor of 14 at room temperature) than that of T-2 A despite the two samples sharing the same construction (Trex monolith). The difference is that T-1 A was positioned in the portion of the ACI loop above the reactor core and T-2 A was in the middle of the core. This means that the radiation damage accumulated by T-1A should be minimal (~ 0 dpa) compared to the 1.09 dpa calculated for T-2 A.

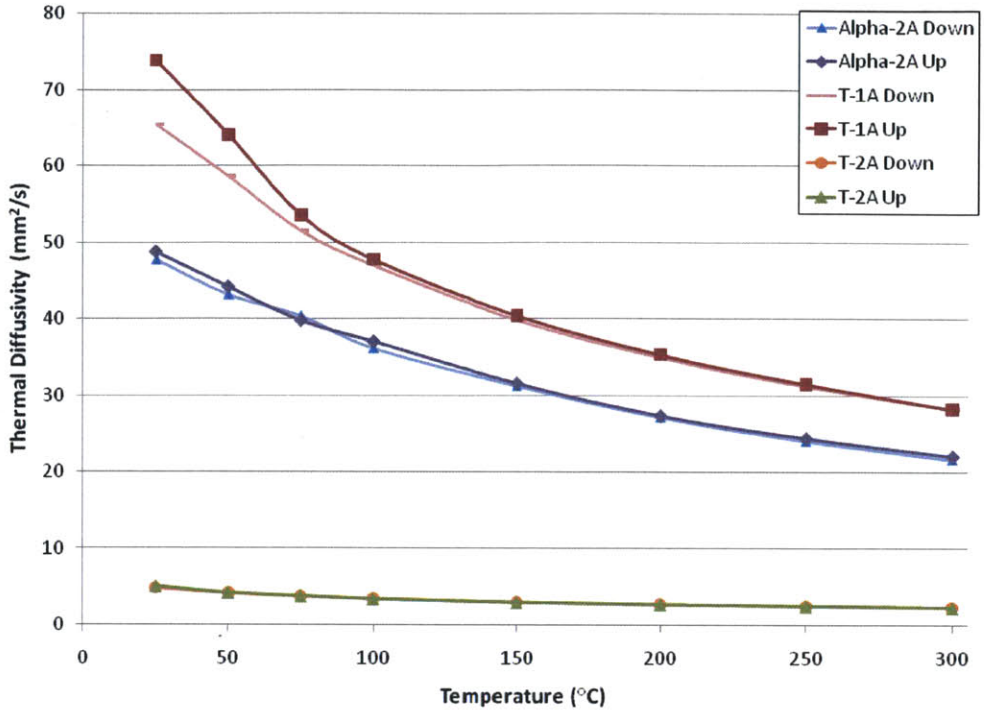

Figure 5.14: Thermal diffusivities for the irradiated monolithic SiC samples. Measurements made with the curvature facing up and down are plotted.

As radiation damage and atom displacements accumulate in a ceramic, they introduce more and more defects into the SiC lattice.[24] This, in turn, increases the phonon-defect scattering and reduces the thermal diffusivity with increasing dpa. Eventually, enough defects will have accumulated that a saturation thermal diffusivity will be reached. At an irradiation temperature of 300 °C, the reduction in the thermal diffusivity of CVD SiC has been shown to saturate by about 1 dpa. [38] This would suggest that the thermal diffusivity for sample T-2 A has reached saturation. Another radiation effect evident in the figures is that the phonon-defect scattering becomes comparable to or exceeds the phonon-phonon scattering which has the effect of reducing the temperature dependence of the thermal diffusivity.

An interesting comparison is that the thermal diffusivity for T-1 A (which remained above the MITR-II core and should have sustained negligible radiation damage) is considerably lower than the thermal diffusivity measured by Senor *et. al.* for un-irradiated CVD SiC (See Figure 5.13). At room temperature, Senor and co-workers' as-fabricated CVD SiC has a thermal diffusivity of 123 mm^2/s compared to 70 mm^2/s for sample T-1 A. There are a number of possible explanations for this difference. First, although T-1 A appears to be a pristine sample, it is possible that it has some small amount of micro-damage as a result of the T-1 tube having been hoop tested prior to the thermal diffusivity measurements. This seems unlikely given the fact that the irradiated monoliths are very brittle, and a damaged sample would most likely not have survived the sample preparation procedures required for thermal diffusivity measurements. Second, the grain sizes in the samples from the two studies may be different. If the CVD SiC in [65] had a larger grain size, this may contribute to a higher thermal diffusivity. [38] Third, as reported in Carpenter [47], T-1 A was observed to have experienced weight gain. This weight gain may be attributed to the development of a silica (SiO_2)

[24] At an irradiation temperature of 300 °C, only interstitials and vacancy defects are generated.

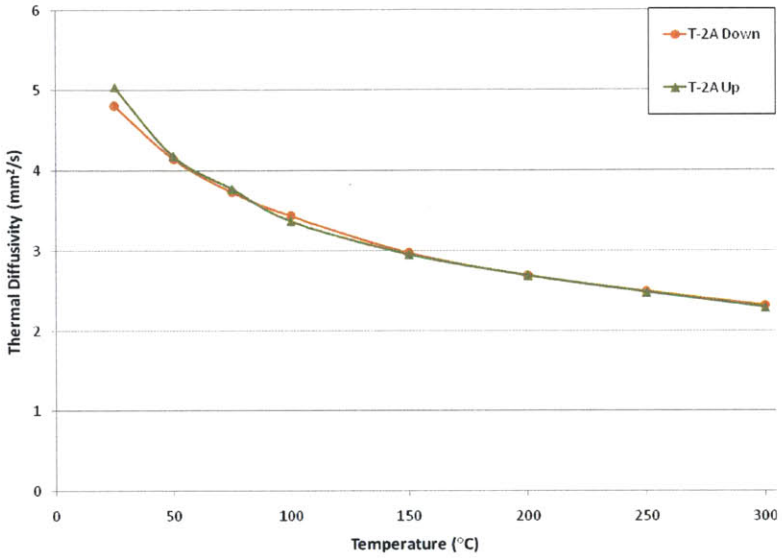

(a) Thermal diffusivity of monolithic SiC tube T-2A with curvature facing up and down.

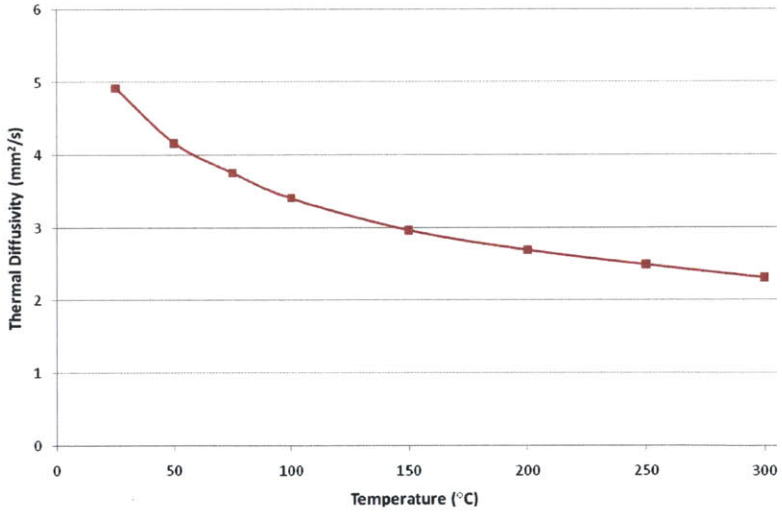

(b) Average of the up and down thermal diffusivity measurements for T-2.

Figure 5.15: Thermal diffusivity of monolith-only sample T-2.

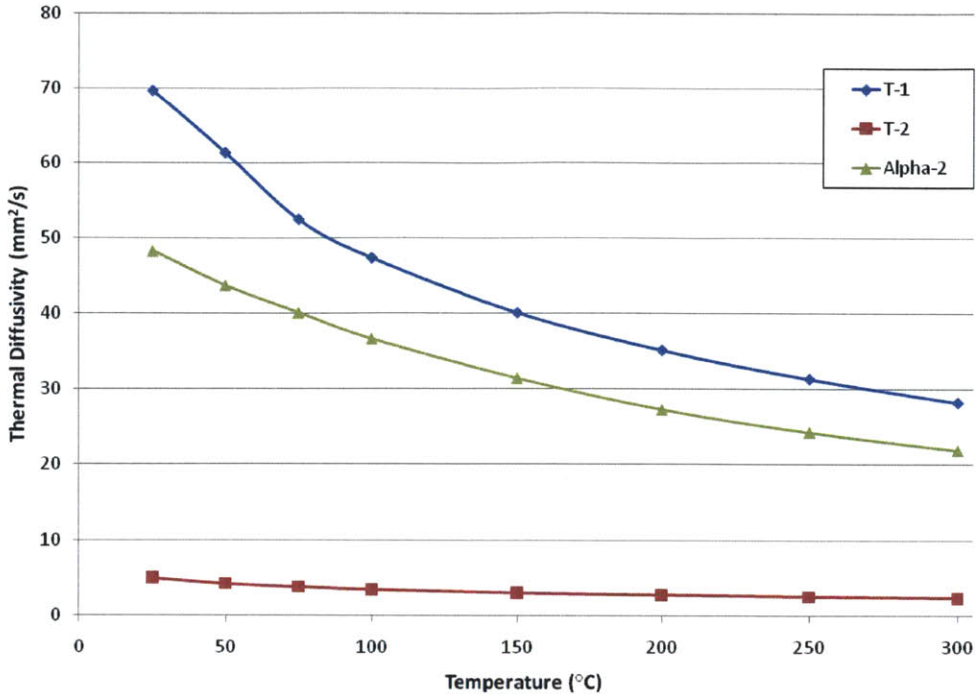

Figure 5.16: Average thermal diffusivity of irradiated monolithic SiC tube samples. T-1 A and Alpha-2 A were located in the ACI loop above the core and should have ~ 0 dpa. T-2 A was calculated to have 1.09 dpa.

layer. The passive corrosion of SiC produces this protective silica layer; however, silica has a low thermal diffusivity of 0.8 mm^2/s at 25 °C [83]. Henager *et. al.* saw significant silica formation on the surface of CVD SiC in water at 300 °C and 10 MPa. [69] The formation of a silica layer on all of the ACI samples is likely, and would reduce the apparent thermal diffusivity of SiC.[25] Finally, it is also possible that despite being located above the core, there was some non-negligible displacement damage in T-1 A. Little displacement damage is needed in order to see large reductions in thermal diffusivity. Again, using the work of Senor *et. al.* as an example, the thermal diffusivity of CVD SiC decreased from 123 mm^2/s at 0.0 dpa to 50 mm^2/s at 0.48 dpa. Even a fraction of a dpa could have reduced the thermal diffusivity of T-1 A. Future work must include measurements of the thermal diffusivity of samples before and after time spent in the ACI loop.

For another data comparison, Senor *et. al.* reported thermal diffusivities of 37 mm^2/s and 20 mm^2/s at measurement temperatures of 25 °C and 300 °C respectively for CVD SiC irradiated to 0.95 dpa at 1100 °C. [65] Sample T-2 A, irradiated at 300 °C to 1.09 dpa, has a thermal diffusivity of 5 mm^2/s and 2.25 mm^2/s at 25 °C and 300 °C respectively. The differences between Senor and co-workers' data and the data reported in this work are due to the higher irradiation temperature (1100 °C) used by Senor. The higher irradiation temperature allows for much higher rates of defect recombination since defects have greater mobility at elevated temperatures. Radiation damage is typically more severe at lower irradiation temperatures where radiation-induced defects do not have enough mobility to recombine. This effect is clearly seen in this comparison. Also, as mentioned in the above paragraph, the formation of a poor heat conducting silica layer on T-2 A is likely, and would adversely effect the thermal diffusivity compared

[25] See [47] for more information on corrosion of SiC tube samples.

to a sample which did not experience corrosion.

The comparison is much closer between the thermal diffusivity for sample T-2 A and the thermal diffusivity in a similar test from Hegeman *et. al.* [76]. In [76], CVD SiC irradiated at 600 °C to ~ 3.5 dpa was measured to have a thermal diffusivity of 5 mm^2/s at room temperature and at 300 °C. This is a more appropriate comparison because the 600 °C irradiation temperature is still within the regime where only point defects accumulate and a lower degree of defect annihilation occurs. This also provides further evidence that the thermal diffusivity in T-2 has been reduced to a saturation level where further dpa will not significantly effect the thermal diffusivity.

The difference between sample α-2 A (α-SiC) and T-1 A (β-SiC) is apparent in Figure 5.16. Senor *et. al.* have reported higher thermal diffusivities for (CVD) β-SiC than for (sintered Hexoloy SA) α-SiC: 123 mm^2/s *vs.* 70 mm^2/s at a temperature of 25 °C. Thus, this observation is not surprising because β-SiC deposited by CVD generally has greater purity than α-SiC which is usually manufactured using sintering aids.

Finally, compare the thermal diffusivity of the Trex monolith-only sample T-1 A (~ 0 dpa) to the thermal diffusivities of the un-irradiated Triplex samples from Section 5.4. The best Triplex sample (04-A in Figure 5.12) has a thermal diffusivity of 28.5 mm^2/s compared to 70 mm^2/s for T-1 A at 25 °C. This is a clear illustration of the effect of combining multiple grades of SiC into multiple layers in the Triplex samples. The phonons must traverse the three layers, and the interface between each layer will strongly scatter phonons. Additionally, the composite layer has many interfaces between the matrix and the fibers.

5.5.2 Thermal diffusivity of irradiated Triplex SiC

Two different irradiated Triplex SiC tubes were investigated. One sample was cut from Triplex tube 25-1, and two samples were cut from Triplex tube 26-2. The constructions and exposures of both tubes are identical: Trex monolith, Hi-Nicalon-S/CVI composite, HyperTherm CVI EBC; and 0.99 dpa. Figure 5.17 shows the thermal diffusivity *vs.* temperature curves for the three irradiated Triplex thermal diffusivity squares. Each curve is in good agreement with the others, and the measurements made with the curvature facing up are nearly equivalent to the measurements made with the curvature facing down. Only the curve for sample 26-2 B with the curvature facing up exhibits some unusual behavior. The measurements from 26-2 B "up" converge with those from the 26-2 B "down" measurements at 50, 75, 100, and 150 °C only to diverge at 200 and 250 °C before converging to the same value again at 300 °C. The pattern exhibited in all of the other thermal diffusivity *vs.* temperature curves thus far has been small deviations between up and down curves at temperatures lower than 100 °C with very close agreement above 100 °C. The deviations observed in Figure 5.17 (less than 0.25 mm^2/s) are small. Small deviations are not unusual and were averaged out.

The average curves are plotted in Figure 5.18 which shows a significant decrease in the thermal diffusivity of these irradiated Triplex samples compared to their un-irradiated counterparts. For ease of comparison, the thermal diffusivities of the four un-irradiated Triplex samples, the irradiated monolith, and the two irradiated Triplex samples are re-plotted together in Figure 5.19. The monolith thermal diffusivity (T-2) decreased by a factor of 14 compared to the above-core monolith sample (T-1) discussed above in Section 5.5.1. The Triplex thermal diffusivities decreased by a factor of between 7 and 9. A decrease in the temperature dependency of the thermal diffusivity is also apparent

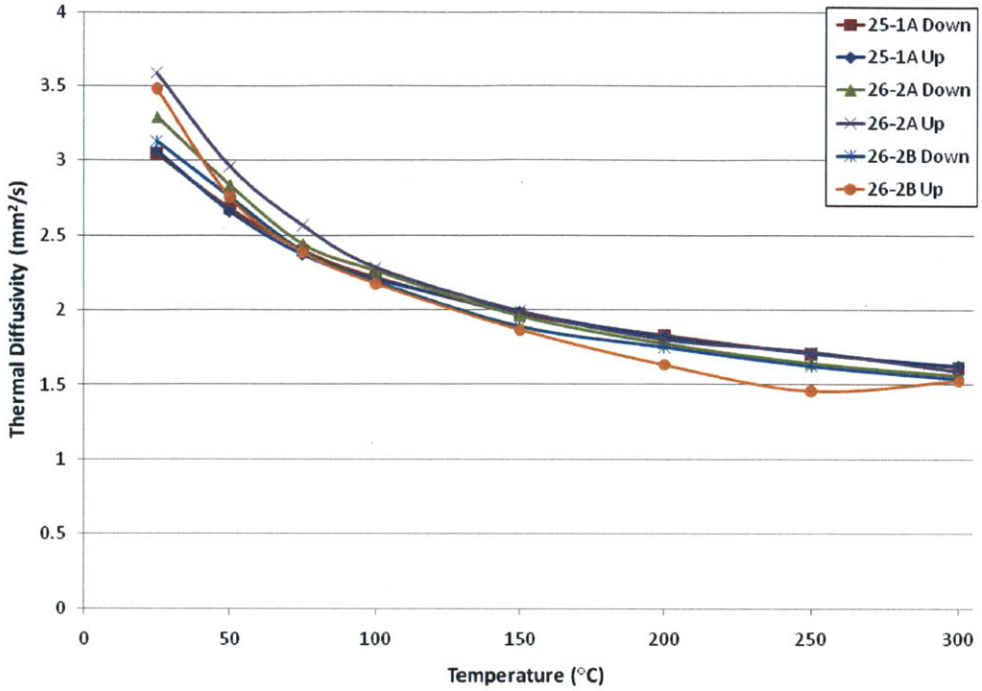

Figure 5.17: Thermal diffusivity *vs.* temperature curves measured for up and down facing irradiated Triplex samples. (0.99 dpa)

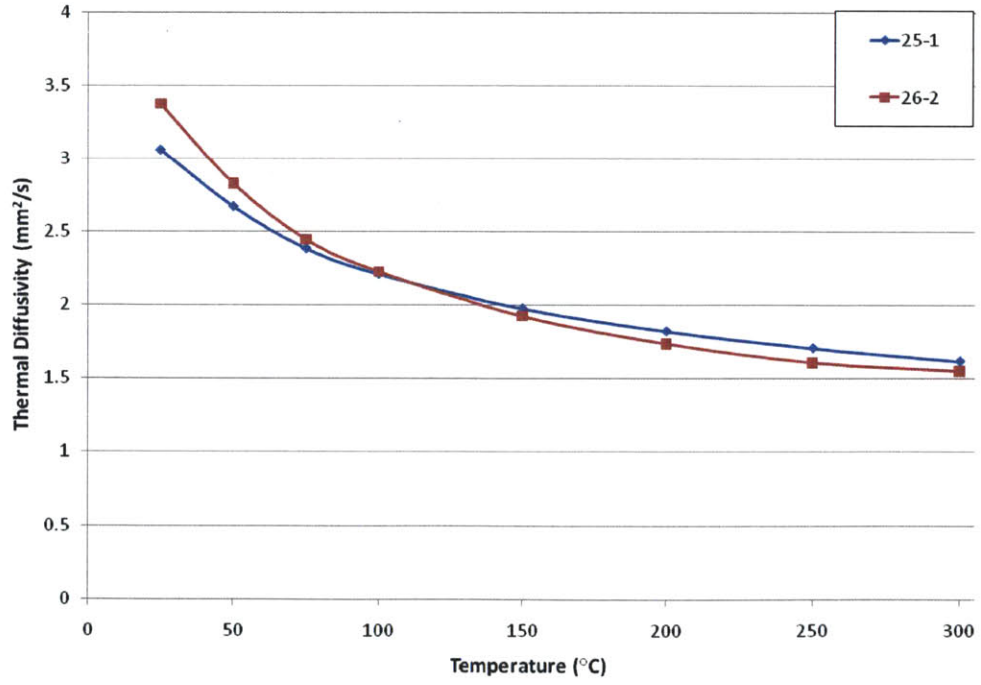

Figure 5.18: Average thermal diffusivity for Triplex tubes 25-1 and 26-2 each irradiated to 0.99 dpa in the ACI loop.

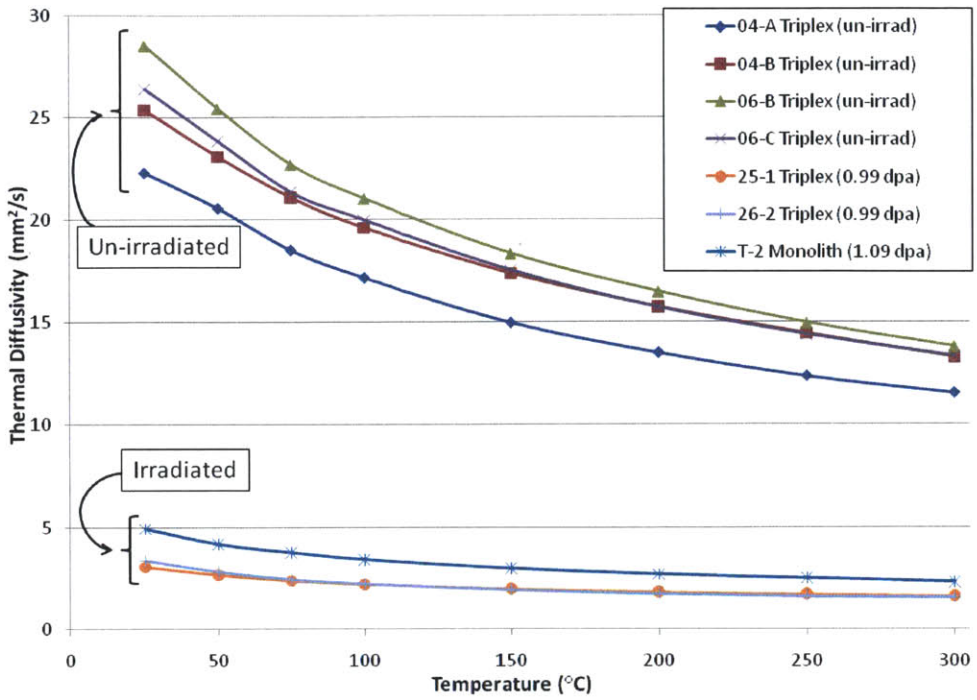

Figure 5.19: Comparison of the thermal diffusivities of irradiated and un-irradiated Triplex samples.

when comparing the irradiated curves to the un-irradiated curves. This is due to the accumulation of point defects to a concentration that phonon-defect scattering is equal to or greater than phonon-phonon scattering at all measurement temperatures.

It is somewhat surprising that the monolith-only SiC suffered a larger fractional decrease in thermal diffusivity than did the Triplex samples, since it is the Triplex samples which have more possible modes of degradation. Nevertheless, the degree of degradation in the thermal diffusivity of the monolithic CVD SiC sample (T-2) is supported by reference to the literature. Hegeman and co-workers reported a decrease in the thermal diffusivity of CVD SiC by roughly a factor of 15. [76] This work observed a factor of 14 decrease in the thermal diffusivity of the monolith-only samples. The Hegeman group also report a factor of 7 or 8 decrease in the thermal diffusivity of composite SiC (Hi-Nicalon fibers in a CVI SiC matrix) after irradiation at 600 °C to 3.5 dpa. This work reports a thermal diffusivity decrease for the Triplex samples of a factor of between 7 and 9. The behavior of the samples in this work is similar to that published by Hegeman *et. al.* [76]

Many of the degradation modes discussed to help explain the degradation of the mechanical properties measured during the hoop testing of irradiated Triplex samples (Section 3.3.3) are applicable to this discussion as well. As was mentioned previously, thermal conduction through SiC is by phonon transport and any defects (point defects, grain boundaries, material interfaces) which scatter phonons will reduce the thermal diffusivity. In addition to the accumulation of point defects in the SiC lattice under neutron irradiation, the Triplex samples possess a number of material interfaces (monolith/composite, fiber/matrix, and composite/EBC interfaces) which will act as phonon scattering centers. [80] If these interfaces are disturbed, the thermal diffusivity will suffer.

The HNTS fibers have a larger CTE than the higher purity CVI matrix. It is unclear whether this differential expansion would be beneficial or detrimental to the thermal diffusivity. On one hand, if the HNTS fibers expanded more than the matrix, this might improve the contact between the fibers and the matrix, thus improving the thermal diffusivity. On the other hand, this mismatch in the thermal expansion coefficients of the Hi-Nicalon Type S fibers and the CVI SiC matrix might introduce residual stresses at the fiber/matrix interface. [56] When these residual stresses relax, perhaps by slippage of the fibers within the matrix, the fiber/matrix interface could be disturbed. Differential irradiation induced swelling is not expected to occur. Nozawa *et. al.* [56] and Hinoki *et. al.* [84] found the swelling behavior of HNTS fibers to be comparable to the CVI β-SiC matrix material, even to 10 dpa. Since the thermal diffusivities of the irradiated monolith-only tubes and Triplex tubes have converged from a pre-irradiation difference of 41.5 mm^2/s (at 25 °C) to a post irradiation difference of less than 1 mm^2/s, it seems reasonable to conclude that the primary mode of thermal diffusivity degradation in both Triplex and monolithic SiC tubes irradiated in the ACI is due to radiation induced point defects and the formation of a poorly conducting silica layer due to corrosion with water at 300 °C and 10.5 MPa.

The LFA 447 is only able to measure thermal diffusivities from room temperature up to 300 °C. PWRs may have core outlet temperatures exceeding 300 °C during normal operation. Under accident scenarios, the temperatures may be expected to reach several times the normal operating temperature. It is seems reasonable to extrapolate the thermal diffusivity data presented here to temperatures of 350-400 °C. Due to the low slopes of the thermal diffusivity curves for the irradiated samples, extrapolation to temperatures beyond 400 °C should be reasonable as well. If experimental data are desired for measurement temperatures above 300 °C, an upgrade from the xenon-flash instrument to the more costly laser-flash system will be required.

As the current standard in PWR fuel cladding, a comparison to Zircaloy is appropriate. The thermal diffusivity for the samples irradiated in this work were converted to thermal conductivity for direct comparison with published thermal conductivity data for Zircaloy. For the monolith-only sample T-2, the density was taken to be 100 % of the theoretical density of 3.21 g/cm^3. For the Triplex samples, 25-1 and 26-2, it was assumed that the composite layer had 10 % porosity. Since the composite layer accounts for roughly half the thickness of the Triplex tube, the density of the Triplex sample as a whole was taken to be 95 % of theoretical density: 3.05 g/cm^3. The specific heat at the test temperatures for the monolithic β-SiC was taken from the Thermophysical Properties of Materials Database. [85] In the literature, there is a scarcity of specific heat data for composite SiC, and many authors have used the heat capacity of monolithic SiC when calculating the thermal conductivity for composite SiC. In this work, specific heat data for composite SiC (Hi-Nicalon fibers in a CVI SiC matrix) from Jones *et. al.* were used to estimate the specific heat for the composite layer of the Triplex samples. [86] In order to arrive at a specific heat for the Triplex sample as a whole, the data from the Thermophysical Properties of Matter Database were averaged with an interpolation of the data from Jones and co-workers. With the estimated density, an estimated specific heat, and the measured thermal diffusivity, the thermal conductivity was calculated according to Equation 2. The calculated values are expected to be somewhat conservative given that Reference [86] published only two c_p *vs.* Temperature data points. Thermal conductivities for as-fabricated Zircaloy-4 were found in the MATPRO manual. [87] Comparing irradiated SiC to un-irradiated Zircaloy

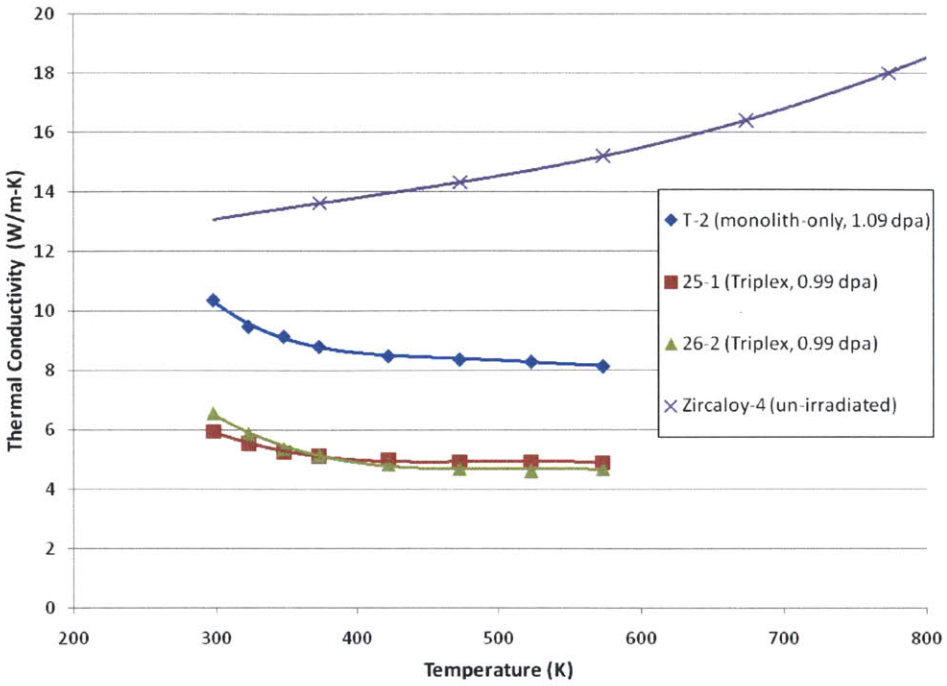

Figure 5.20: Thermal conductivity of monolith-only and Triplex SiC *vs.* Zircaloy-4.

is valid since heat conduction in Zircaloy is primarily by electrons, and the thermal conductivity is minimally affected by dislocation damage.

On average, un-irradiated Triplex samples have a thermal conductivity of 49 W/m-K and 40 W/m-K at 300 K and 573 K respectively. This is far superior to as-fabricated Zircaloy-4. However, SiC's advantage is reduced with irradiation. As depicted in Figure 5.20, the thermal conductivity of Zircaloy-4 is greater than that for the irradiated monolith-only sample T-2 by roughly 2.5 W/m-K and 7 W/m-K at 300 K and 573 K respectively. The irradiated Triplex samples have thermal conductivities lower than Zircaloy-4 by roughly 7 W/m-K and 10 W/m-K at 300 K and 573 K respectively. Effective heat transfer utilizing a SiC cladding type may require a different type of fuel pin such as the annular design featuring cooled inner and outer radii discussed by Carpenter [45, 47]. The thermal conductivity of Zircaloy will decrease with oxidation. Gilchrist reports that the black zirconium oxide which forms on Zircaloy cladding may have a thermal conducitivity as low as 0.13 - 0.86 W/m-K. [88] SiC's corrosion resistance may allow it to have more consistent heat transfer over its service life than Zircaloy. It is possible that SiC's thermal conductivity may overtake that of Zircaloy at some point during the service life.

6 Summary, Conclusions, and Suggested Future Work

A tubular silicon carbide fuel cladding has been proposed as a replacement for the tubular Zircaloy claddings currently used in LWRs. The proposed design, referred to as a Triplex SiC cladding, consists of three layers of SiC. The inner layer is monolithic CVD SiC from which the Triplex tube derives the majority of its strength. The central layer surrounds the monolith and is a composite made of Hi-Nicalon Type S SiC fibers and a SiC matrix deposited within the fiber preform via CVI. The composite layer provides additional strength and pseudo ductility such that the Triplex design exhibits a "graceful" failure mode not possible with only monolithic SiC. The outermost layer is a thin environmental barrier coating applied via CVD, which acts to protect against corrosion.

Silicon carbide's high melting point, high hardness, relatively high thermal conductivity, low neutron cross section, low chemical reactivity, and low thermal expansion coefficient make it a good candidate for a fuel cladding. A SiC cladding may allow increased safety margins under transients and accident scenarios (LOCA, RIA, etc), improved resource utilization via a higher allowable burnup beyond the NRC mandated 62 GWd/MTU limit, and improved waste management.

The work presented here evaluated the Triplex cladding prototypes as well as methods for bonding SiC to SiC. The hoop strength of both irradiated and un-irradiated Triplex claddings was measured. SEM was used to assess the fracture mechanisms at work in the failure of the Triplex samples. Three SiC/SiC bonding methods were evaluated in the ACI loop. Visual inspection, SEM/EDX, and swelling data were collected to help characterize these bond specimens and propose reasons for their failure. Finally, the thermal diffusivities of irradiated and un-irradiated Triplex samples and monolith-only samples were measured and compared.

6.1 Summary and Conclusion of Mechanical Testing

Two Triplex samples, one irradiated and one un-irradiated, were tested using an expanding plug apparatus which pressurized the interior of the tubes until their failure. From this test, the hoop strength and internal pressure at failure were calculated assuming that the point of maximum stress occurs on the inner surface of the monolith. It was argued that this assumption was valid because the tube's thickness is comparable to its radius such that the thin shell approximation does not hold and that the dimpled inner surface acted to concentrate stresses.

It was found that the sample (25-2) irradiated to 0.99 dpa failed at a hoop stress of 103 MPa and an internal pressure of 20.4 MPa. The un-irradiated sample (06-B) failed at a higher hoop stress of 169 MPa and an internal pressure of 30.5 MPa. Both of these samples failed at lower stresses and internal pressures than did the un-irradiated samples of the same construction tested by Carpenter. The average internal pressures and hoop stresses at failure from Carpenter's work are 255.6 MPa and 46.5 MPa respectively. Sample 06-B possessed a radially varying wall thickness (i.e. thicker on one side than on the other) due to a manufacturing fault. This is undoubtedly responsible for its lower hoop stress at failure compared to tubes of the same construction tested by Carpenter. It is not surprising that the un-irradiated sample, 25-2, ruptured at a lower hoop stress than its un-irradiated counterparts. The same effect has been noted in tests by Carpenter [47] and Feinroth *et. al.* [46].

Compared to Zircaloy at room temperature, the Triplex samples tested here were not as promising as the Triplex designs tested by Carpenter [47]. At elevated temperatures, however, the hoop strengths of the Triplex SiC designs tested here would maintain their strengths while Zircaloy's strength quickly decreases with increasing temperature.

A number of explanations for this strength reduction in Triplex SiC samples with irradiation in the ACI loop are feasible, but the most compelling are as follows. First, some degradation in the mechanical properties was likely caused by greater thermal expansion in the HNTS fibers than in the matrix. Second, although both the HNTS and CVI matrix SiC materials are high in purity, the fibers and the matrix may have accumulated point defects at different rates and experienced differential radiation induced swelling. Both differential thermal expansion and differential swelling would have generated localized stresses and may have cause fiber/matrix debonding. Third, since some of the load during internal pressurization of the Triplex sample is shared among all three layers, if the inter-layer bonding was disturbed, this would reduce the hoop strength. The monolith is likely to have a lower radiation-induced swelling rate and a different thermal expansion rate than the composite layer. Fourth, corrosion pitting of the inner surface of the monolith will have concentrated stresses in the Triplex tube's most vulnerable area. Finally, displacement damage in SiC irradiated at 300 °C introduces point defect flaws into the crystal structure which concentrate and amplify stresses.

Visual analysis and SEM micrographs allowed the characterization of crack propagation in the Triplex tubes after hoop testing. The crack initiates at the monolith inner surface where it breaks through the monolith perpendicular to its surface. The crack enters the composite where it propagates laterally by debonding the fibers from the matrix. All the while, energy is dissipated in the composite as the crack propagates. Eventually the crack is either arrested in the matrix or traverses radially by causing debonding between the composite and the outer EBC where it eventually breaks through the outer surface. The composite layer, particularly the fiber/matrix interface and the composite/EBC interface, is the key component for dissipating fracture energy, helping to slow crack propagation, and providing a graceful failure for the Triplex tube.

6.2 Summary and Conclusion of Bond-Block Irradiation and Analysis

Since the proposed SiC fuel cladding must be sealed once the UO_2 fuel pellets have been loaded, three methods for bonding SiC to SiC were evaluated. Six samples (two of each bond type), each comprised of two Hexoloy SA (α-SiC) blocks bonded together, were irradiated in the ACI loop for 1.5 months to a fluence equivalent to 0.16 dpa. Of the six samples, only one remained bonded after the 1.5 month period. The five failed samples went on to PIE which included SEM of the failed bond surfaces, weight loss analysis, and swelling measurements.

The "glass ceramic" calcium aluminate ($CaO\text{-}Al_2O_3$) bond material failed in two samples. Visual inspection raises questions as to whether the bond material actually covered the entire bonded face at fabrication, as only a small area of bond material remained. SEM discovered rhombohedral crystals containing Al, Ca, and O surrounding a large amorphous region of the remaining bond material. Glass ceramics such as calcium aluminate have better mechanical properties in the amorphous state. Radiation induced ordering may have caused formation of the crystals from the amorphous material. If the calcium aluminate was not quenched fast enough during manufacturing, this may also have allowed the formation of undesirable crystals with degraded mechanical properties which contributed to the failure of

this bond method.

The titanium foil bond method also failed in two specimens. SEM showed that the remaining bond material was not uniformly spread over the bonded face of the Hexoloy SA substrate. Nano-scale Ti crystals were discovered in branch-like patterns in the bond material. The CTE for Ti is twice the CTE for α-SiC and this effect may have generated shear stresses on the bonds.

One of the samples bonded with the TiC/SiC bond method survived and was returned to the ACI loop. The other failed and was inspected. This bond material is notable as the thickest remaining bond material observed. It also possessed high porosity. Small aluminum needle-like crystals were formed in the immediate vicinity of areas which suffered bond material/substrate debonding. The primary bond material, Ti, has a much higher strength than Al. It is possible that the presence of these Al impurities acted to nucleate cracks and promote debonding between the bond material and the SiC substrate.

Minor weight loss was observed in all of the bond specimens after irradiation. Each pair of samples bonded by the same method experienced nearly identical weight loss. Thus, the weight loss was attributed to the loss of bond material once the bond itself had broken.

Dimensional changes suggested that each sample had experienced swelling; however, the dimensional changes were highly anisotropic. Density measurements confirmed that the α-SiC blocks had each experienced 1.7 % swelling. The density before irradiation was 3.14 g/cm^3 and the density after irradiation was 3.09 g/cm^3. This swelling is attributed to neutron capture (n,α) reactions with the ^{10}B sintering aid used in Hexoloy SA which would have caused helium nucleation at the grain boundaries. Point defect accumulation is also a significant contributor to this swelling. Due to the anisotropic swelling, it is likely that shear stresses contributed to the failure of the bond specimens.

6.3 Summary and Conclusion of Thermal Diffusivity Measurements

Both un-irradiated and irradiated Triplex tubes along with irradiated and un-irradiated monolith-only tubes were fashioned into ~ 6 mm x 6 mm squares for thermal diffusivity measurements made via the widely-used thermal-flash method. A methodology was devised which allowed the fabrication of thermal diffusivity samples from the often brittle, radioactive SiC tubes exposed in the ACI experiment. For each sample, the thermal diffusivity was measured over a range of temperatures from 25 °C to 300 °C.

Since each sample was cut from an originally tubular specimen, each sample had curvature with a radius of approximately 5 mm. Since the thermal-flash measurement method was intended only for samples having two flat, parallel-plane surfaces, the effect of the curvature on the thermal diffusivity readings was investigated by making measurements with the curvature facing up and down. The data demonstrated virtually equivalent diffusivity between the up and down measurements. These were averaged in order to arrive at a final thermal diffusivity for the specimen.

The un-irradiated Triplex samples have thermal diffusivities between 20 and 28.5 mm^2/s at 25 °C, and between 10 and 16 mm^2/s at 300 °C. The un-irradiated CVD monolith returned a thermal diffusivity of 70 mm^2/s at 25 °C and 28 mm^2/s at 300 °C. The difference is down to the numerous interfaces between the monolith and the composite, and the fibers and the matrix, and the composite and the EBC. Each material interface represents a strong phonon scattering

center which degrades the thermal conductivity of the Triplex SiC samples compared to the monolith-only sample.

The Triplex samples irradiated to 0.99 dpa returned thermal diffusivities of 3.4 mm^2/s at 25 °C and 1.6 mm^2/s at 300 °C. This is a substantial reduction due to the accumulation of point defects which strongly scatter phonons. The temperature dependence of the thermal diffusivity *vs.* temperature plots was reduced as phonon-defect scattering meets or exceeds phonon-phonon scattering. The irradiated CVD monolith also returned significantly degraded thermal diffusivities of 4.9 mm^2/s at 25 °C and 2.3 mm^2/s at 300 °C. This type of reduction is reasonable given comparisons to the literature. Since the thermal diffusivities of the irradiated Triplex and monolith-only samples have approached such similar values, this suggests that the same mechanisms are at play: the accumulation of phonon scattering defects and the formation of a low-conducting silica layer due to corrosion. Comparison to the literature suggests that both the irradiated monolith-only and Triplex samples have reached their saturation thermal diffusivities.

As-fabricated Zircaloy-4 cladding has been reported with thermal conductivities of 13 W/m-K at 25 °C and 15 W/m-K at 300 °C. The un-irradiated Triplex samples look very good by comparison. However, the irradiated monolithic and Triplex samples cannot match Zircaloy's thermal conductivity/diffusivity which increases with temperature and is not expected to suffer significant degradation with irradiation, because heat conduction in Zircaloy is mostly by electrons and not by the phonons (lattice waves) that dominate heat conduction in SiC. It is, however, possible that SiC's superior corrosion resistance will allow it to provide more consistent heat transfer over the course of its in-core service life.

6.4 Suggested Future Work

Regarding the mechanical testing, more test samples of the same construction are needed in order to give statistical significance to the hoop strengths of irradiated and un-irradiated Triplex tubes. Manufacturing flaws (e.g. uneven tube wall thickness) compromised the hoop strength of one of the un-irradiated Triplex tubes. Similar flaws may not have been noticed in other samples. A higher degree of manufacturing consistency will be needed for mass production of a composite SiC cladding. It would be informative to understand how the strength of the SiC cladding evolves with temperature. Thus, hoop tests at PWR operating temperatures and at postulated accident temperatures are needed. Proving the strength of SiC at high temperatures and comparing it to Zircaloy is important. More attention should also be paid to the corrosive pitting of the monolith which may have contributed to the reduction in hoop strength following a specimen's exposure in the ACI loop.

The SiC/SiC bonding methods require a new approach. The boron sintered α-SiC used to test the bonds experienced anisotropic swelling which undoubtedly stressed the bonds. In future tests, it would be worth using a highly pure, highly stoichiometric CVD β-SiC product which would have improved dimensional stability. Different bond methods must also be tried, and mechanical testing of a set of un-irradiated bond samples would be valuable. The use of in-core LVDTs would allow the collection of real-time swelling data and might help to determine if/when bond samples fail while in the ACI loop. As the bond material should ideally have the same properties as the rest of the SiC cladding, a method for using CVD or CVI SiC to seal the tubes after the fuel has been loaded would be ideal. The SiC cladding will only be as good as its weakest link.

The thermal diffusivities of more samples of different constructions and exposures should be measured. This would help to build a map of the evolution of thermal diffusivity of SiC with dose and to help explain the relative behavior of the monolith and the composite portions of the Triplex design.

References

[1] Duderstadt, J. J., and Hamilton, L. J. *Nuclear Reactor Analysis*, 1st ed.; Wiley, 1976.

[2] Butler, D. (2004) Energy: Nuclear power's new dawn. *Nature 429*, 238–240.

[3] Todreas, N. E., and Kazimi, M. S. *Nuclear Systems Volume I: Thermal Hydraulic Fundamentals, 1st edition*; Taylor & Francis, 1989.

[4] Marshall, A. C. *An Assessment of Reactor Types for Thermochemical Hydrogen Production - SAND2002-0513*; Sandia National Laboratory, 2002.

[5] Barrow, H., and Hassan, A. (1984) Azimuthal temperature variation in the cladding of PWR fuel elements. *Nuclear Engineering and Design 77*, 97–102.

[6] Collier, J. G., and Hewitt, G. F. *Introduction to Nuclear Power*; Hemisphere Publishing: Washington, D. C., 1987.

[7] Cacuci, D. G. *Handbook of Nuclear Engineering*, 1st ed.; Springer, 2010; pp 1522–1620, Ch. 13.

[8] Marchal, N., Campos, C., and Garnier, C. (2009) Finite element simulation of Pellet-Cladding Interaction (PCI) in nuclear fuel rods. *Computational Materials Science 45*, 821–826.

[9] Michel, B., Sercombe, J., and Thouvenin, G. (2008) A new phenomenological criterion for pellet-cladding interaction rupture. *Nuclear Engineering and Design 238*, 1612–1628.

[10] Was, G. *Fundamentals of Radiation Material Scence*; Springer: New York, 2007.

[11] Rahn, F. J., Adamantiades, A. G., Kenton, J. E., and Braun, C. *A Guide to Nuclear Power Technology: A Resource for Decision Making*; John Wiley & Sons, 1984.

[12] Glasstone, S., and Sesonske, A. *Nuclear Reactor Engineering*, 3rd ed.; Van Nostrand Reinhold Inc.,U.S., 1981.

[13] Simnad, M. T. (1981) A brief history of power reactor fuels. *Journal of Nuclear Materials 100*, 93–107.

[14] Pickman, D. (1972) Properties of zircaloy cladding. *Nuclear Engineering and Design 21*, 212–236.

[15] Cox, B. (1990) Environmentally-induced cracking of zirconium alloys – A review. *Journal of Nuclear Materials 170*, 1–23.

[16] Simpson, C., and Ells, C. (1974) Delayed hydrogen embrittlement in Zr-2.5 wt % Nb. *Journal of Nuclear Materials 52*, 289–295.

[17] *Current Trends in Nuclear Fuel For Power Reactors*; 51st IAEA General Conference (2007); IAEA: Vienna Austria, 2007.

[18] *A Technology Roadmap for Generation IV Nuclear Energy Systems: Ten Nations Preparing Today for Tomorrow's Energy Needs*; GIF-002-00; United States Department of Energy, 2002.

[19] *Program on Technology Innovation: Advanced Fuel Cycles - Impact on High-Level Waste Disposal: Analysis of Deployment Scenarios of Fast Burner Reactors in the U.S. Nuclear Fleet*; EPRI: Palo Alto, CA, 2008.

[20] Ilas, G., Gauld, I. C., and Murphy, B. D. *Analysis of Experimental Data for High Burnup PWR Spent Fuel Isotopic Validation - ARIANE and REBUS Programs (UO2 Fuel)*; United States Nuclear Regulatory Commission, 2010.

[21] *Extended Burnup Evaluation - Topical Report BAW-10186-A, Rev. 1*; United States Nuclear Regulatory Commission: Washington, D. C., 2000; Web-based ADAMS search.

[22] Yang, R., Cheng, B., Deshon, J., Edsinger, K., and Ozer, O. (2006) Fuel R & D to Improve Fuel Reliability. *Journal of Nuclear Science and Technology 43*, 951–959.

[23] Carpenter, D., Kohse, G., and Kazimi, M. Modeling of Silicon Carbide Duplex Cladding Designs for High Burnup Light Water Reactor Fuel. 2008.

[24] Staehle, R. W., Eyre, B. L., and Kimura, I. *Research for Aging Management of Light Water Reactors and Its Future Trend*; Anatomy of Proactivity; Institute of Nuclear Safety Systems, Inc., 2008.

[25] Motta, A. T. *Light-Water Reactor Fuel Degradation Mechanisms at High Burnup: Implications to Generation IV Materials*; Materials Research Society Symposium Proceedings; MRS Online Proceedings Library, 2007; Vol. 1043.

[26] Pierron, O. N., Koss, D. A., Motta, A. T., and Chan, K. S. (2003) The influence of hydride blisters on the fracture of Zircaloy-4. *Journal of Nuclear Materials 322*, 21–35.

[27] Diamond, D. J., Hsu, C., Fitzpatrick, R., and Mirkovic, D. *Reactivity Accidents: A reassessment of the design basis events-BNL-NUREG-43069*; Conference: 17 Water Reactor Safety Information Meeting, October 23-25, Rockville, MD; 1989.

[28] Nero, A. V. *A Guidebook to Nuclear Reactors*; University of California Press, 1979.

[29] Hannerz, K., and Vesterlund, G. (1975) Zircaloy cladding mechanical properties. *Nuclear Engineering and Design 33*, 205–218.

[30] Shiozawa, S., Ichikawa, M., and Fujishiro, T. (1988) Studies of the UO2-zircaloy chemical interaction and fuel rod relocation modes in a severe fuel damage accident. *Journal of Nuclear Materials 154*, 116–122.

[31] Hofmann, P., and Kerwin-Peck, D. (1984) UO2/Zircaloy-4 chemical interactions from 1000 to 1700°C under isothermal and transient temperature conditions. *Journal of Nuclear Materials 124*, 80–105.

[32] Saux, M. L., Besson, J., Carassou, S., Poussard, C., and Averty, X. (2010) Behavior and failure of uniformly hydrided Zircaloy-4 fuel claddings between 25 °C and 480 °C under various stress states, including RIA loading conditions. *Engineering Failure Analysis 17*, 683–700.

[33] *50.46 Acceptance criteria for emergency core cooling systems for light-water nuclear power reactors*; United States Nuclear Regulatory Commission: Washington, D. C., 2011.

[34] Heinisch, H., Greenwood, L., Weber, W., and Williford, R. (2002) Displacement damage cross sections for neutron-irradiated silicon carbide. *Journal of Nuclear Materials 307-311*, 895–899.

[35] Alkan, Z., Kugeler, K., Kaulbarsch, R., and Manter, C. (2001) Silicon carbide encapsulated fuel pellets for light water reactors. *Progress in Nuclear Energy 38*, 411–414.

[36] Katoh, Y., Snead, L. L., Nozawa, T., Morley, N. B., and Windes, W. E. (2006) Advanced Radiation-Resistant Ceramic Composites. *Advances in Science and Technology 45*, 1915–1924.

[37] Riley, F. *Structural Ceramics*; Cambridge University Press: New York, 2009.

[38] Snead, L. L., Nozawa, T., Katoh, Y., Byun, T., Kondo, S., and Petti, D. A. (2007) Handbook of SiC properties for fuel performance modeling. *Journal of Nuclear Materials 371*, 329–377.

[39] Daulton, T. L., Bernatowicz, T. J., Lewis, R. S., Messenger, S., Stadermann, F. J., and Amari, S. (2003) Polytype distribution of circumstellar silicon carbide: microstructural characterization by transmission electron microscopy. *Geochimica et Cosmochimica Acta 67*, 4743–4767.

[40] Wright, W. V., and Bartels, F. T. *Proceedings of the Conference for Silicon Carbide High Temperature Semiconductors 1960*; pp 31–36, Adapted by: ASM Alloy Phase Diagrams Center.

[41] Callister, W. D. *Material Science and Engineering: An Introduction*; John Wiley & Sons, Inc.,, 1985.

[42] Snead, L. L. (2004) Limits on irradiation-induced thermal conductivity and electrical resistivity in silicon carbide materials. *Journal of Nuclear Materials 329-333*, 524–529.

[43] Youngblood, G. E., Senor, D. J., and Jones, R. H. (2003) Thermal Diffusivity/Conductivity of Irradiated Monolithic CVD-SiC. *Fusion Materials Semiannual Progress Report for the Period Ending December 31, 2002: DOE-ER-0313/33* 27–33.

[44] Price, R. (1973) Thermal conductivity of neutron-irradiated pyrolytic [beta]-silicon carbide. *Journal of Nuclear Materials 46*, 268–272.

[45] Carpenter, D. Assessment of Innovative Fuel Designs for High Performance Light Water Reactors. Masters Thesis, Massachusetts Institute of Technology, 2006.

[46] Feinroth, H., Ales, M., Barringer, E., Kohse, G., Carpenter, D., and Jaramillo, R. In *Ceramics in Nuclear Applications: Ceramic Engineering and Science Proceedings*; Katoh, Y., and Cozzi, A., Eds.; 2009; Vol. 30; Issue 10; pp 47–55.

[47] Carpenter, D. An Assessment of Silicon Carbide as a Cladding Material for Light Water Reactors. Doctor of Philosophy Thesis, Massachusetts Institute of Technology, 2010.

[48] Acheson, E. G. United States Patent No. 492767: Production of Artificial Crystalline Carbonaceous Materials. 1893.

[49] Trex, *Trex Advanced Materials: Maker of Chemical Vapor Composite Silicon Carbide (CVC SiC)*; www.trexadvancedmaterials.com/trex.pdf.

[50] Katoh, Y., Nozawa, T., and Snead, L. L. (2005) Mechanical Properties of Thin Pyrolitic Carbon Interphase SiC-Matrix Composites Reinforced with Near-Stoichiometric SiC Fibers. *Journal of the American Ceramic Society 88*, 3088–3095.

[51] Bunsell, A. R., and Piant, A. (2006) A review of the development of three generations of small diameter silicon carbide fibres. *Journal of Materials Science 41*, 823–839.

[52] Takeda, M., Urano, A., ichi Sakamoto, J., and Imai, Y. (1998) Microstructure and oxidative degradation behavior of silicon carbide fiber Hi-Nicalon type S. *Journal of Nuclear Materials 258-263*, 1594–1599.

[53] Hinoki, T., Snead, L., Katoh, Y., Hasegawa, A., Nozawa, T., and Kohyama, A. (2002) The effect of high dose/high temperature irradiation on high purity fibers and their silicon carbide composites. *Journal of Nuclear Materials 307-311*, 1157–1162.

[54] Buschow, K. J., Cahn, R. W., Flemings, M. C., Ilschner, B., Kramer, E. J., and Mahajan, S. *Encyclopedia of Materials - Science and Technology*; Elsevier: New York, 2001; Vol. 2.

[55] Hollenberg, G. W., Henager, C. H., Youngblood, G. E., Trimble, D. J., Simonson, S. A., Newsome, G. A., and Lewis, E. (1995) The effect of irradiation on the stability and properties of monolithic silicon carbide and SiCf/SiC composites up to 25 dpa. *Journal of Nuclear Materials 219*, 70–86.

[56] Nozawa, T., Katoh, Y., and Snead, L. (2009) The effect of neutron irradiation on the fiber/matrix interphase of silicon carbide composites. *Journal of Nuclear Materials 384*, 195–211.

[57] Hong, S., Byun, T., Lowden, R. A., Snead, L. L., and Katoh, Y. (2007) Evaluation of the Fracture Strength for Silicon Carbide Layers in the Tri-Isotropic-Coated Fuel Particle. *Journal of the American Ceramic Society 90*, 184–191.

[58] Barringer, E. *CTP Monthly Status Report for February 2007*; CTP-07-003, 2007.

[59] Shinavski, R. J., Engel, T. Z., Wang, K. C., Magaldi, T., Lara-Curzio, E., Porter, W. D., Radovic, M., and Wang, H. *Mechanical and Thermal Evaluation of Near-Stoichiometric SiC Fiber-Reinforced SiC with Braided Architectures for Nuclear Applications*; 31st International Conference on Advanced Ceramics & Composites; 2007.

[60] Byun, T., Lara-Curzio, E., Lowden, R., Snead, L., and Katoh, Y. (2007) Miniaturized fracture stress tests for thin-walled tubular SiC specimens. *Journal of Nuclear Materials 367-370*, 653–658.

[61] Ross, D. F., and Hendrich, W. R. In *Ceramics in Nuclear and Alternative Energy Applications*; Marra, S., Ed.; Wiley, 2007; pp 117–125.

[62] Matthews, R. (1974) Irradiation damage in reaction-bonded silicon carbide. *Journal of Nuclear Materials 51*, 203–208.

[63] Snead, L., Osborne, M., and More, K. (1995) Effects of Radiation on SiC-Based Nicalon Fibers. *Journal of Materials Research 10*, 736–747.

[64] Huang, H., and Ghoniem, N. (1997) A swelling model for stoichiometric SiC at temperatures below 1000°C under neutron irradiation. *Journal of Nuclear Materials 250*, 192–199.

[65] Senor, D. J., Youngblood, G. E., Greenwood, L. R., Archer, D. V., Alexander, D. L., Chen, M. C., and Newsome, G. A. (2003) Defect structure and evolution in silicon carbide irradiated to 1 dpa-SiC at 1100 °C. *Journal of Nuclear Materials 317*, 145–159.

[66] Katoh, Y., Hashimoto, N., Kondo, S., Snead, L., and Kohyama, A. (2006) Microstructural development in cubic silicon carbide during irradiation at elevated temperatures. *Journal of Nuclear Materials 351*, 228–240.

[67] Dienst, W. (1992) Reduction of the mechanical strength of Al2O3, AlN and SiC under neutron irradiation. *Journal of Nuclear Materials 191-194*, 555–559.

[68] Dienst, W. (1994) Mechanical properties of neutron-irradiated ceramic materials. *Journal of Nuclear Materials 211*, 186–193.

[69] Jr., C. H. H., Schemer-Kohrn, A. L., Pitman, S. G., Senor, D. J., Geelhood, K. J., and Painter, C. L. (2008) Pitting corrosion in CVD SiC at 300 °C in deoxygenated high-purity water. *Journal of Nuclear Materials 378*, 9–16.

[70] Howe, L., and Thomas, W. (1960) The effect of neutron irradiation on the tensile properties of zircaloy-2. *Journal of Nuclear Materials 2*, 248–260.

[71] Hannon, A. C., and Parker, J. M. (2000) The structure of aluminate glasses by neutron diffraction. *Journal of Non-Crystalline Solids 274*, 102–109.

[72] Li, W., and Mitchell, B. S. (1999) Nucleation and crystallization in calcium aluminate glasses. *Journal of Non-Crystalline Solids 255*, 199–207.

[73] *ASTM B367 Grade Ti-PD8A (Commercially Pure Titanium Castings)*; ASM International, 2003; http://products.asminternational.org/datasheets/navigate.do?record=10164&search=titanium%20thermal%20expansion.

[74] Hexoloy SA Silicon Carbide - Technical Data. http://www.hexoloy.com/data-sheets/silicon-carbide-products/pdf/b-1045.pdfêlax.

[75] *ASM International, Aluminum 1100: Commercially Pure Aluminum*; Engineering Alloys Digest, Inc., 1974; http://products.asminternational.org/datasheets/index.jsp.

[76] Hegeman, J., van der Laan, J., van Kranenburg, M., Jong, M., d'Hulst, D., and ten Pierick, P. (2005) Mechanical and thermal properties of SiCf/SiC composites irradiated with neutrons at high temperatures. *Fusion Engineering and Design 75-79*, 789–793.

[77] Palentine, J. (1976) The development of silicon carbide as a routine irradiation temperature monitor, and its calibration in a thermal reactor. *Journal of Nuclear Materials 61*, 243–253.

[78] Parker, W. J., Jenkins, R. J., Butler, C. P., and Abbott, G. L. (1961) Flash Method of Determining Thermal Diffusivity, Heat Capacity, and Thermal Conductivity. *Journal of Applied Physics 32*, 1679–1684.

[79] Cowan, R. D. (1963) Pulse Method of Measuring Thermal Diffusivity at High Temperatures. *Journal of Applied Physics 34*, 926–927.

[80] Youngblood, G. E., Senor, D. J., Jones, R. H., and Graham, S. (2002) The transverse thermal conductivity of 2D-SiCf/SiC composites. *Composites Science and Technology 62*, 1127–1139.

[81] Yamada, R., Igawa, N., and Taguchi, T. (2004) Thermal diffusivity/conductivity of Tyranno SA fiber- and Hi-Nicalon Type S fiber-reinforced 3-D SiC/SiC composites. *Journal of Nuclear Materials 329-333*, 497–501.

[82] Bunnell, L., Bates, J., and Mellinger, G. (1983) Some high-temperature properties of Zircaloy-oxygen alloys. *Journal of Nuclear Materials 116*, 219–232.

[83] Katsura, T. (1993) Thermal diffusivity of silica glass at pressures up to 9 GPa. *Physics and Chemistry of Minerals 20*, 201–208.

[84] Hinoki, T., Katoh, Y., and Kohyama, A. (2002) Effect of Fiber Properties on Neutron Irradiated SiC/SiC Composites. *Materials Transactions 43*, 617–621.

[85] Thermophysical Properties of Matter Database (TPMD); version 7; CINDAS, LLC. 2011; https://cindasdata.com/Applications/TPMD/.

[86] Jones, R. H., Steiner, D., Heinisch, H. L., Newsome, G. A., and Kerch, H. M. (1997) Radiation resistant ceramic matrix composites. *Journal of Nuclear Materials 245*, 87–107.

[87] *SCDAP/RELAP5/MOD3.1 Code Manual Volume IV: MATPRO, NUREG/CR-6150*; Idaho National Laboratory, 1993.

[88] Gilchrist, K. (1976) Thermal property measurements on Zircaloy-2 and associated oxide layers upto 1200°C. *Journal of Nuclear Materials 62*, 257–264.